PHENOMENOLOGICAL STUDIES OF DARK MATTER

by

MIGUEL ALEJANDRO GOMEZ RAMIREZ

Presented to the Faculty of the Graduate School of
The University of Texas at Arlington in Partial Fulfillment
of the Requirements
for the Degree of

DOCTOR OF PHILOSOPHY

THE UNIVERSITY OF TEXAS AT ARLINGTON
May 2014

To the memory of my father, Miguel, and my mother, Soledad.

Acknowledgements

I would like to thank my advisor Dr. Christopher Jackson for his guidance and advice through the course of my Ph.D. graduate studies. I wish to thank Dr. Yue Deng, Dr. Zdzislaw Musielak, Dr. Sangwook Park, and Dr. Jae Yu for their interest in my research and for taking time to serve in my committee.

April 07, 2014

Abstract

PHENOMENOLOGICAL STUDIES OF DARK MATTER

Miguel Alejandro Gomez Ramirez, Ph.D.

The University of Texas at Arlington, 2014

Supervising Professor: Christopher Jackson

It is common knowledge that eighty percent of the matter in our Universe consists of a mysterious substance called "dark matter" (DM) which has only been detected through its gravitational interactions. The "Standard Model" (SM) of particle physics, despite its extremely impressive successes, does not have a good candidate particle to fit the DM requirements. If DM is made up of a particle which interacts weakly and it has a mass on the same scale as other SM particles, it should be detectable.

In this work, two different phenomenological studies of DM are performed. The first possibility is a weakly-interacting particle being detected when a high density of particles and enough energy is present. These conditions are met by objects called "active galactic nuclei" (AGN). AGN are the extremely violent central regions of very large galaxies, and in these regions highly-energetic "jets" of particles are accelerated. It was thought that the possibility the jet particles interact with the surrounding DM producing photons with very distinctive characteristics. A comparison of predicted values with current data is made and it is shown that the prospects for detecting DM in this way are promising in the near future.

In the second approach instead of working with complicated fully developed models, only the minimal content needed to account for DM is added to the SM. The strength of these "simplified" models is that they encompass the interactions and parameter spaces of well-motivated models such as supersymmetry. A simplified model of fermionic DM candidate which couples exclusively to the right handed top quark via a color-charged scalar is considered (motivated by EW symmetry breaking). It is shown that this model can account for the totality of DM and the chances of detection in the near future are very good.

Table of Contents

List of Figures

List of Tables

Chapter 1

Background

1.1 The Standard Model

The theory known as the Standard Model (SM) of particle physics is considered by many to be one of the major achievements of the scientific community during the 20th century. The story starts after the quantum revolution during the first quarter of the century when theorists attempted to formulate a relativistic version of quantum mechanics. However, this proved difficult due to the unexpected and mind boggling features that the solutions exhibited. These problems forced the researchers to move from a single particle interpretation to a many particle interpretation and finally to a field theory interpretation. The first successful quantum field theory (QFT), quantum electrodynamics (QED), is a gauge theory with gauge group $U(1)_{EM}$ and served as a prototype for the explanation of other subatomic phenomena. These included the theory of the strong nuclear force (quantum chromodynamics - QCD for short) based on the $SU(3)$ gauge group and the unified theory of electroweak (EW) interactions based on the, semi-simple, $SU(2)_L \times U(1)_Y$ gauge group. The final ingredient is the Higgs mechanism with a corresponding field (the Higgs field). In Appendix A a summary/review of these ideas is covered.

1.1.1 SM Particle Content

All the fields included into the SM can be classified in different ways (spin, families, hadronic/non-hadronic...) each classification emphasizing one aspect over others. Roughly speaking there are matter particles and force carriers, the matter particles can be accommodated in "families" or generations. Each generation contains two quarks and two leptons with the pattern repeating itself three times. One popular picture of this representation is shown in Figure 1.1a.

A more interesting way to depict the field content of the SM including the chiral components of the fermions is shown in Figure 1.1b. Note that only one generation is included because the fermions in the other generations have the same quantum numbers but differ in their mass. This second diagram shows a more explicit and "faithful" representation of the SM content and points to a larger number of fields (counting chirality) than usual counts. The vertical axis is the electric charge, the two inclined axes are the hypercharge and the weak isospin and due to the amount of

particles that are electrically neutral the center of the plot is crowded. At the origin you will find the photon γ the Z boson and the eight gluons. On the horizontal line (zero electric charge) the Higgs boson and the neutrino-antineutrino pair.

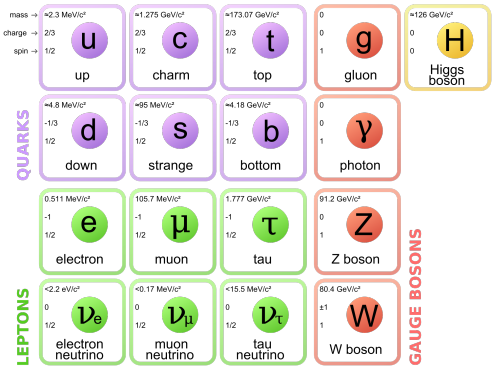

(a) SM content arrange by generation.[1]

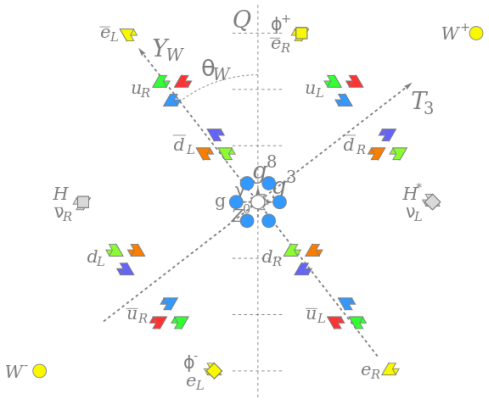

(b) SM content arrange by charge.[2]

Figure 1.1: Particle content of the SM.

The final count of particle/field content of the SM can be found on Table 1.1. Note that at the very least there are 61 different particles.

Table 1.1: Number of particles/fields with and without including the projection over chiral states.

Field	Type/Gen.	Gen.	Anti	Color	Total	Chirality	Total
Quark	2	2	Pair	3	36	2	72
Lepton	2	2	Pair	None	12	2	24
Gluon	1	1	Own	8	8		8
W	1	1	Pair	None	2		2
Z	1	1	Own	None	1		1
Photon	1	1	Own	None	1		1
Higgs	1	1	Own	None	1		1
		Total			61		109

[2]Figure by MissMJ/CC BY 3 (URL: `http://en.wikipedia.org/wiki/File:Standard_Model.svg`). From now on the symbol "CC By 3" should be understood as the link to the creative commons license `http://creativecommons.org/licenses/by-sa/3.0/deed.en`.

[2]Figure by Cjean42/CC BY 3 (URL: `http://en.wikipedia.org/wiki/File:Standard_Model_of_Elementary_Particles.svg`).

1.1.2 SM Lagrangian

The SM is a theory including two (independent) quantum gauge groups: one simple $SU(3)_c$ for strong interactions (QCD) and one semi-simple $SU(2)_L \times U(1)_Y$ for electroweak (EW) interactions. The lagrangian density is[3]

$$\mathcal{L}_{SM} = \mathcal{L}_{gauge} + \mathcal{L}_{QCD+EW} + \mathcal{L}_{higgs} + \mathcal{L}_{Yukawa} \tag{1.1}$$

where the gauge part includes all the gauge fields:

$$\begin{aligned} \mathcal{L}_{gauge} &= -\frac{1}{4}G^a_{\mu\nu}G^{a\mu\nu} - \frac{1}{4}W^a_{\mu\nu}W^{a\mu\nu} - \frac{1}{4}B_{\mu\nu}B^{\mu\nu} \text{ with} \\ G^a_{\mu\nu} &= \partial_\mu G^a_\nu - \partial_\nu G^a_\mu - g_s f_{abc} G^b_\mu G^c_\nu \\ W^a_{\mu\nu} &= \partial_\mu W^a_\nu - \partial_\nu W^a_\mu - g\,\epsilon_{abc} W^b_\mu W^c_\nu \\ B_{\mu\nu} &= \partial_\mu B_\nu - \partial_\nu B_\mu, \end{aligned} \tag{1.2}$$

with G^a_μ representing the gluonic fields, W^a_μ representing the weak (unphysical) fields and B_μ represents the hypercharge field. The interaction term, $\mathcal{L}_{QCD+EW}$, includes the full covariant derivative with coupling constants and (for simplicity) including a number indicating the nature of the particle c_ψ (0 for leptons and 1 for quarks):

$$\mathcal{L}_{QCD+EW} = \sum_{j\in\{L,\,R\}} \sum_{\psi} \bar{\psi}_j \gamma^\mu \left(i\partial_\mu - \frac{g}{2} I_{\psi_j} \vec{\tau}\cdot\vec{W}_\mu - \frac{g'}{2} Y_{\psi_j} B_\mu - \frac{g_s}{2} c_\psi \lambda^a G^a_\mu \right) \psi_j. \tag{1.3}$$

Here it is important to note that the QCD part has universal coupling for all quarks (independent of flavor) while the weak and hypercharge numbers depend on the flavor of the particle. The Higgs part of the lagrangian, $\mathcal{L}_{higgs}$, includes the interaction of the weak fields with the Higgs field and the Higgs potential which is constructed to give mass to three out of the four EW gauge fields:

$$\mathcal{L}_{higgs} = \left| \left(\partial_\mu - \frac{i\,g}{2}\vec{\tau}\cdot\vec{W}_\mu + \frac{i\,g'}{2} B_\mu \right) \phi \right|^2 - \frac{\lambda}{4}\left(\phi^\dagger\phi - v^2\right)^2 \tag{1.4}$$

[3]No ghost fields included although their are necessary for non-abelian gauge theories but are unobservable (hence the name).

with $\phi = \left(1/\sqrt{2}\right)\left(\phi^{+}, \phi^{0}\right)^{T}$ representing a complex field where the index gives the electric charge and both components of the doublet have hypercharge 1. Finally the Yukawa term of the lagrangian, $\mathcal{L}_{Yukawa}$, contains the interactions between the fermionic fields and the Higgs field:

$$\mathcal{L}_{Yukawa} = -\sum_{m,n=0}^{3}\left(\Gamma^{u}_{m\,n}\bar{q}^{0}_{m\,L}\tilde{\phi}\,u^{0}_{n\,R} + \Gamma^{d}_{m\,n}\bar{q}^{0}_{m\,L}\phi\,d^{0}_{n\,R} + \Gamma^{e}_{m\,n}\bar{\ell}^{0}_{m\,n}\phi\,e^{0}_{n\,R}\right) + h.c.. \tag{1.5}$$

Once the Higgs field acquires a non-zero V.E.V., these interactions give rise to the fermion masses. Note that this interaction is different from the others in the sense that the interaction is non-universal in character (hierarchy in Yukawa couplings) and spans several orders of magnitude.

1.1.3 SM Interactions

Knowing the field content and the lagrangian of the SM it is possible to study the interactions described by it and calculate observables. One technique is the perturbative treatment of the theory deriving Feynman rules for all the interactions up to a certain level of precision (perturbation order when applicable). As the name indicates there is a relation between diagrams (pictorial representations) and mathematical expressions[4]. The corresponding Feynman rules for the SM interactions without including the Higgs terms are depicted in Figure 1.2.

The last four vertices are very important because they demonstrate the non-abelian nature of the interactions (self-interaction is something that QED does not have), i.e., the carriers of the force are charged under the group of the interaction. The non-abelian nature of the interactions is responsible for numerous features of the theory, in particular $SU_C\,(3)$ shows asymptotic freedom (the strength of the interaction diminishes with energy) and confinement (no free colored particles are observed).

However not all the features observed are related to the gauge group, some peculiarities of the weak interaction not associated with the nature of the group but experimentally observed are:

1. The interaction is chiral, i.e., it couples differently to right-handed particles and left-handed particles. In particular the $W^{\pm}$ only couples to the left-handed part of the fermionic fields, while the Z couples to both projections but with different strengths.
2. Unlike strong and E&M interactions, weak interactions have a different basis for coupling other than the mass eigenstate basis. This was fixed including the CKM matrix.

[4]Note that this correspondence allowed to do calculations very fast due to its algorithmic nature.

[5]Figure by MissMJ/CC BY 3 (URL: `http://en.wikipedia.org/wiki/File:Standard_Model_Feynman_Diagram_Vertices.png`).

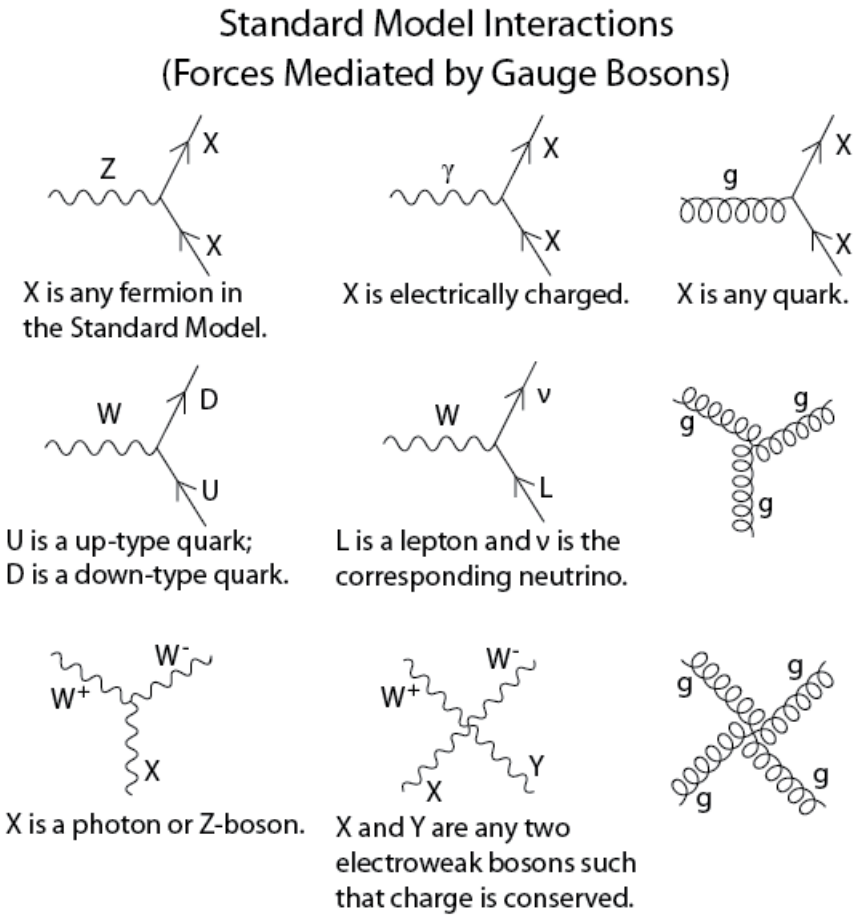

Figure 1.2: Allowed vertices of the standard model for interactions mediated by spin 1 bosons.[5]

3. Again, unlike strong and E&M interactions C, P and CP symmetries are not conserved by weak interactions.
4. The bosons are massive requiring a new mechanism for symmetry breaking. This is the main reason the Higgs mechanism and then the Higgs field was introduced in the SM.

1.1.3.1 Higgs Interactions

The Higgs mechanism and Higgs boson were introduced to give mass to the weak vector bosons forcing a unification between the weak and electromagnetic interactions. As a by product the masses of the fermions were produced by the same mechanism and fixed a different problem (the fermions cannot have mass due to chirality). The set of Feynman diagrams for the theory are shown in Figure 1.3. The coupling between the Higgs boson and the other particles is proportional to the

mass of the other particle, and in the SM the neutrinos are massless therefore there is no coupling for them. However there is evidence that the neutrinos are not massless, but very light compared to the other fermions, and it is possible to include a term for them but due to the unknown nature of the neutrinos (Dirac or Majorana?) that term is considered beyond the SM physics.

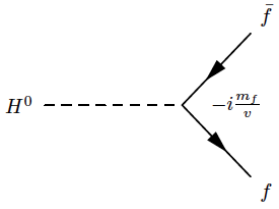

(a) Higgs fermion pair interaction.

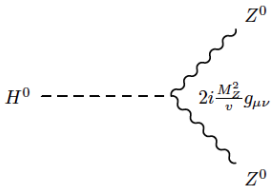

(b) Higgs Z^0 pair interaction.

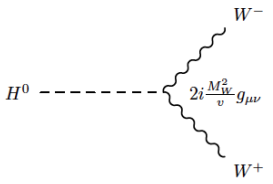

(c) Higgs W pair interaction.

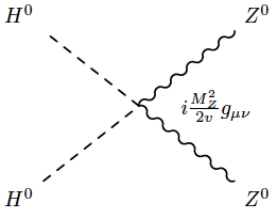

(d) Higgs pair Z^0 pair interaction.

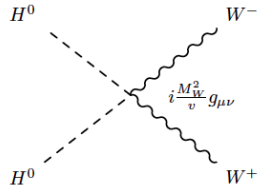

(e) Higgs pair W pair interaction.

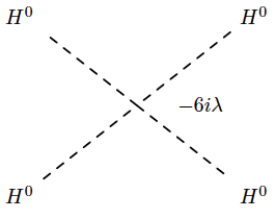

(f) Higgs quartic self-interaction.

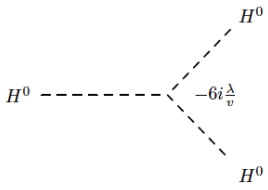

(g) Higgs cubic self-interaction.

Figure 1.3: Allowed Higgs interactions in the SM.

1.1.4 Shortcomings of the Standard Model

The SM has a lot of desirable characteristics such as:

1. All phenomena that can be calculated within the SM fit experimental evidence.
2. Renormalizability. All the interactions in the SM, with the inclusion of the Higgs mechanism, can be renormalized, i.e., there is a procedure to remove infinities with a finite number of parameters order by order.

3. EW unification. The electromagnetic and weak interactions are interrelated among themselves and there exist relations that restrict some of the free parameters contained in the EW sector. However two coupling constants remain after unification reflecting the structure of the group (semi-simple instead of simple).
4. Higgs mechanism. This clever trick allows particles to have mass and the theory still is renormalizable. After almost 50 years of waiting a Higgs boson was detected at CERN laboratory (Aad et al. 2012b; Chatrchyan et al. 2012).

However its great success the SM has some less desirable characteristics (some of theoretical origin and some from experimental origin)

1. It does not include the gravitational interaction at all. By construction the gravitational interaction was never included into the model due to its feebleness compared to the other interactions at the energy scale studied. The main problem is that nobody has found a way to quantize gravity for all possible scenarios.
2. It does not have a viable DM candidate. Although there are some particles in the SM that interact very little they lack all the required characteristics to fit the astrophysical and cosmological observations. In this work I will focus on this point.
3. Strong CP problem. This problem is related to the possibility of a term in the lagrangian of the form:

$$\mathcal{L}_{CPQCD} = -\frac{n_f g_s^2 \theta}{32\pi^2} F^a_{\mu\nu} \tilde{F}^{a\mu\nu} \tag{1.6}$$

   which violates CP symmetry without violating any other dynamical symmetry. However, the lack of empirical evidence of its existence has no theoretical explanation ($\theta = 0$ but at the end it is a free parameter) (Feng 2010).
4. Hierarchy problem. The hierarchy problem is present when the quantum corrections to some calculated parameters are such that their expected value differ vastly from the empirically observed one (it is unnatural). In the SM case the Higgs mass is not protected by any symmetry and the expected mass is $m_H \propto \Lambda^2$ where Λ is a energy scale that determines the cutoff of the perturbative regime. This is problematic because the cutoff is assumed to be very high $\Lambda = M_{GUT} \sim 10^{16}\,\mathrm{GeV}$ or $\Lambda = M_{Pl} \sim 10^{19}\,\mathrm{GeV}$ and $m_h \approx 125\,\mathrm{GeV}$ which implies a cancellation of the leading 30 digits! (Feng 2010)

5. Neutrino oscillations. This observation implies masses for the neutrinos and the SM was built assuming massless and even knowing that it is possible to include a mass term for them it is not clear their nature or how their mass is generated (Feng 2010).
6. Why three generations (without a discernible pattern between the masses of the particles)? There is no reason for the extra-generations of fermions other than they have been observed.
7. Are 19 free parameters too many? This point is mainly an aesthetic one, we do not know how many parameters a theory should have, but it seems that more than a few are too many.

1.2 The Dark Matter Problem

Astronomical observations have forced the scientific community to introduce a new kind of matter that does not interact electromagnetically and for obvious reasons it is called dark matter. The oldest evidence of its existence goes back to 1930s when Fritz Zwicky studied the Coma galaxy cluster and found that the rotation curves implied much more mass than observed. How did he figure it out? Using the virial theorem! Equating the mean kinetic energy to the gravitational energy it is possible to build the expected rotation curve and compare it to the observed rotation curve (a schematic plot showing generic cases for both curves is shown in Figure 1.4a) (Feng 2010; Arrenberg et al. 2013).

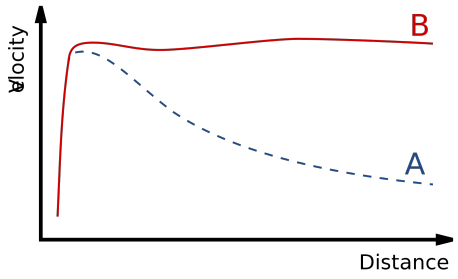

(a) Rotation curves that show the existence of dark matter. Curve A is the calculated based on luminous mass and curve B is the observed one, note that the amount of mass does not decrease with distance as expected from newtonian gravitation and the observed luminosity of the galaxies. Figure by PhilHibbs/CC BY 3 (URL `http://en.wikipedia.org/wiki/File:GalacticRotation2.svg`).

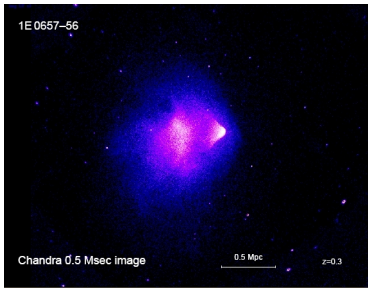

(b) Astrophysical evidence of DM: the Bullet cluster. The bluish part of the image is matter that does not interact and the reddish part is regular matter (false color image). This picture changed the mind of almost everyone about MOND. Source: NASA/Chandra X-ray Observatory (URL: `http://cxc.harvard.edu/symposium_2005/proceedings/files/markevitch_maxim.pdf`).

Figure 1.4: Evidence for the existence of DM in the Universe.

For a while this information was ignored, but in 1970s it was considered again and this time the experimental evidence was considered of the highest quality (Vera Rubin was the astronomer doing this work). And finally evidence start coming from other observational sources: gravitational lensing, cosmic microwave background (CMB), Big-Bang Nucleosynthesis (BBN) and hot Big-Bang (hBB) relics: gravitational lensing in particular excluded to great extent another competing alternative, MOdified Newtonian Dynamics (MOND), for explaining the non-keplerian nature of the rotation curves in galaxies as shown in Figure 1.4b; studying the power spectrum of the Cosmic Microwave Background (CMB), in particular the ratio of the amplitude of the first peak to the amplitude of the second peak, allows to estimate the composition of the universe (less than 5% is SM matter - see Figure 1.5); finally the study of the evolution of the universe and of the relics in hBB allows to exclude some options that would generate scenarios not observed (Feng 2010; Schumann 2013; Arrenberg et al. 2013).

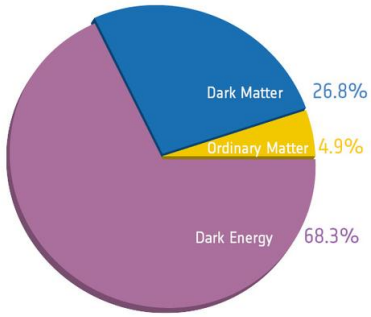

Figure 1.5: Content of the Universe today. Source: ESA/Planck Collaboration.[6]

Some alternatives that were studied (and excluded) through the time included:

- Neutrinos, if massless they still carry energy but were considered not good candidates. On the other hand, if they have a small mass (small compared to other particles in the SM - but still relativistic) they were considered an excellent candidate for DM. From solar observations and atmospheric observations the difference of the squares of pair of masses was obtained and therefore it was implied that at least one of them have mass (Mohapatra et al. 2007). Assume that the squared mass difference is $m_i^2 - m_j^2 = a$ this implies that $\max(m_i, m_j) = \sqrt{a + \min(m_i, m_j)^2}$ (Funchal et al. 2013) taking the maximum observed difference it is possible

[6]URL: `http://www.ucl.ac.uk/star/research/cosmology/science/images/figures/planck_cosmic_pie.`

to infer that one of the neutrinos has mass at least $\sqrt{a}$. The observed values are $\left|m_1^2 - m_2^2\right| = 0.000079\,\mathrm{eV}^2$ and $\left|m_3^2 - m_2^2\right| = 0027\,\mathrm{eV}^2$ which gives one neutrino of at least $0.04\,\mathrm{eV}$. An upper limit for the mass can be determined from tritium decay and accelerator experiments and are $m_{\nu_e}^{eff} < 2\,\mathrm{eV}$, $m_{\nu_\mu}^{eff} < 190\,\mathrm{keV}$ and $m_{\nu_\tau}^{eff} < 18.2\,\mathrm{MeV}$[7]. However, the smallness of the differences implies same order of magnitude mass and generally the minimum value of the upper limit is assumed for al flavors. It turns out that this last assumption allows the neutrinos to be in equilibrium with the thermal bath at the early stages of the BB and then implies a neutrino density given by:

$$\Omega_\nu h^2 \approx \sum_{i=1}^{3} \frac{g_i m_i}{90\,\mathrm{eV}} \tag{1.7}$$

where g_i is the statistical factor associated with the type of particle $g = 1$ for Majorana neutrinos and $g = 2$ for Dirac neutrinos. The density for relativistic particles at the time of structure in the Universe gives an upper bound $\Omega_\nu h^2 < 0.0076$ or $\sum_{i=1}^{3} g_i m_i < 0.7\,\mathrm{eV}$[8], in conclusion neutrinos are a form of DM but cannot be the main component of DM.

- MAssive Compact Halo Objects (MACHOs) are non-luminous objects which inhabited the halos of the galaxies, and are assumed to be brown dwarf stars and black holes[9] (Griest 1993). A brown dwarf is a failed to form star, i.e., a cloud of gas that collapses under gravity but the mass is not large enough to create conditions to initiate a nuclear fusion reaction at its core but can give back a small amount of heat and light back to the Universe. A black hole forms due to the precisely opposite reason, the cloud was so heavy that the collapse is total (a singularity is form at its center), no pressure from nuclear reactions nor degeneracy can support and stop the collapse and not even light (short for any kind of electromagnetic radiation) can escape[10]. The brown dwarves produced disappointing results when after observation and calculation showed that they were at most 6% of the mass of the halos (again not the main component of DM). Finally primordial black holes (those created during the BB) have not been observed to masses as low as a few percent the mass of the Moon (Griest et al. 2013).

At this time it is considered a certainty that dark matter exist and cannot be explained by any of the known physics. So, what could DM be? From a "theoretical" point of view DM candidates should fulfill some criteria:

[7] From J. Beringer *et al.* (Particle Data Group), PR D86, 010001 (2012) (URL: `http://pdg/lbl.gov`).
[8] Including analysis of Planck data $\Omega_\nu h^2 \approx \sum_{i=1}^{3} (m_i/90\ eV) < 0.23/90 \approx 0.003 < 0.1199$ (Ade et al. 2013).
[9] Not really but for simplification I am grouping them together.
[10] Although some radiation might be produce close to the surface in what is known as Hawking radiation.

i Does it match the appropriate relic density[11]?

ii Is it cold?

iii Is it neutral?

iv Is it consistent with Big-Bang Nucleosynthesis (BBN)?

v Does it leave stellar evolution unchanged?

vi Is it compatible with constraints of self-interactions?

vii Is it compatible with direct DM searches?

viii Is it compatible with gamma-ray constraints?

ix Is it compatible with other astrophysical bounds?

x Can be probed experimentally?

Several comments are in order, first a relic density discrepancy may be avoided if DM particles are not a thermal relic, e.g., axions; second the convenience model forces to have a cold DM candidate although some warm-cold mixture is possible but cold being dominant; third point is mandatory otherwise it would be absurd to call it dark matter; the new interactions cannot affect the BBN because this is one of the triumphs of the Big-Bang theory; the next point again constrains the interactions that are possible due to astrophysical observations; the sixth point again constrains the possible interactions but in this case with itself; points seven to nine are related to empirical evidence; and the last point is only a guidance for a good theoretical candidate (it must be possible to look for it, at least in principle).

Some possibilities for the identity of DM that are being studied carefully at present time (a summary of the alternatives reviewed here is given in Table 1.2):

1. Sterile neutrinos. Due to the evidence of at least two massive neutrinos and the nature of the mass term in the lagrangian for all other particles in the SM it is only natural to assume the same term for the neutrino mass (Dirac mass), this implies the existence of right-handed neutrinos but then it is possible to have a Majorana mass term too. These right-handed neutrinos are singlets for all the SM interactions, i.e., they are sterile[12] (Feng 2010; Funchal et al. 2013).

[11] Maybe a misleading name it refers to the current abundance (usually normalized density - Ω_i/Ω_{crit}) of one of the components that were initially present at the early stages of the Universe.

[12] Note however that the mass eigenstates are not exactly the same as the weak/flavor eigenstates, when the diagonalization is carried out some eigenstates are going to be mainly left-handed and some are mainly right-handed these are the ones really identify as active and sterile.

One problem with sterile neutrinos is that their relic density requires very specific behavior of the mass and mixing angle (both of them small) (Gelmini and Gondolo 2010) which is not necessarily what it is expected from a theoretical point of view, e.g., see-saw mechanism, however this is more an aesthetics problem at this point than a real one. Note too, that although they are unstable their mean lifetime is consistent with the age of the Universe. The real problem comes from their mass, these particles are semi-relativistic, i.e., they can be warm DM (WDM) but not cold DM (CDM) and the evidence points to CDM as main component (from structure formation in the universe).

2. Axions. Axions were postulated as a solution to the strong CP problem, a new pseudo-scalar field is introduced and the interaction lagrangian is:

$$\mathcal{L}_a = -\frac{g_s^3}{32\pi^2}\frac{a}{f_a}\epsilon^{\mu\nu\rho\sigma}G^{\alpha}_{\mu\nu}G^{\alpha}_{\rho\sigma} \tag{1.8}$$

where f_a is a new mass scale (Feng 2010). It turns out that the parameter space for this term gets reduced to the light mass and very weakly interacting region. This type of particle is not produced in thermal equilibrium and therefore there are no restrictions on its mass/coupling from the relic density[13], instead another production mechanism is necessary to come into play generating cold (non-relativistic) axions. However the lifetime of the particle is long enough compared to the age of the Universe and this impose an upper limit of $m_a < 3\text{meV}$ from supernova SN1987a, red giants and accelerator searches.

3. Weakly Interacting Massive Particles (WIMPs). One of the most attractive features of WIMPs is that, when in chemical equilibrium in the early Universe, they give the correct relic abundance for CDM. Additionally their interactions make them detectable (a very desirable feature indeed). Even better, some theoretical extensions of the SM to solve other problems contain particles like this in the list of new fields (SUSY and KK). After freeze out (see Appendix D on page 84) and given that there is no more changes of entropy the present relic density is

$$\Omega h^2 \approx \frac{3\times 10^{-27}\text{cm}^3\text{s}^{-1}}{\langle\sigma_{ann}\beta\rangle} \tag{1.9}$$

which for weak cross sections gives the correct order of magnitude of DM density. At first sight this expression is independent of the mass of the WIMP, but this is misleading because

[13] Axions can be produced thermally but they suffer the same problems as neutrinos.

the mass dependence is enclosed by the cross section term (roughly $\Omega h^2 \sim m_\chi^2/g_X^4$). Lo and behold for weak scale masses and couplings this gives a close number to the observed one, this has been dubbed the "WIMP miracle" (Feng 2010; Profumo 2013; Gelmini and Gondolo 2010).

In this work the focus will be on this kind of particle, studying "simplified models", given all their attractive features and its links to the more theoretically motivated extensions of the SM. Specially attractive is the possibility of multiple methods of search and detection that can be put to work in the near future or are operational at present time. These simplified models have a rich phenomenology to study and are generic enough to cover several alternatives without implementing the full complexity of more complete models (SUSY, KK...).

4. Exotic DM[14]. Some people have developed new ideas like superWIMPs, hidden DM, WIMPzillas, WIMPless models, WIMPonium models, dynamical DM (Gelmini and Gondolo 2010; Feng 2010) which attracted some attention but were consider too outrageous by some or were in conflict with some of the observations available at the moment.
5. None of the above. This option covers two possibilities, first DM particles only interact gravitationally in which case it is not going to be possible to characterize it, or second it behaves like something nobody has imagined yet. One case is hopeless and the other requires to measure and detect DM (non-gravitationally) to finally start disentangling this puzzle.

Table 1.2: Summary of viable DM candidates. HP stands for hierarchy problem, NPFN stands for new physics flavor problem. Adapted from (Feng 2010).

	WIMPs	SuperWIMPs	Hidden DM	Sterile ν	Axions
Motivation	HP	HP	HP NPFP	ν mass	Strong CP
Naturally Correct Ω	Yes	Yes	Possible	NA	NA
Production Mechanism	Freeze Out	Decay	Various	Various	Various
Mass Range	GeV − TeV	GeV − TeV	GeV − TeV	keV	μeV − meV

1.2.1 DM Search and Detection

The main processes for DM detection are:

- DM annihilation ($DM + \overline{DM} \rightarrow SM + \overline{SM}$).

[14]This is not a usual category for DM candidates but it serves to group lots of models with not that much in common and some of them just to remind us the unknown nature of the DM puzzle.

- DM elastic scattering ($DM + SM \rightarrow DM + SM$).
- DM creation ($SM + \overline{SM} \rightarrow DM + \overline{DM}$).

Where SM (DM) denote SM (DM) particles. There is an additional process, DM decay which is possible if the particles have a long lifetime compared to the age of the Universe (they have not decayed all by now) (Profumo 2013), however this last process is usually ignored and only the other three are considered. Each process is the basis for a different kind of search, therefore there are three different strategies or approaches for the search of DM particles, one for each process and they are going to be described later. Note that in each case there are three main components of the interaction rate: the number density of DM particles, the number density of SM particles and the cross section flux (cross section times speed) or in equation form:

$$\Gamma = \int \frac{\rho_{i1}}{m_{i1}} \frac{\rho_{i2}}{m_{i2}} dV \times \sigma\beta \times N_{SM,f} N_{DM,f} \tag{1.10}$$

where $\{i1, i2\}$ stand for DM or SM in the initial state and $N_{j,f}$ stands for the flux of particles of type j per event (Profumo 2013).

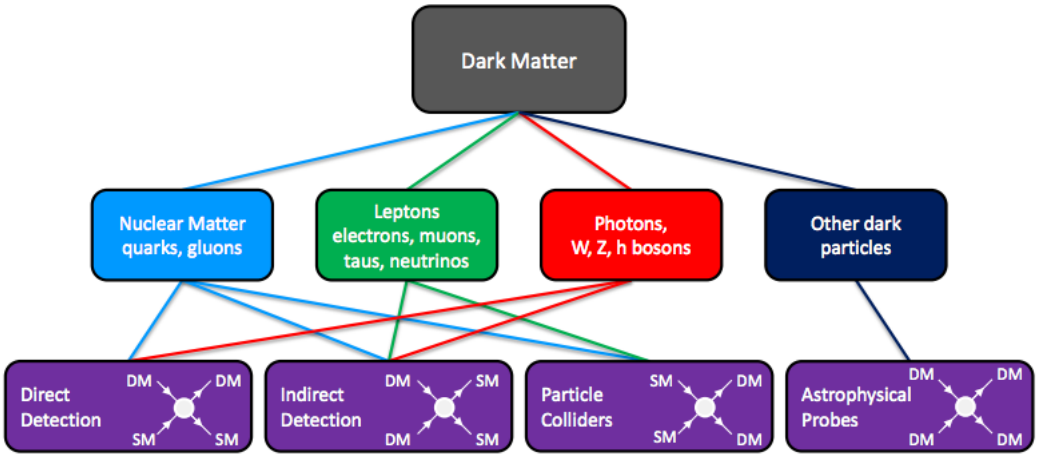

Figure 1.6: Alternatives for DM detection. Source: Snowmass CF1 Summary (Cushman et al. 2013).

As stated earlier each process is associated with a different method of detection and some of its results are going to be found in what follows (see Figure 1.6).

1. Direct detection. In general, DM is expected to be distributed more or less uniformly around the Earth and it should be possible to detect the interaction (nucleus recoil in target material) between DM and SM particles. The targets are composed of huge amounts of material, usually

a liquid detector like Xe (an example of the energy spectra for some typical values of the parameters are shown in Figure 1.7 for different detector materials - note that the selected materials can be highly purified; tend to be inert, three out of four are chemically inert; and the more radiopure the better)[15], surrounded by scintillators or Cherenkov detectors (Cushman et al. 2013). In the case of Weakly Interacting Massive Particles (WIMPs) the expected flux is $10^5\,(100\,\mathrm{GeV}/m_\chi)\ cm^{-2}s^{-1}$ (Taoso et al. 2008). Note that for small mass DM this method is less favorable than collider searches (due to the recoil), but for masses in the TeV range they are better suited for the purpose (because in colliders the energy is not enough to produce this heavy particles).

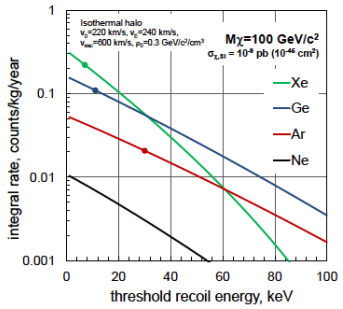

Figure 1.7: Predicted integral spectra for WIMP elastic scattering for Xe, Ge, Ar and Ne assuming perfect energy resolution. Source: Snowmass CF1 Summary (Cushman et al. 2013).

So far only the DAMA/LIBRA and COGENT collaborations have claimed DM detection while studying the annual modulation of event rate (see Figure 1.8b). This modulation is due to the motion of the sun around the galactic center (GC) and the motion around the sun creating small differences in the velocity with respect to the halo depending on the time of the year as shown in Figure 1.8a (Bernabei 2004; Cushman et al. 2013). Unfortunately no other experiment has been able to confirm this observation and it is even in conflict with more recent results from more sensitive experiments like XENON100 and LUX as shown in figure 1.9.

2. Collider production. The idea is to produce a pair of DM particles during the collision of two SM particles, e.g., at LHC two protons colliding head-on may produce a pair particle/anti-particle of DM depending on the underlying particle physics model for the new interaction. The

[15]Note that for low mass WIMP (in the range $1-10\,\mathrm{GeV}$) other materials are being considered, e.g., He^4.

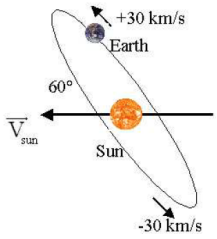

(a) Variation of the relative velocity with respect to the halo due to motion of the Solar system around the GC and to Earth's motion around the Sun.

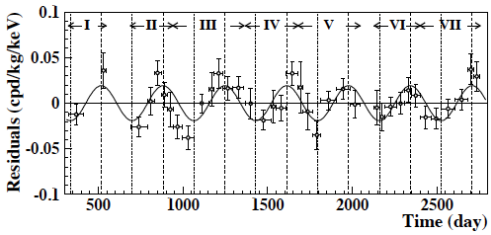

(b) Variation of the relative velocity with respect to the halo due to motion of the Solar system and to Earth's motion around the Sun.

Figure 1.8: DAMA/LIBRA experimental motivation and results. Source: (Bernabei 2004).

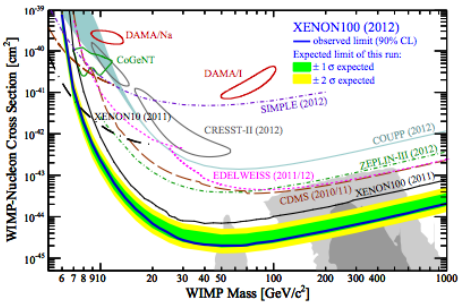

(a) Result for 225 days for XENON100. Incompatible with previous signal reports. Source: (Aprile et al. 2012).

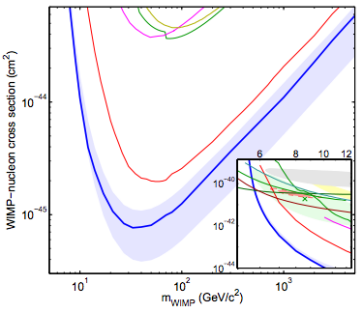

(b) LUX results and comparison with other experiments (inset, blue line represents LUX). Source: (Akerib et al. 2013b).

Figure 1.9: Recent results for direct detection of DM by XENON100 and LUX.

DM particles being stable escape undetected, i.e., as missing energy/momentum[16]. Difficulties in detecting DM at the LHC include the feebleness of the interaction, i.e., the signal might get lost in the background (might get misidentify as neutrinos for example); or the energy required to produce the pair is too high, i.e., the DM is too heavy to be produced with current accelerators[17].

It is important to note that independent of the details, in terms of complementarity colliders provide a control environment for the study of the nature of DM particles, and generally most of the WIMPs masses considered are accessible at those facilities but have

[16]Remember that "backgrounds are typically smaller for larger values of missing momentum, collider searches tend to be most effective for low-mass dark matter particles, which are more easily produced with high momentum" (Arrenberg et al. 2013), i.e., collider searches have an advantage over other alternatives when DM particles are not that heavy.

[17]Or maybe DM is hadrophobic and it is leptophilic which implies that a lepton collider is better suited to detect it.

problems distinguishing missing signals from particles produced with a relatively small lifetime (of the order of ns) from particles with much longer lifetime (of the order of Gy).

To date there has not been any strong signal of DM presence at LHC, but note that most of the analysis are based on some realization of a theoretical model (SUSY, KK...) and the results are given in terms of this models and their parameters (see Figure 1.10).

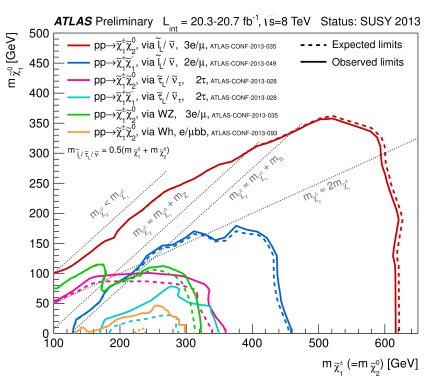

(a) Exclusion of parameter space for SUSY. Source: ATLAS public results.

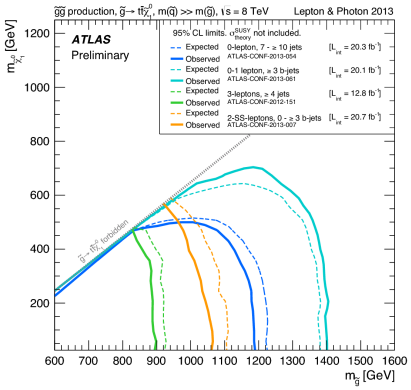

(b) Values for some parameters in SUSY model. Source: ATLAS public results.

Figure 1.10: Results from ATLAS collaboration as of August 2013.[18]

3. Indirect detection. Finally,[19] the annihilation of DM into SM particles result in spectral features that can be very different from the spectra generated by astrophysical sources. These observations are astronomical, i.e., require telescopes and detectors for all spectrum of electromagnetic radiation, detectors for high energy charged particles and high energy neutral particles (neutrinos) coming from outer space (Profumo 2013). In general, electromagnetic radiation is considered the best because it travels in - more or less - straight trajectories pointing to the point of origin facilitating the analysis of the background and alternative explanations. And among the charged particles and the neutral particles there is no clear winner. On one hand, charged particles are easier to detect and if they are antiparticles the general consensus is that they are a signal from DM annihilation (if a large flux is detected). On the other hand, neutral particles can travel longer distances without appreciable deviation from the initial direction and can point to the original source but are much more difficult to detect and the expected flux is lower. There are several instruments Earth bound and orbiting the Earth taking data at the writing of this work (AMS, electrons, positrons, anti-nuclei, ISS; Fermi,

[19]URL: `https://twiki.cern.ch/twiki/bin/view/AtlasPublic/SupersymmetryPublicResults`

photons, electrons, satellite; HESS, photons, electrons, Namibia; IceCube, neutrinos, Antarctica; MAGIC, photons, electrons, positrons, La Palma, Spain; PAMELA, electrons, positrons, satellite; and VERITAS, photons, electrons, positrons, Arizona, USA) (Buckley et al. 2013). It is usually assumed that it is possible to constrain the mass of the particle with stronger bounds in indirect detection than in direct detection experiments.

The methods for looking for DM can be grouped as follows

(a) Charged Cosmic Ray/Antimatter Experiments. There are several indications of excess of positrons over electrons by different collaborations.

- Hints by HEAT and AMS-1 of increase in the positron ratio.
- PAMELA found an increase in the ratio of positrons to total number of particles $N_+/(N_+ + N_-)$ from 10 GeV to 100 GeV.
- Confirmation and extension of range up to 200 GeV by Fermi collaboration.
- Confirmation with smaller errors by AMS-2 collaboration (see figure 1.11a).
- No similar increase in other channels, e.g., antiprotons signal.

At present time there is no known astrophysical process that can explain these observations making the DM option more plausible (than before). In order to explain these observations some properties of DM particles can be deduced including: a mass of a few TeV, leptophilic (to explain the absence of signal in the antiproton channel) with cross section flux of about $10^{-23}\text{cm}^3/s$ (see Figure 1.11b).

(b) Gamma-ray Experiments. There is more than one way to produce photons from DM annihilation.

- Prompt gamma-rays from bremsstrahlung of charged particles and fragmentation of hadrons on the final stages of the cascade producing a peak in the continuum close the DM mass; from bremsstrahlung from internal particles on the annihilation process (subdominant); and annihilation into a pair of photons or photon and a vector bosons (through loops) producing a line spectrum or a forest of line spectrum. In all cases the point of origin of the photons follows closely the DM distribution.
- Inverse Compton scattering (ICS) gamma-rays from electrons and positrons created in the DM annihilation onto CMB photons. A wider distribution than prompt gamma-rays and difficult to pinpoint the source.

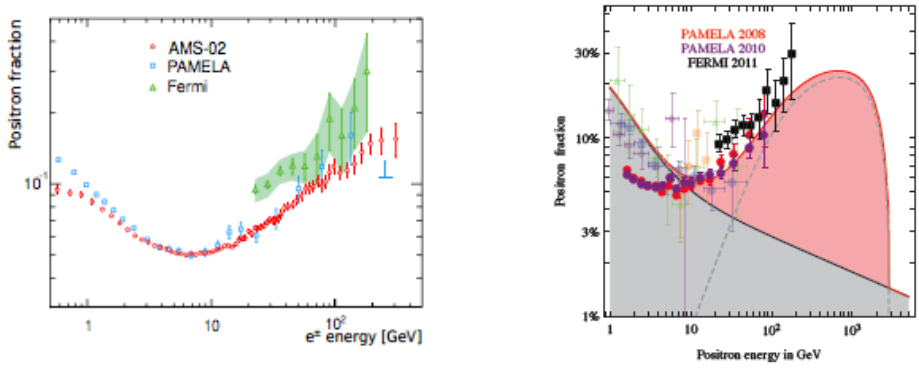

(a) Positron fraction as measure by different experiments. AMS@ confirms the previous observations due to PAMELA and Fermi shows same trend. Source: (Corti 2014).

(b) Plausible explanation with DM for signals of antimatter from outer space, the pink shaded area corresponds to a DM particle of 3 TeV (note the sharp cutoff at DM particle's mass). Source: (Cirelli 2012).

Figure 1.11: Hints of signals of DM from outer space.

- Synchrotron emission while on magnetic fields present along the trajectory of the charged particles created in the annihilation process. The best places to look at are those in which the magnetic field is large.

In general the idea is to identify places in the Universe in which one of the conditions is fulfilled and it is easy to detect the signal. Obviously the best targets have a high density of DM (higher than average) and/or the astrophysical background is low. In general there is a consensus about no signal detected so far (although some claims have been made but not confirmed or simply proven wrong, see Figure 1.12). Note, also, that the empirical evidence from gamma-rays contradicts the evidence from antimatter.

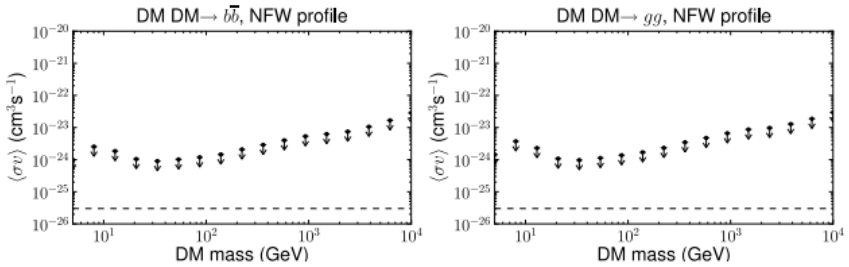

Figure 1.12: Cross section bounds for a specific DM density and specific particle physics model from Fermi LAT. Source: Ackerman et al. (Ackermann et al. 2013).

(c) Neutrino Experiments. Neutrinos travel through almost any material with little deflection making them better to locate their source, however due to the same reason they are very difficult to detect. Most neutrino detectors are underground and use the Earth to screen other signal coming from cosmic rays (the signal should come from below to be used). Again the targets include the GC and the galactic halo; satellite galaxies and clusters of galaxies; but there is another possibility much closer to us, the Sun. The signal from the Sun is a very energetic neutrino that no astrophysical nor stellar process is known to produce. Some limits for cross section can be seen in Figure 1.13.

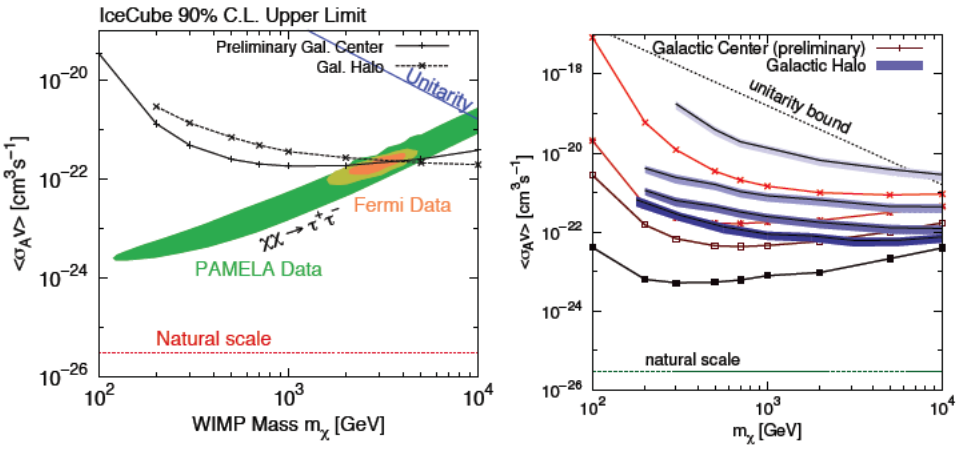

Figure 1.13: Cross section bounds for DM annihilation from the GC (left) and the galactic halo (right) found by IceCube. Source: Cirelli (Cirelli 2012)

Note, however, that although DM annihilation is the most common process studied in indirect detection efforts, it is by no means unique. There is another process that can occur in outer space, in particular the scattering of DM and SM particles close to the GCs where the concentration of both types of particles is extremely large and the energy of the SM particles is large too. This Active Galactic Nuclei (AGN), can give a very distinctive signal and it is worth to study it.

It is important to note too that the discovery of DM particles and its characterization is going to come from a mixture of all kinds of detection (complementarity) because at this time it is believe that a signal in one of the modes but not the others is not conclusive enough. This reason supports our effort to model and study all modes at the same time to get a more complete and accepted picture.

Chapter 2

Gamma-ray Signals from AGN

Not knowing for sure that DM has been detected forces us to explore all the possibilities, i.e., looking in different parts of the Universe and/or considering more exotic scenarios. In this chapter, the former option will be considered: searching for signals of dark matter in regions of the Universe that have yet to be explored. In the next chapter, a new model of dark matter will be explored and its possible signals at the type of experiments discussed in the last part of the chapter.

In this chapter, the possibility of the detection of high-energy gamma-rays originating in the interaction of DM and SM particles around some AGN is explored. This scenario is favorable because the DM density close the the core of the AGN could be very high compared to the average DM density making more likely the interaction of DM particles. Additionally when high-energy particles are flowing out of the jets the whole picture improves more. The basic idea is that collisions of jet particles with DM particles creates a heavy, charged particle (not included in the content of the SM) that quickly decays back to the original particles, although, an additional photon can be emitted from the initial, final or intermediate state charged particles. One of the consequences is the appearance of a sharp cutoff (of the order of the difference in mass between the KK particles) that is not common in astrophysical processes, but by no means impossible.

The question to be answered in this chapter is whether or not the spectra from these gamma-rays is discernible from astrophysical gamma-rays. In what follows, a computation of the complete WIMP-induced gamma ray flux for an AGN (including the AGN jet-WIMP scattering along with the contributions from annihilations) is done. In previous studies the focus was the gamma ray spectrum coming from the scattering between AGN jets and WIMPs, in this work one step more is taken and the complete spectrum is constructed. This chapter is based on the paper "WIMP-induced Gamma-ray Spectrum of Active Galactic Nuclei" (Gómez et al. 2013).

2.1 The Model

To investigate the possibility of detecting DM around AGN, a particular model must be chosen, and the chiral square, which belongs to the Universal Extra-Dimensions (UED) family[1], was selected. The "chiral square" derives its name from the geometrical form obtained in the manifold generated by the two new dimensions, i.e., they form a square. The other condition imposed is the identification of adjacent sides (folding the square along the main diagonal) creating the quantization rule that allows to calculate the mass of the Kaluza-Klein (KK) modes $m_{j,k}^2 = m_0^2 + \pi^2(j^2+k^2)/L^2$ with m_0 the mass of the corresponding SM particle (Dobrescu and Ponton 2004; Burdman et al. 2006a,b; Dobrescu et al. 2007b).

The model contains an additional discrete symmetry implying the existence of an excited mode that cannot decay (at tree level) and serves as DM particle. The DM candidate is assumed to be a color singlet and, for obvious reasons, electrically neutral, i.e., the colored and charged particles are heavier than the DM candidate. All this gives us that the DM particle is the scalar partner of the hypercharge boson $B_H^{(1,0)}$ (ignoring any possible mixing with the weak Ws partners) and the interaction is $U(1)$ with coupling g_1 and the relevant charge is hypercharge. The model contains a long list of interactions, but the one that is relevant for this work is between a SM electrically charged particle, the KK excited associated particle and the WIMP:

$$\Delta\mathcal{L} = g_1 \left[\bar{\psi}_E \left(Y_L P_L + Y_R P_R\right) \psi_e + \bar{\psi}_e \left(Y_L P_R + Y_R P_L\right) \psi_E\right] B_H \tag{2.1}$$

where Y_i is the hypercharge of the i chiral part of the SM field, ψ_e is the SM particle and ψ_E is the KK excited state. From this lagrangian and the relic abundance constraint it is possible to find some limits on the mass of the excited hypercharge boson: $190\,\mathrm{GeV} \leq M_B \leq 215\,\mathrm{GeV}$[2].

2.2 Gamma-rays from the Scattering between DM Particles and Particles on AGN Jets

The components for the calculation of the gamma-ray flux are the number of particles in the jet and its energy, the number of particles of DM available for scattering and the cross section

[1] Extra dimensions means that additional space-like dimensions are added to the regular four dimensional space-time, universal means that the fields have access to all the dimensions as opposed to ADD models where SM particles have access to the initial four-dimensional space. The extra dimensions are assumed to be compactified with radii much larger then l_{Pl} but smaller than currently explored distances. Roughly the inverse of the radius gives the mass scale for the KK excitations $M_{KK} \sim 1/R$. Note that the starting point for each "tower" of KK excitations corresponds to a SM particle.

[2] Note that those limits are valid only if the WIMP is a thermal relic and the DM particle is unique and there is no more complex dark matter sector with several quasi-stable particles contributing to the thermal relic density.

for the process (which measures the probability of interaction). The differential cross section is a function of the energy of incoming particles and the energy of the photon[3] (but we are assuming that the DM particle is heavier than the scattered SM particle, an electron in this case, therefore its kinetic energy is negligible and its total energy is given by its mass). Additionally from astrophysical models it is known that the flux of electrons in the jet depends on their energy too which implies that the differential photon flux is going to be related to an integral of those quantities with respect to the energy of the electron

$$\frac{d\Phi_\gamma}{dE_\gamma} = \int \delta_{DM} \times \left(\frac{1}{d_{AGN}^2} \frac{d\Phi_e^{AGN}}{dE_e} \right) \times \left(\frac{1}{M_B} \frac{d^2\sigma_{e+B_H \to \gamma+e+B_H}}{d\Omega dE_\gamma} \bigg|_{\theta=\theta_0} \right) dE_e \tag{2.2}$$

where the first factor of the integrand is related to the density of the DM that is in the vicinity of the core of the galaxy where the interaction is more probable, the second factor is related to the number of electrons being expelled in the jets and the last factor gives the probability of interaction (or how often the particles interact). A closer look at each of these factors follows, because it is possible to learn the limitations of this approach checking all the assumptions and approximations that were made.

2.2.1 DM Density Profile

The first factor of the integrand in Equation 2.2 is related to, but not exactly equal to, the density of DM around the AGN, which prompts the question why is not the density of DM around the AGN? And the answer is because what really matters is how the particles in the jet see the DM density and because the jets are highly collimated there is a preferred direction, that of the direction of the jet. Note that we are assuming a spherically symmetric distribution of DM around the AGN therefore the number of DM particles that the particles in the jet find are given by the integral of the density along the path of the particles in the jet (radial direction):

$$\delta_{DM} = \int_{r_{min}}^{r_0} \rho_{DM}(r)\, dr \tag{2.3}$$

in principle the integral could go from a very small radius (r_{min} or the base of the jet) at which the jet originates to infinity, however the jet becomes incohesive at some point and the DM density is

[3] Not enough delta functions to integrate out this degree of freedom easily and at the end it is what is observed.

small and the integral can be approximated with this cut[4]. Note that this integration is equivalent to find an average surface density that the particles in the jet find on their path and therefore is related to the number of DM particles with which the SM particles can collide (Gorchtein et al. 2010).

As mentioned previously the assumption is that the DM density is higher closer to the core. However, due to the feebleness of the interaction, if a detectable signal is desired a slightly more peaked profile than usual (standard profiles for DM in galaxies are Einasto, Navarro-Frenk-White - NWF -, and adiabatic) is necessary. On the other hand, the activity of the nucleus of the galaxy modifies the DM somehow. For these reasons the chosen profile to work with is due to Gondolo and Silk (GS) (Gondolo and Silk 1999), who worked out the new profile close to an active core (and this is the standard for AGN)[5] (which we assume to be long lived enough to detect signals from them now) in which the central part is more spiky than density profiles used for regular galaxies (Einasto, NFW, and adiabatic). Two parts define the GS profile: the core contribution (related to the interaction between the DM and the black hole) and a spike contribution:

$$\rho\left(r\right) = \frac{\rho'\left(r\right)\ \rho_{core}}{\rho'\left(r\right) + \rho_{core}} \tag{2.4}$$

where $\rho_{core} \approx {}^{M_{DM}}/_{\langle\sigma\beta\rangle_0 t_{BH}}$ with t_{BH} the time since the formation of the BH, and $\langle\sigma\beta\rangle$ the thermally averaged cross section flux for the DM annihilation process; i.e., the longer the time of interaction the larger the volume or the smaller the density. The spike contribution is a slightly more complicated:

$$\rho'\left(r\right) = \rho_0 \left(\frac{R_{sp}}{r_0}\right)^{-\gamma} \left(1 - \frac{4R_S}{r}\right)^3 \left(\frac{R_{sp}}{r}\right)^{\gamma_{sp}} \tag{2.5}$$

with γ_{sp} the slope of the central spike, R_{sp} the radius defining the spike and R_S the Schwarzschild radius of the black hole. But these are observables, the relation between the observed quantities and the GS parameters is:

$$\gamma_{sp} = \frac{9 - 2\gamma}{4 - \gamma} \qquad , \qquad R_{sp} = \alpha_\gamma\, r_0 \left(\frac{M_{BH}}{\rho_0\, r_0^3}\right)^{1/(3-\gamma)} \qquad \text{and} \qquad \alpha_\gamma \propto \gamma^{4/9}. \tag{2.6}$$

[4]Note that previous studies have shown that the value for the upper limit is way less important than the selection of the lower limit, this reflects the suppress nature of the DM density profile around the AGN.

[5]For the case of Centaurus A the distance is so large that it is very difficult if not impossible to achieve resolutions of distances less than 100-1000 Mpc (Gorchtein et al. 2010; Huang et al. 2012) making "direct" inferences for the density profile useless and theoretical approximations and extrapolations are necessary making this model more attractive.

Note that for a non-rotating black hole the radius of the last stable orbit is $r_{last} = 4R_S$ (this is the radius of minimum distance to the black hole for any particle that interacts gravitationally) or $\rho_{DM}(r < r_{last}) = 0$ which sets a natural lower limit for the integral in Equation 2.3, $r_{min} = 4R_S$. The constant ρ_0 is fixed through the saturation of the inequality

$$\int_{4\,R_S}^{10^5\,R_S} 4\pi r^2 \rho_{DM}(r)\,dr \leq \Delta M_{BH} \tag{2.7}$$

which states that the uncertainty on the mass of the black hole has to be larger than the mass of DM around the black hole.

For definiteness we will use Centaurus A AGN as example of this type of calculation (and because some observational data is available for it). The parameters for Centaurus A AGN are shown on Table 2.1 (Abdo et al. 2010). The results for different combinations of the time of

Table 2.1: Values for GS parameters for Centaurus A AGN.

M_{BH} [$M_\odot$] Black Hole mass	$(5.5 \pm 3.0) \times 10^7$
R_S [pc] Schwarzschild radius	5×10^{-6}
t_{BH} [yr] Age of Black Hole	$10^8 - 10^{10}$
α_γ	0.1
r_0 [pc] (upper limit of integration)	15×10^3
d_{AGN} [pc]	3.7×10^6
θ_0	68°

existence of the black hole and the DM annihilation cross section are shown in Figure 2.1 on the next page. The annihilation cross section is in the range of the "magic" number for the "WIMP miracle" to work. As stated before the upper limit of integration does not matter as much as the lower limit of integration (look at Figure 2.1b the curves start almost horizontal but at some point start varying really fast), note too the rapid decay of the DM density for relatively small radius (Figure 2.1a on the following page). Also note that the shorter the time and the smaller the cross section the greater the number of particles in the spike, therefore the annihilation cross section is affecting the computations in two ways: if it is small then there are more particles available to interact, but they interact with less probability. On the other hand, if the cross section is large, the density is lower making less particles available for interaction but they interact more strongly (the problem is that the relation is non-linear and is non-trivial to find the best scenario possible) but contrary to other

indirect search methods in this case the lower the cross section the better the chances of a signal according to Profumo et al. (Gorchtein et al. 2010).

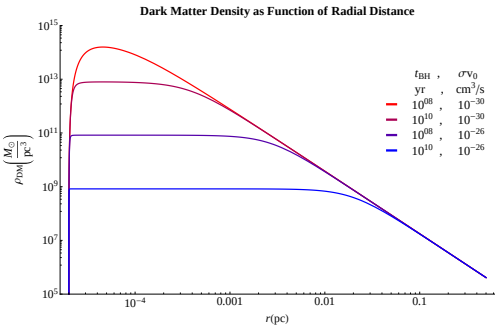

(a) DM density profile for Centaurus A for different values of ρ_{core} where $\gamma = 1$, $M_{BH} = (5.5 \pm 3.0) \times 10^7\, M_\odot$, $R_S = 5 \times 10^6$ pc, $r_0 = 15 \times 10^3$ pc.

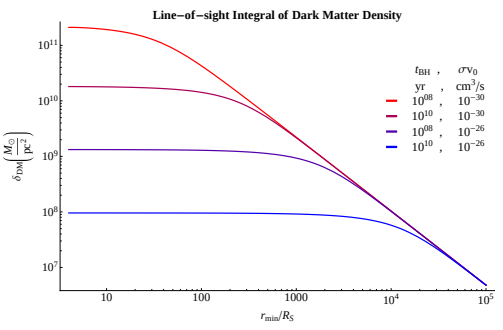

(b) los integral of DM density profile for Centaurus A for different values of ρ_{core} with $\gamma = 1$, $M_{BH} = (5.5 \pm 3.0) \times 10^7\, M_\odot$, $R_S = 5 \times 10^6$ pc, $r_0 = 15 \times 10^3$ pc.

Figure 2.1: DM density profile and los integral.

2.2.2 The AGN Jet

A priori it is possible to name several factors affecting the dynamics of the jet such as geometry, energy distribution, composition of the jet, but it turns out that the most important effect is due to the energy distribution (once the composition has been identified) and the exact geometry can be neglected (Gorchtein et al. 2010; Huang et al. 2012). The standard approach is to utilize the so-called blob geometry in which particles move isotropically and assume that the gamma factor with respect to the black hole is not too large ($\Gamma_B \sim 3$)[6]. A broken power law for the energy distribution is obtained from Fermi LAT observations (Abdo et al. 2010):

$$\frac{d\Phi_e^{AGN}}{d\gamma'}(\gamma') = \frac{1}{2} k_e \gamma\prime - s_1 \left[1 + \left(\frac{\gamma'}{\gamma'_{br}}\right)^{(s_2 - s_1)}\right]^{-1} \qquad \gamma'_{min} \leq \gamma' \leq \gamma'_{max} \tag{2.8}$$

with $s_1 = 1.8$, $s_2 = 3.5$, $\gamma'_{br} = 4 \times 10^5$, $\gamma'_{min} = 8 \times 10^2$, $\gamma'_{max} = 10^8$, and $\gamma' = {}^{E'}/_{m_e}$. The constant k_e is found saturating the Eddington limit for the black hole mass L_e:

$$L_e = m_e \int_{-1}^{1} \int_{\gamma_{min}}^{\gamma_{max}} \frac{\gamma}{\Gamma_B (1 - \beta_B \mu)} \frac{d\Phi_e^{AGN}(\gamma \Gamma_B (1 - \beta_B \mu))}{d\gamma} d\gamma d\mu \tag{2.9}$$

[6] In this reference frame the angle of the jet is smaller than the multiplicative inverse of the gamma factor ($\theta < {}^1/_{\Gamma_B}$).

where the primed quantities are in the "bulk" reference frame and unprimed quantities refer to the black hole. The polar angle dependence is included in the $\mu(=\cos\theta)$ variable.

The final form for the factor for the jet particles is

$$\frac{1}{d_{AGN}^2}\frac{d\Phi_e^{AGN}}{dE_e} = \frac{1}{d_{AGN}^2 m_e}\int_{\mu_0}^{1}\frac{1}{\Gamma_B\left(1-\beta_B\mu\right)}\frac{d\Phi_e^{AGN}\left(\gamma\Gamma_B\left(1-\beta_B\mu\right)\right)}{d\gamma}d\mu \tag{2.10}$$

and μ_0 indicates how narrow (collimated) the jet is. A typical value for a highly collimated jet is $\mu_0 = 0.9$ and we will use that as our lower limit of integration (this cone includes close to 80% of the particles according to Profumo et al. (Gorchtein et al. 2010)).

2.2.3 The Cross Section

The differential cross section for the scattering $B_H + e^- \to B_H + e^- + \gamma$ has six different Feynman diagrams (three for s channel and three for u channel processes) as shown in Figure 2.2 where the virtual particle exchanged is the first KK excited state of the electron $E^{(1,0)}$ (E for simplicity).

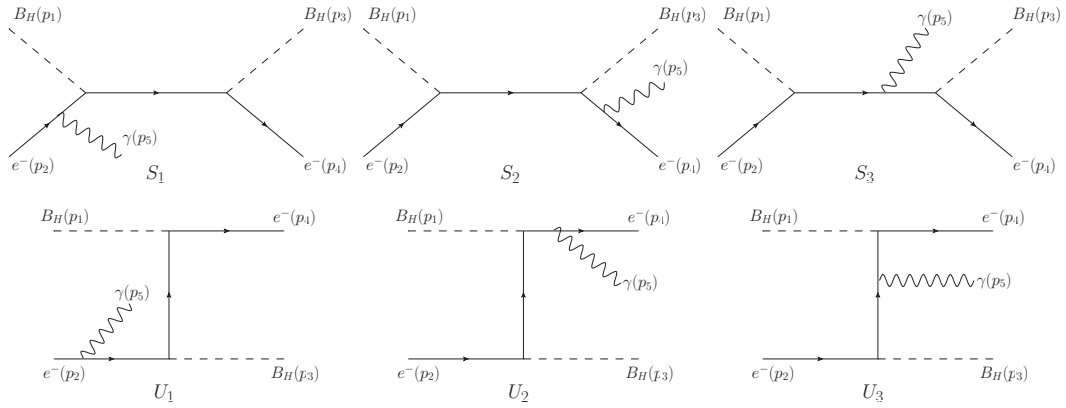

Figure 2.2: Feynman diagrams for the scattering of DM and SM particles ($B_H + e^- \to B_H + e^- + \gamma$) through the exchange of an excited state of the electron (E). There are no diagrams for a t channel because there is no more ways to "rotate" the diagram with the existing vertices in the theory, only s and u channel contributions.

It is obvious that the matrix element can be written as $\mathcal{M} = \sum_i \mathcal{M}_i^\mu \epsilon_{\mu,5}$ where $\epsilon_{\mu,5} = \epsilon_\mu(p_5)$ is the polarization four-vector for the photon with four-momentum $p_5 = p_5^\nu$[7]. The amplitudes for the s-channel diagrams are given by:

$$\begin{aligned}
\mathcal{M}_{S_1}^\mu &= \frac{eg_1^2}{\Sigma_{34} t_{25}} \bar{u}_4 \left(Y_L P_R + Y_R P_L\right) \left(\not{p}_3 + \not{p}_4 + M_E\right) \left(Y_L P_L + Y_R P_R\right) \left(\not{p}_2 - \not{p}_5\right) \gamma^\mu u_2 \\
\mathcal{M}_{S_2}^\mu &= \frac{eg_1^2}{\Sigma_{12} s_{45}} \bar{u}_4 \gamma^\mu \left(\not{p}_4 + \not{p}_5\right) \left(Y_L P_R + Y_R P_L\right) \left(\not{p}_1 + \not{p}_2 + M_E\right) \left(Y_L P_L + Y_R P_R\right) u_2 \\
\mathcal{M}_{S_3}^\mu &= \frac{eg_1^2}{\Sigma_{12} \Sigma_{34}} \bar{u}_4 \left(Y_L P_R + Y_R P_L\right) \left(\not{p}_3 + \not{p}_4 + M_E\right) \gamma^\mu \left(\not{p}_1 + \not{p}_2 + M_E\right) \left(Y_L P_L + Y_R P_R\right) u_2
\end{aligned} \tag{2.11}$$

where the denominators have been adjusted to behave correctly in case of resonance $\Sigma_{ij} = s_{ij} - M_E^2 - i\sqrt{s_{ij}}\,\Gamma_E$ with Lorentz invariants defined as $s_{ij} = (p_i + p_j)^2$ and $t_{ij} = (p_i - p_j)^2$. The decay width for E is independent of the energy and to leading order is given by:

$$\Gamma_E = \frac{g_1^2}{32\pi} \left(Y_L^2 + Y_R^2\right) \frac{\left(M_E^2 - M_B^2\right)^2}{M_E^3}. \tag{2.12}$$

The u-channel amplitudes are not resonant in the region of interest and are given by:

$$\begin{aligned}
\mathcal{M}_{U_1}^\mu &= \frac{eg_1^2}{t_{14} t_{25}} \bar{u}_4 \left(Y_L P_R + Y_R P_L\right) \left(\not{p}_4 - \not{p}_1 + M_E\right) \left(Y_L P_L + Y_R P_R\right) \left(\not{p}_2 - \not{p}_5\right) \gamma^\mu u_2 \\
\mathcal{M}_{U_2}^\mu &= \frac{eg_1^2}{t_{23} t_{45}} \bar{u}_4 \gamma^\mu \left(\not{p}_4 + \not{p}_5\right) \left(Y_L P_R + Y_R P_L\right) \left(\not{p}_2 - \not{p}_3 + M_E\right) \left(Y_L P_L + Y_R P_R\right) u_2 \\
\mathcal{M}_{U_3}^\mu &= \frac{eg_1^2}{t_{14} t_{23}} \bar{u}_4 \left(Y_L P_R + Y_R P_L\right) \left(\not{p}_4 - \not{p}_1 + M_E\right) \gamma^\mu \left(\not{p}_2 - \not{p}_3 + M_E\right) \left(Y_L P_L + Y_R P_R\right) u_2.
\end{aligned} \tag{2.13}$$

The unpolarized differential cross section for $B_H(p_1) + e(p_2) \to B_H(p_3) + e(p_4) + \gamma(p_5)$ is given by:

$$d\sigma = (2\pi)^4 \delta^4(p_1 + p_2 - p_3 - p_4 - p_5) \frac{1}{4E_1 E_2} \frac{d^3 p_3}{(2\pi)^3 2E_3} \frac{d^3 p_4}{(2\pi)^3 2E_4} \frac{d^3 p_5}{(2\pi)^3 2E_5} \sum \left\langle |\mathcal{M}|^2 \right\rangle \tag{2.14}$$

and using the four dimensional Dirac delta function to integrate four degrees of freedom ($\vec{p}_3$ with $\delta^3(\vec{p}_1 + \vec{p}_2 - \vec{p}_3 - \vec{p}_4 - \vec{p}_5)$, and E_4 with $\delta(E_1 + E_2 - E_3(p_1, p_2, p_4, p_5) - E_4 - E_5)$), the differential cross section is:

$$\frac{d^2\sigma}{dE_5 d\Omega_5} = \frac{1}{(2\pi)^5} \frac{E_5}{32 E_1 E_2} \int \frac{E_4}{E_3} \frac{1}{|1 + J|} \sum \left\langle |\mathcal{M}|^2 \right\rangle d\Omega_4 \tag{2.15}$$

[7]From now on all variables that depend on the four-momentum p_i are going to be labeled by the subscript i of the four-momentum.

where quantities with indices 3 and 4 are functions of the remaining variables and J is to the change of integration variable between $|\vec{p}_3|$ and E_3. To simplify the calculations we choose the reference frame in which the DM particle is at rest, the initial linear momentum of the SM particle coincides with the positive z axis and the the azimuthal angle for the photon is zero ($\phi_5 = 0$). The four-momenta in this reference frame are:

$$p_1^\mu = \begin{pmatrix} M_B \\ \vec{0} \end{pmatrix} \quad p_2^\mu = E_2 \begin{pmatrix} 1 \\ 0 \\ 0 \\ 1 \end{pmatrix} \quad p_3^\mu = \begin{pmatrix} E_3 \\ \vec{p}_3 \end{pmatrix} \quad p_4^\mu = E_4 \begin{pmatrix} 1 \\ \sin\theta_4 \cos\phi_4 \\ \sin\theta_4 \sin\phi_4 \\ \cos\theta_4 \end{pmatrix} \quad p_5^\mu = E_5 \begin{pmatrix} 1 \\ \sin\theta_5 \\ 0 \\ \cos\theta_5 \end{pmatrix} \tag{2.16}$$

where the mass of the electron has been ignored and due to the integrations (four-momentum conservation) the following relations are true:

$$\begin{gathered} \vec{p}_3 = \vec{p}_1 + \vec{p}_2 - \vec{p}_4 - \vec{p}_5 \\ E_3 = \sqrt{M_B^2 + E_2^2 + E_4^2 + E_5^2 - 2E_2E_4c_4 - 2E_2E_5c_4 + 2E_4E_5\left(s_5s_4\cos\phi_4 + c_5c_4\right)} \\ E_4 = \frac{M_B\left(E_2 - E_5\right) - E_2E_5\left(1 - c_5\right)}{M_B + E_2\left(1 - c_4\right) - E_5\left(1 - s_5s_4\cos\phi_4 - c_5c_4\right)} \\ J = \frac{1}{E_3}\left[E_4 - E_2c_4 + E_5\left(s_5s_4c_4 + c_5c_4\right)\right] \qquad \text{with} \\ c_i = \cos\theta_i \quad \text{and} \quad s_i = \sin\theta_i. \end{gathered} \tag{2.17}$$

For Centaurus A the observation angle is $\theta_5 = \theta_0 = 68°$ and for $E_\gamma = 10\,\text{GeV}$, $M_B = 200\,\text{GeV}$ and $M_E = 215\,\text{GeV}$ the differential cross section is shown in 2.3. There are two peaks each related to the different modes of resonance due to the propagators Σ_{12} and Σ_{34}, one of them varies so slowly with E_γ that it can be taken to occur always at the same energy $E_e^* \approx M_E - M_B$, the second one varies much faster with E_γ and appears as a mobile peak on this graph moving to the right as the energy of the photon E_γ increases. We observed that the first resonance is (almost always) dominant, i.e., it is higher by a factor of 10 or more.

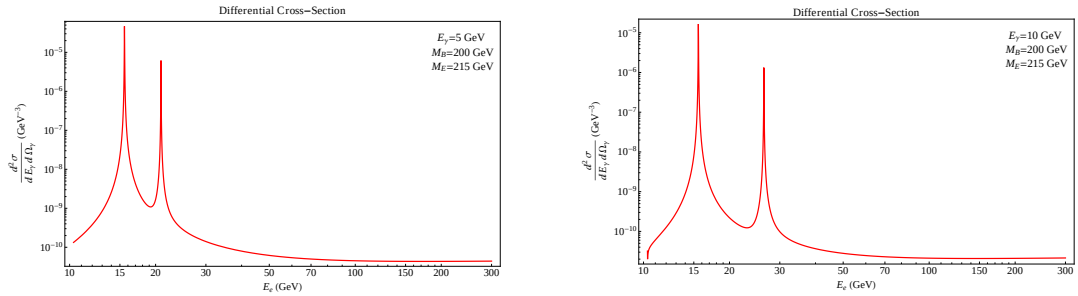

Figure 2.3: The differential cross section for $B_H + e^- \to B_H + e^- + \gamma$ for photon energy $E_5 = 5\,\text{GeV}$ (left) and $E_5 = 10\,\text{GeV}$ (right) as a function of the incoming electron energy. The resonance located near 15 GeV is due to pieces of the amplitude-squared which get contributions from diagrams S_2 and S_3 (which depend on the propagator term Σ_{12}), while the second resonance located near $22-23\,\text{GeV}$ (left) or 27 GeV (right) originates from diagrams S_1 and S_3 (which depend on the propagator term Σ_{34}).

2.2.4 Gamma-ray Flux form DM Particles Scattered by SM Particles

Putting all of the pieces together it is possible to compute the gamma-ray flux from Centaurus A AGN jet particles scattering of DM particles in the halo close to the core. Note that usually what is reported is the spectral energy distribution (νS_ν) which is related to the flux as:

$$\nu S_\nu = E_\gamma^2 \times \frac{d\Phi_\gamma}{dE_\gamma}. \tag{2.18}$$

The spectral energy distribution is shown in Figure 2.4 for both 5 and 6 dimensions[8]. In both cases it is observed a rise and then a very sharp cutoff follow by a monotonic decline. The shape is different from the characteristic power law followed by most known astrophysical processes. The cutoff corresponds to a value close to the difference of the two KK particles, i.e., the first peak of the cross section; the slow decline afterwards is due to the second peak and the fact that it keeps moving with the energy available for the photon (with the energy of the initial electron), a fixed the second peak would produce a two hump figure instead of the single hump observed. It is important to note that the inclusion of the finite resolution of the detector is going to soften this feature.

A final remark on computational efficiency is necessary, although a full calculation for one set of values of the parameters was done, the time consumed was too long. Therefore, after checking for consistency and accuracy, the implementation of the collinear approximation suggested in (Gorchtein et al. 2010) was made and it improved by several orders of magnitude the time at a small cost in

[8]The 5 dimensional case was published before and it was used as a sanity check for the approximations made to the 6 dimensional case.

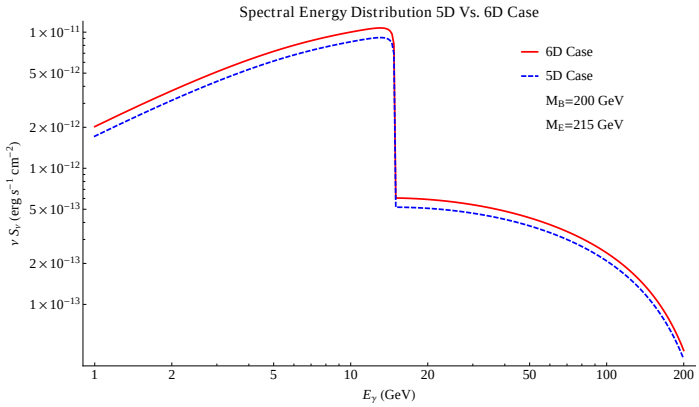

Figure 2.4: The spectral energy distribution νS_ν as function of the photon energy E_γ from the interaction of WIMPs with the AGN jets of Centaurus A. Note that 5D case refers to a comparison to the model studied in (Gorchtein et al. 2010) and 6D case corresponds to the model studied in this work.

accuracy (several values of the parameters were checked and for the final calculation of the study which includes a fit to data a faster algorithm was required). In the collinear approximation, one assumes that the difference between the two particles is small, that the final photon aligns with the final electron and that the main contribution comes from the resonances (mainly pure s-channel diagrams or mixtures of them). A complete account of the calculation can be found in Appendix B on page 76.

2.3 Gamma-rays from DM Annihilation

The calculation of the gamma-ray flux from DM annihilation depends quadratically on the density of DM (two DM particles have to get close together to interact). Therefore the flux is given by:

$$\left(\frac{d\Phi}{dE_\gamma}\right)_{ann.} = \frac{1}{8\pi M_B^2 d_{AGN}^2}\int_{r_{min}}^{r_0} 4\pi r^2 \rho_{DM}^2(r)\,dr \sum_f \langle\sigma\beta\rangle_f \frac{dN_\gamma^f}{dE_\gamma} \rightarrow$$
$$\left(\frac{d\Phi}{dE_\gamma}\right)_{ann.} = \frac{\langle\sigma\beta\rangle_{tot}}{8\pi M_B^2 d_{AGN}^2}\int_{r_{min}}^{r_0} 4\pi r^2 \rho_{DM}^2(r)\,dr \frac{dN_\gamma}{dE_\gamma} \tag{2.19}$$

where the summation is over all final states with at least one photon and $^{dN_\gamma^f}/_{dE_\gamma}$ is the normalized photon spectrum per annihilation.

The total gamma-ray from annihilation spectrum has two components:

1. Continuum. It is expected that pairs of LKPs annihilate predominantly into pairs of electroweak bosons WW and ZZ, SM Higgs bosons HH and (if heavy enough) top quark pairs

$t\bar{t}$. To compute the continuum gamma-ray spectrum from these annihilations we use the micrOMEGAs code (Belanger et al. 2011) for the chiral square model. With a Higgs mass around $M_H = 125\,\mathrm{GeV}$ and a DM particle slightly heavier than the top, but inside the allowed range derived from the density relic constraint, of $M_B = 200\,\mathrm{GeV}$, we found the annihilation fractions are roughly 48% $B_H + B_H \to W + W$, 28% $B_H + B_H \to H + H$, 22% $B_H + B_H \to Z + Z$ and 2% $B_H + B_H \to t + \bar{t}$ and the total flux cross section is $\langle \sigma\beta \rangle = 2.40 \times 10^{-26}\ \mathrm{cm}^3/\mathrm{s}$.

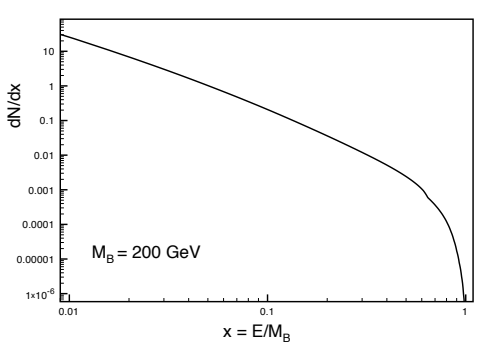

(a) The differential photon spectrum per annihilation event as a function of the fractional photon energy $x = E_\gamma / M_B$ for $M_B = 200\,\mathrm{GeV}$.

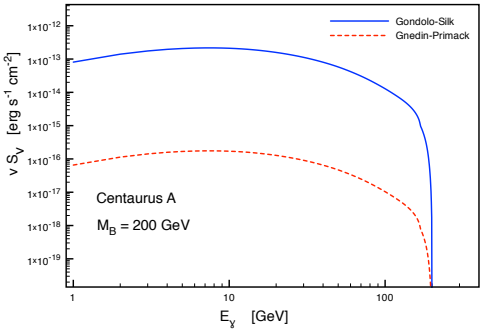

(b) The spectral energy distribution $\nu S_\nu = E_\gamma^2 \times {}^{d\Phi_\gamma}/_{dE_\gamma}$ versus the photon energy for Centaurus A for two choices of the dark matter density profile.

Figure 2.5: Gamma ray spectra from continuum WIMP annihilations.

The differential photon spectrum dN/dx as function of the energy of the photon $x = E_\gamma / M_B$ is shown in Figure 2.5a. As was pointed out by Bertone et al. (Bertone et al. 2009), in contrast to other models, the continuum spectrum from the chiral square model sharply decreases well before the value of the WIMP mass M_B. They explained that there are many annihilation modes that do not produce a photon ("photon unfriendly" modes), consisting of massive particles which are unlikely to radiate high-energy photons (the signal that we are looking for). The majority of the produced photons come from radiation (or after hadronization, decays of π^0's) from the even softer decay products of the particles produced in the primary annihilation (therefore being less energetic).

The density dependence is quadratic and Figure 2.5b shows the results for two different model of the DM density. The three orders of magnitude of difference are due to the "shallowness" of the Gnedin-Primack (GP) profile compared to the GS model, if the density effect was important in the scattering case in the annihilation is much more important and

the smaller number of particles to interact in the GP model shows it. Finally combining and comparing the contribution to the spectrum from the scattering (spectrum from jet-halo interactions) and the continuum it is clear that the scattering is dominant and the continuum is at best a tenth of the total as can be seen in Figure 2.6.

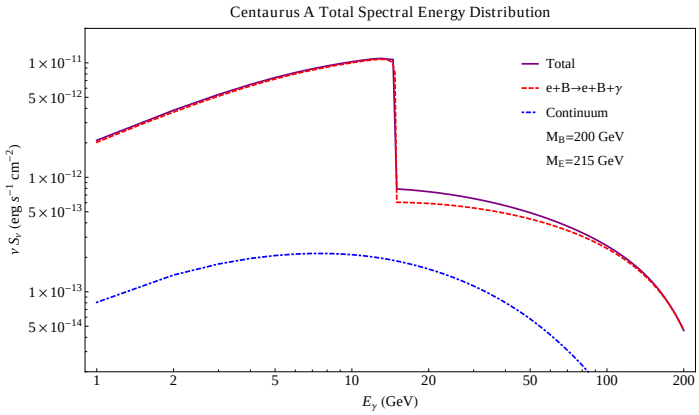

Figure 2.6: Total spectral energy distribution for the process $e + B$ with one or two final photons (leading order and one loop) including continuum emission from dark matter annihilation (but not line emission).

2. Line Emission. In the chiral square model the DM particle is a scalar; therefore, any annihilation with two final particles ($B_H + B_H \to \gamma + X$), one of them being a photon, implies that the other particle has to be a vector particle; this gives us three possible choices for X: a photon, a neutral weak boson Z or the first vectorial KK excitation of the hypercharge boson $B^{(1,1)}$. In Bertone et al. (Bertone et al. 2009) it was shown that it is possible to get several and well separated lines (even after including the effect of detector resolution) from a specific source like the center of the Milky Way.

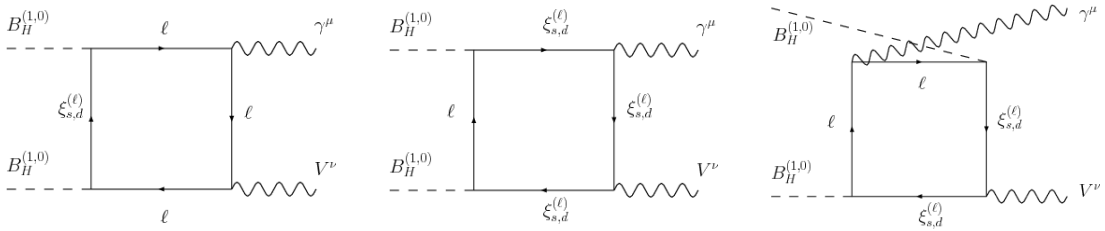

Figure 2.7: Example Feynman diagrams for the process $B_H + B_H \to \gamma + V$. $\xi^{(\ell)}_{s,d}$ are the gauge eigenstates for the (1,0) excitations of the SM leptons (ℓ).

The contribution to the line spectra come from loop diagrams like the ones shown in Figure 2.7 on the previous page. The amplitude for each diagram can be written as:

$$\mathcal{M} = \epsilon_A^{\mu*}(p_A)\,\epsilon_B^{\nu*}(p_B)\,\mathcal{M}^{\mu\nu}(p_1, p_2, p_A, p_B) \tag{2.20}$$

where number subscripts are for initial states and letter subscripts for final states (A for the photon and B for the second vector state), ϵ's are the polarization four-vectors of the final vector particles. The tensor $\mathcal{M}^{\mu\nu}$ has two free indices and it should be expanded in terms of the metric tensor and combinations of the momenta four-vectors available:

$$\mathcal{M}^{\mu\nu} = Ag^{\mu\nu} + \sum_{i,j} B_{ij} p_i^\mu p_j^\nu. \tag{2.21}$$

However it was shown in (Bertone et al. 2009) that the dominant contribution comes from the metric tensor term (only if the DM is massive enough such as it can be treated non-relativistically, i.e., $p_1 = p_2 \approx (M_B, 0, 0, 0)^T$). The results for $\gamma + \gamma$, $\gamma + Z$ and $\gamma + B^{(1,1)}$ cross sections as a function of M_B for the KK masses $M_E = 1.2M_B$ and $M_{B^{(1,1)}} = 1.6M_B$ are shown in Figure 2.8.

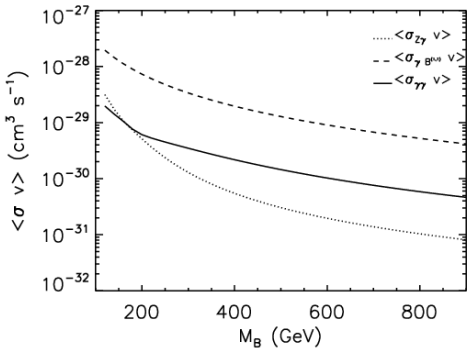

Figure 2.8: The flux cross sections for $B_H + B_H \to \gamma\gamma, \gamma Z$ and $\gamma B^{(1,1)}$ as a function of the DM particle mass. Source: Bertone et al. (Bertone et al. 2009).

In each case the spectra will depend on the width of the decaying particle (no width for a photon, i.e., a delta function at the mass of the DM particle M_B), and it can be parametrize by (Bertone et al. 2009):

$$\begin{aligned} \frac{dN_\gamma^V}{dE} &= \frac{4M_B M_V \Gamma_V}{f_1 f_2} \\ f_1 &= \left[\tan^{-1}\left(\frac{M_V}{M_B}\right) + \tan^{-1}\left(\frac{4M_B^2 - M_V^2}{M_V \Gamma_V}\right)\right] \\ f_2 &= \left[\left(4M_B^2 - 4M_B E_\gamma - M_V^2\right)^2 + \Gamma_V^2 M_V^2\right]. \end{aligned} \tag{2.22}$$

2.4 Results

So far we have included the DM related gamma-ray flux, but there exist a background due to astrophysical processes. The model for this astrophysical background follows a power law ${}^{d\Phi_{\rm bkg}}/_{dE_\gamma} = A_{\rm b} E_\gamma^{\delta_{\rm b}}$ where the photon energy is measured in GeV. Assuming that the photons do not interact with anything from the source to the detector and assuming that the detector will smear the measurement with a gaussian kernel, the total differential flux is:

$$\begin{aligned} \frac{d\Phi_{tot}}{dE_\gamma} &= G_0\left(E'_\gamma, E_\gamma\right)\left(\frac{d\Phi_{\rm bgk}}{dE'_\gamma} + \frac{d\Phi_{\rm cont.}}{dE'_\gamma} + \frac{d\Phi_{\rm line}}{dE'_\gamma} + \lambda_{\rm AGN}\frac{d\Phi_{\rm AGN}}{dE'_\gamma}\right) \qquad \text{with} \\ G_0\left(E'_\gamma, E_\gamma\right) &= \frac{1}{\sqrt{2\pi}\,\sigma_{exp}} e^{-\left(E'_\gamma - E_\gamma\right)^2/2\sigma_{exp}^2} \end{aligned} \tag{2.23}$$

where σ_{exp} is the experimental resolution, i.e., $\sigma_{exp} = 0.1E'_\gamma$ for the Fermi LAT detector. Note that the contribution from the AGN is scaled with $\lambda_{\rm AGN}$, which will be allowed to vary in the range $0.5 - 1$, and is meant as a parametrization of the uncertainty in the AGN contribution (allowing more freedom to fit the experimental data).

A bayesian algorithm was used to fit the data and the details are in Appendix C on page 81. Note that the fit has some restrictions; remember that there is relic abundance "measurement" ($\Omega_{DM}h^2 = 0.11 \pm 0.01$)[9] that constrains the possible values for the different parameters to allow the model to be viable. One possibility is that our DM candidate is the only component of the DM and then we saturate the limit. On the other hand, if the DM sector is more complex and our candidate is only a fraction of the total DM then the constraint is loose (there is some slack due to the other

[9]This uncertainty is theoretical in nature and much larger than the empirical one (0.0027).

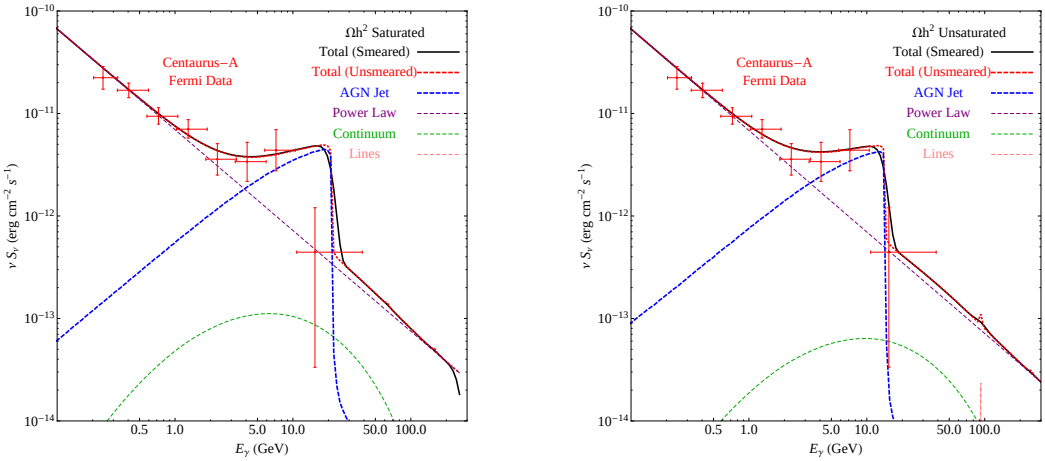

(a) Saturated photon spectrum.

(b) Unsaturated photon spectrum.

Figure 2.9: The unsaturated relic abundance case yields an energy cutoff that fits the Centaurus-A data slightly better than the saturated case. While the continuum and lines are generally suppressed below the astrophysical background, the $B^{(1,1)}\gamma$ line can appear above the continuum, offering possible detection in our own galaxy.

components). Additionally there are restrictions that come from direct searches, e.g., XENON100. To include these restrictions the following rescaling was used:

$$\sigma_{\rm SI}^{\rm meas.} = \sigma_{\rm SI}\frac{\Omega_{B_H}h^2}{\Omega_{\rm meas.}h^2}, \qquad \sigma\beta_{\gamma\,X}^{\rm meas.} = \sigma\beta_{\gamma\,X}\left(\frac{\Omega_{B_H}h^2}{\Omega_{\rm meas.}h^2}\right)^2. \tag{2.24}$$

The results are shown in Figure 2.9. First note that the power law gave similar results in both cases and the coefficients found for the saturated case are $A_{\rm b} = 6.1^{+1.0}_{-0.8}\times10^{-12}$ and $\delta_{\rm b} = -3.06\pm0.14$ (this is on the high side for the exponent for an astrophysical process); also note that the unsaturated case fits better the cutoff but both of the fits are consistent with the experimental uncertainty; and finally note that the signal from annihilation is very small but one of the lines (the one corresponding to $B^{(1,1)} + \gamma$ final state) can be detected under some circumstances.

But, why to explore a unsaturated case? It turned out that the parameters (masses) in our model are in conflict with the data unless it was adjusted as can be seen in Figure 2.10 on the following page. The problem with a more compact spectrum of particles (less difference in the masses) is that more coannihilations will occur decreasing the current density of the DM particle (Figure 2.10d). Unfortunately the drop (which is occurring at the difference of masses in our model) only fits the data if it is not the only DM in the Universe. However it is a considerable component

of it (around 50%) and that is an improvement over past experiences[10]. A rough estimate from Figure 2.10a and Figure 2.10b gives the combination $M_B = 180\,\text{GeV}$ and $M_E = 210\,\text{GeV}$, but this contradicts the evidence from Fermi LAT with a difference close to 15 GeV.

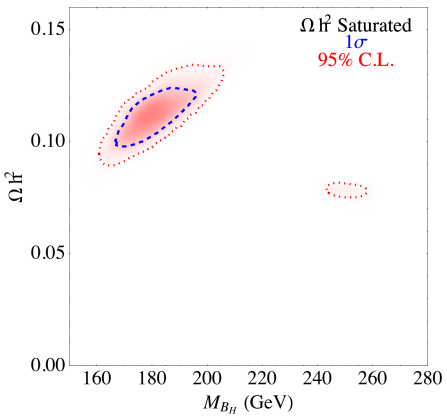

(a) Posterior distributions for the saturated case as function of DM mass and relic density. The preferred mass is centered around $M_B = 180\,\text{GeV}$ slightly lower than the selected mass.

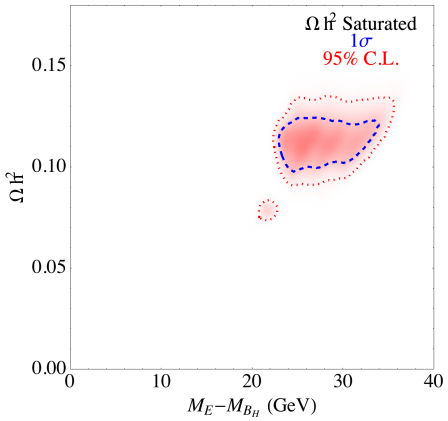

(b) Posterior distributions for the saturated case as function of difference of mass and relic density. The preferred mass difference is centered around $M_E - M_B = 30\,\text{GeV}$ doubling the selected value.

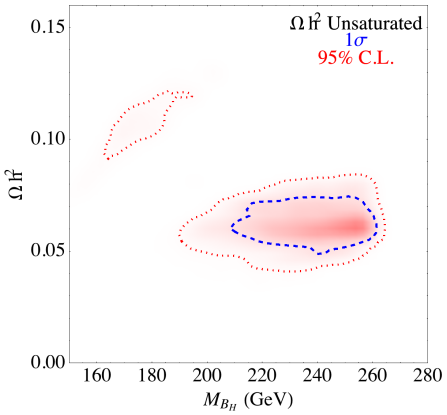

(c) Posterior distributions for the saturated case as function of DM mass and relic density. The preferred mass is centered around $M_B = 240\,\text{GeV}$ higher than the selected mass.

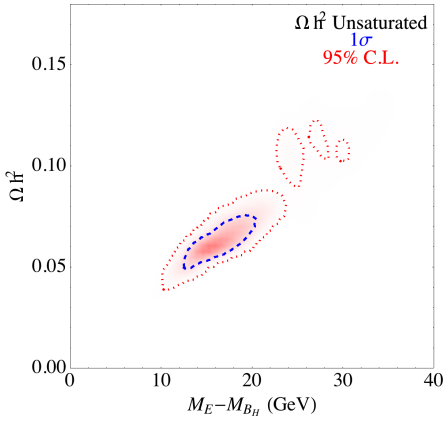

(d) Posterior distributions for the saturated case as function of difference of mass and relic density. The preferred mass difference is centered around $M_E - M_B = 17\,\text{GeV}$ very close to the selected value.

Figure 2.10: Posterior distributions for unsaturated (bottom) and saturated case (top).

Finally, in Figure 2.11 on page 39, we present associated dark matter observables. In Fig. 2.11 (top), we see the spin-independent scattering cross section for the two relic abundance

[10]It is possible to have a more complex model in which non-standard cosmological conditions are met.

cases. In the case of a saturated relic abundance, the expected cross sections are quite close to the Xenon100 limit (Aprile et al. 2012). This indicates some amount of tension within the model. However, the unsaturated case is naturally within a factor of 3-4 of the current bound. Either case is within reach of future direct detection experiments such as LUX (Akerib et al. 2013a) and Xenon-1Ton (Aprile 2012) with a cross section no lower than $\mathcal{O}(5 \times 10^{-10}$ pb).

In Figure 2.11 on the next page (bottom), we show the location and predicted cross section into the γ-ray lines $\gamma+\gamma$, $Z+\gamma$ and $B^{(1,1)}+\gamma$ and the present 4 year Fermi line search limit (Albert 2012). The $B^{(1,1)}+\gamma$ is sizable and is well positioned for Fermi line searches within our own galaxy in the near future. We find the $B^{(1,1)}+\gamma$ should have a line location of $50-100\,\mathrm{GeV}$ and cross section at the $\mathcal{O}\left(10^{-28}\ \mathrm{cm}^2/\mathrm{s}\right)$ level. The $\gamma+\gamma$ and $Z+\gamma$ lines are of similar strength. Furthermore, given the energy resolution of γ-ray experiments, they will likely be smeared together as one line at this energy. Therefore, they are combined in the contour plot as one line.

2.5 Discussion

Since the best fit in the model correspond to a mass splitting of $\mathcal{O}(15\,\mathrm{GeV})$, the relic density of B_H is lower than measured by WMAP and Planck due to coannihilation with the up-scattered state, E. Therefore, a second DM candidate is needed to explain the remaining DM of the Universe; one possibility is the axion (see page 11).

A small mass splitting between the DM candidate and the compressed spectrum associated with the first level excitation, the outlook for searches at the LHC for discovering this scenario are gloomy. The main difficulty being that the cuts are going to get rid of the soft decay products. Note that the null searches for new heavy states in models such as SUSY have not precluded this scenario and a mass scale of $\mathcal{O}(200\,\mathrm{GeV})$ is within reach of a future ILC at 250 or 500 GeV. There, the cleaner background and more precise control over initial state energy may allow a discovery.

It is worth noting that in the presence of brane kinetic terms, the masses in extra dimension models are allowed to vary more freely. In this case, while the strength of coannihilation between B_H and the compressed spectrum will be weakened, we can say that coannihilation between B_H and E will take place to some level due to the AGN jet data requiring a $10-20$ GeV mass splitting. However, the searches at the LHC may uncover the decay of, say, $Q^{(1,0)} \to B_H + q$ with a sufficient mass splitting.

We expect that the Fermi LAT should be able to discover the $B^{(1,1)}+\gamma$ line and future direct detection experiments such as LUX (Akerib et al. 2013a) and Xenon-1Ton (Aprile 2012) are

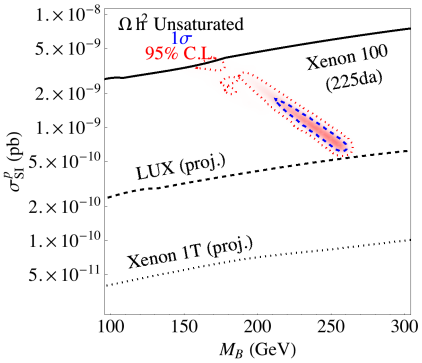

(a) Posterior distribution in spin independent cross section and DM mass plane for unsaturated relic density.

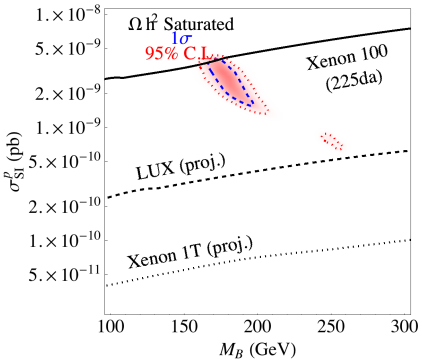

(b) Posterior distribution in spin independent cross section and DM mass plane for saturated relic density.

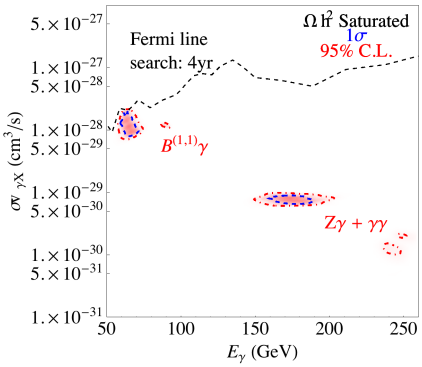

(c) Posterior distribution in cross section flux of lines and energy of the photon plane for unsaturated relic density.

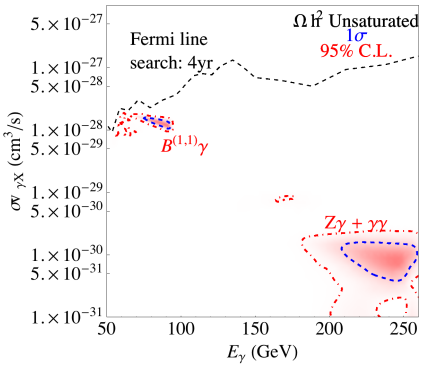

(d) Posterior distribution in cross section flux of lines and energy of the photon plane for saturated relic density.

Figure 2.11: The dashed (dotted) contour contains the 1σ (95%) C.L. regions, respectively. Either scenario is easily probed by the LUX and Xenon 1T experiments.

well positioned to probe the entire scattering cross section, assuming the B_H relic abundance is not suppressed too much. The Fermi LAT and HESS measurements on Centaurus-A should also provide additional statistical power to confirm or refute this scenario directly.

Chapter 3

Top Portal DM

In the preceding chapter, the possibility of detection of "standard" DM by looking in different parts of the Universe was explored. In this chapter slightly more "exotic" model of DM is studied. For starters this model is more basic than the one used before and is classified as a "simplified model" in the sense that only the minimum content is introduced and it does not pretend to explain other phenomena than DM itself (Beltran et al. 2009; Fan et al. 2010; Fitzpatrick et al. 2013; Beltran et al. 2010; Goodman et al. 2011; Bai et al. 2010; Goodman et al. 2010). An advantage of this approach is that the simplified model can be mapped to more complex models like SUSY, UED, etc (the new particles and interactions may have some resemblance or even be identical to particles and interactions in those models). The term exotic requires some explanation though, for a long time the research was focus on the more complex models because there were other compelling reasons to believe they were an improvement, but due to their complexity some additional restrictions were imposed in the new particles and interactions added and these restrictions were associated to the model per se not on the nature of DM. Therefore with the new approach you remove those additional constraints but pay the price to look for a less ambitious goal: instead of explaining some fundamental problems you are trying to characterize DM and nothing else. This chapter is based on the paper "Dark Matter on Top" (Gomez et al. 2014).

These simplified models modify the lagrangian with a new interaction term between the DM particle and some SM particle(s), in addition to kinetic and mass terms for the new particles, of the form:

$$\Delta\mathcal{L} \sim \frac{1}{\Lambda^n}\mathcal{O}_{SM}\mathcal{O}_{DM} \tag{3.1}$$

where $\mathcal{O}_{SM}$ and $\mathcal{O}_{DM}$ are operators constructed from SM and DM fields respectively and Λ is a cutoff scale for the effective theory. Because the DM particle has to be stable or quasi-stable for periods of time comparable to the age of the Universe a new discrete symmetry is introduced to

avoid the decay of it. Thus the DM operator contains an even number of DM fields and the simplest among all of them is:

$$\Delta\mathcal{L} \sim \frac{1}{\Lambda^n} |DM|^2 |SM|^2 . \tag{3.2}$$

A nice feature of models of this form is that they result in complimentary probes of the available parameter space from direct detection and collider experiments because the same operator is responsible for the signals at these experiments (Goodman et al. 2011; Bai et al. 2010; Goodman et al. 2010; Birkedal et al. 2004; Feng et al. 2006; Cao et al. 2011; Cheung et al. 2012; Dreiner et al. 2013). However, there is a small problem with this kind of interaction, in that collider searches impose bounds for higher-dimensional operator probing the Λ scale, i.e., the high energy scale is important for the lower energy phenomenology. This is what the new approach was trying to avoid. But if you consider renormalizable interactions only the story is different, e.g., particles with weak-scale, renormalizable couplings to the SM and weak-scale masses do not present this problem.

If only one new particle is added, the DM particle (a singlet under SM interactions), then there is only one such renormalizable interaction: a quartic coupling between Higgs and DM scalar fields (Silveira and Zee 1985; McDonald 1994; Burgess et al. 2001; Patt and Wilczek 2006; Barger et al. 2008b). On the other hand, the inclusion of more than one particle opens to possibility of more interactions, the simplest being a cubic interaction:

$$\Delta\mathcal{L} = g_{DM} SM \; \widetilde{SM} \; DM \tag{3.3}$$

where the new particle ($\widetilde{SM}$) has the same charges under SM interactions as the associated SM particle to preserve gauge invariance (local charge/current conservation). The DM particle is lighter than the new particle and again a new discrete symmetry is needed to allow a stable DM particle, i.e., DM and $\widetilde{SM}$ are odd under the new symmetry.

Recently, interactions of the form of Equation (3) where the SM field is a quark have been the focus of several studies (Chang et al. 2014a; Bai and Berger 2013; DiFranzo et al. 2013). The interest on these models, for the first generation or massless quarks, is due to the possibility of getting testable signals in current and near future experiments at colliders and direct detection facilities.

The "top portal" model in which DM couples exclusively (or, at least, most strongly) to the top quark will be studied. The main reason to consider this model is the possibility of a relation between the dynamics of DM and the ElectroWeak Symmetry Breaking (EWSB) given that all the

involved masses are clustered around hundreds of GeV. If that is the case it is natural to expect to have a coupling between them (the most massive states of the SM and the new particles).

3.1 The Model

DM is assumed to be made up entirely of a fermion χ and nothing else. This fermion couples to the right-handed top quark and is a singlet under SM gauge groups. To preserve gauge invariance a new particle with the same quantum numbers as the right-handed top quark is introduced ϕ^a. The new particle is a scalar colored state, i.e., it interacts strongly with other SM particles. The full lagrangian is:

$$\mathcal{L} = \mathcal{L}_{SM} + i\chi\not{\partial}\chi - m_\chi\bar{\chi}\chi + (D_\mu\phi)^*(D^\mu\phi) - m_\phi^2|\phi|^2 + (g_{DM}\phi^*\bar{\chi}t_R + h.c.)\,^1 \tag{3.4}$$

where the covariant derivative is:

$$D_\mu = \partial_\mu - ig_sG_\mu^aT^a - iQ_teA_\mu + ie\frac{\sin\theta_W}{\cos\theta_W}Q_tZ_\mu \tag{3.5}$$

with Q_t the electric charge of the top quark in terms of the positron charge e, θ_W is the weak angle and T^a are the generators of the color group. This SM "partner" can couple to gluons, photons and Z bosons, but not to W bosons (no weak charge, i.e., weak isospin is zero for this particle as for a right-handed fermion in the SM). From now on I will call this model the Top Portal Dark Matter (TPDM).

There are three free parameters in the model (m_χ, m_ϕ and g_{DM}) but some restrictions are necessary to retain the desirable properties of the model:

- Perturbative regime, i.e., $g_{DM} < \sqrt{4\pi} \approx 3.54$, i.e., the interaction can be intrinsically strong but not super-strong ($\alpha_{DM} < 1$).
- DM particle is stable, therefore $m_\chi < m_\phi$, i.e., there is no decay mode for the DM particle.
- SM partner is unstable, therefore the length of the chain decay after the first decay $\phi \to \chi + \bar{t}^*$ is not large (otherwise the decay is highly suppressed), i.e., the difference in masses of the two new particles can be small but not too small (the smaller the difference the less phase space to decay). The decay chains in increasing order of suppression are (stopping when the final states can be on-mass shell):

[1] Remember that $t_R = P_Rt = {}^{(1+\gamma_5)t}/_2$ is simply the projection of the field into the (chiral) right-handed field.

– Large mass difference ($m_\phi - m_\chi > m_t$), $\phi \to \chi + \bar{t}$.

– Moderately large mass difference ($m_\phi - m_\chi > m_W + m_b$), $\phi \to \chi + \bar{t}^* \to \chi + W^- + \bar{b}$.

– Small mass difference ($m_\phi - m_\chi > m_b + m_c + m_s$), $\phi \to \chi + \bar{t}^* \to \chi + W^{*-} + \bar{b} \to \chi + \bar{b} + \bar{c} + s$.

– Small and negligible mass difference ($m_\phi - m_\chi > m_l$), $\phi \to \chi + W^{*-} \to \chi + l^- + \bar{\nu}_l$.

The decay width of the top partner is:

$$\Gamma\left(\phi \to \chi + \bar{t}^*\right) = \frac{g_{DM}^2}{16\pi} \frac{m_\phi^2 - m_\chi^2 - m_{t^*}^2}{m_\phi^3} \sqrt{m_\phi^4 - 2m_\phi^2\left(m_\chi^2 + m_{t^*}^2\right) + \left(m_\chi^2 - m_{t^*}^2\right)^2} \tag{3.6}$$

where m_{t^*} is the mass of the final state(s) accompanying the DM particle (including the possibility of creating an on-mass shell top quark).

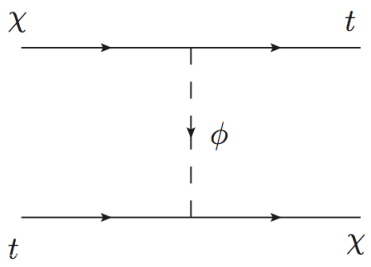

(a) The leading-order diagram would be highly-suppressed due to the smallness of the top quark PDF.

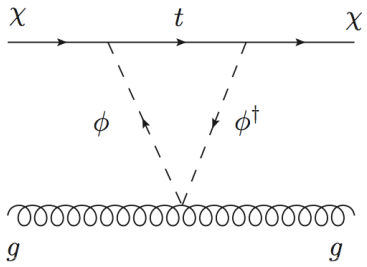

(b) The first non-vanishing contribution would come from loop-level diagrams, also highly-suppressed.

Figure 3.1: Feynman diagrams which would contribute to direct detection of TPDM.

Note that there are no restrictions coming from direct detection due to the negligible Parton Distribution Function (PDF) of the top quark in the nucleons (proton and neutron). It is clear that the only way the DM particle can interact with the nucleon is through the interchange of a top partner with a top inside the nucleon (Figure 3.1a) or through a loop with a gluon inside the nucleon (Figure 3.1b). Therefore the absence of signal only indicates that the required interaction for direct detection is highly suppressed specially for the masses considered in this work.

3.2 Relic Density

The DM particle is assumed to be in equilibrium with the thermal bath at the early stages of the Universe, i.e., it is a thermal relic. The Boltzmann "equation" for the DM particle can be cast in the general form (annihilation process only):

$$\begin{aligned}\frac{dY_\chi}{dx} &= -\frac{\lambda\langle\sigma\beta\rangle}{x^2}\left(Y_\chi^2 - CY_\chi - Y_\chi^{eq\cdot}Y_{\bar{\chi}}^{eq\cdot}\right)\\ \frac{dY_{\bar{\chi}}}{dx} &= -\frac{\lambda\langle\sigma\beta\rangle}{x^2}\left(Y_{\bar{\chi}}^2 + CY_{\bar{\chi}} - Y_\chi^{eq\cdot}Y_{\bar{\chi}}^{eq\cdot}\right)\end{aligned} \tag{3.7}$$

where $C = Y_\chi - Y_{\bar{\chi}}$ is the constant asymmetry between particles and antiparticles and all other quantities except λ are functions of $x = {}^{m_\chi}/_T$ (Iminniyaz et al. 2011). Only the symmetric case is considered here ($C = 0$), therefore the two equations coalesce to only one differential equation ($Y_\chi = Y_{\bar{\chi}}$). Note that time and temperature are related and the evolution from small to large values of t are mapped to the evolution from large to small values of T.

The traditional approach to solve the Boltzmann equation is called the freeze-out approximation in which the relic density follows the equilibrium value closely up to the freeze-out point in which the density "freezes-out" (hence the name) and departs from its equilibrium value and starts approaching its limiting value (Iminniyaz et al. 2011; Gondolo and Gelmini 1991; Profumo 2013). A second approximation is made when the DM is not relativistic ($\beta \lesssim 0.3$) which simplifies the flux cross section (up to second order in β):

$$\begin{aligned}\sigma\beta \approx \frac{1}{2}\frac{3g_{DM}^4\sqrt{1-r}}{32\pi m_\chi^2\left(1-r+R\right)^2}\Bigg[1 + \frac{\left(2r^2-10r+11\right)R^2}{24\left(1-r\right)\left(1-r+R\right)^2}\beta^2\\ + \frac{2\left(2r^2-2r-9\right)\left(1-r\right)R + \left(2r^2+6r-5\right)\left(1-r\right)^2}{24\left(1-r\right)\left(1-r+R\right)^2}\beta^2\Bigg]\end{aligned} \tag{3.8}$$

where $r = \left({}^{m_t}/_{m_\chi}\right)^2 < 1$ and $R = \left({}^{m_\phi}/_{m_\chi}\right)^2 > 1$. Note the additional factor of one half, shown explicitly, for non-identical particles (Gondolo and Gelmini 1991). This result is typically expressed in terms of the "wave" coefficients $\sigma\beta \approx a + b\beta^2$ with a the "s-wave" coefficient and b the "p-wave" coefficient. In our model, for most of the parameter space, the coefficient of the s-wave is dominant (see Figure 3.2a on page 45) and can be ignored in most cases.

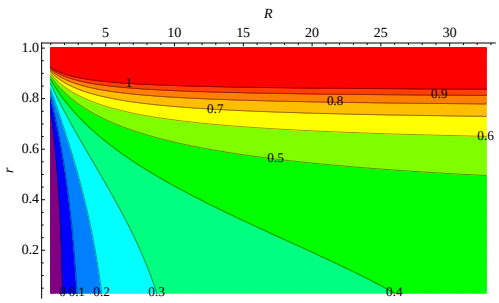

(a) Ratio of the p-wave coefficient to the s-wave coefficient as function of m_ϕ and m_χ for $m_t \approx 175\,\text{GeV}$. Only when the mass of the DM particle is almost degenerate with mass of the top quark the p-wave coefficient starts to be relevant.

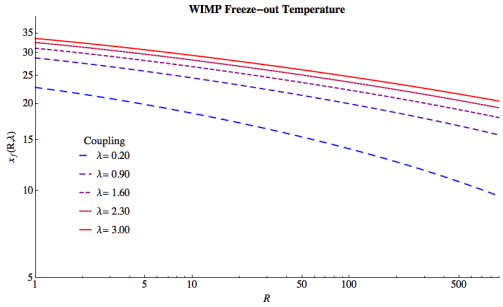

(b) Freeze-out temperatures as function of $R = \left({}^{m_\phi}/_{m_\chi}\right)^2$ for several values of the coupling constant and $m_t \approx 175\,\text{GeV}$. Note that the values are greater than the minimum safe value for the approximation to be valid.

Taking the thermal average is trivial now and the result is well known $\langle\sigma\beta\rangle \approx a + {}^{6b}/_{x}$. The next step is to find the temperature of freeze-out x_F, for this the non-linear equation has to be solved:

$$\begin{aligned} \delta\left(\delta+2\right)\frac{s_m}{H_m}Y_\chi^{eq.}\left(x\right)\frac{\langle\sigma\beta\rangle}{x} &= x-\frac{3}{2} \qquad \text{with} \\ Y_\chi^{eq.}\left(x\right) &= \frac{45g}{2^{5/2}\pi^{7/2}g_*}x^{3/2}e^{-x} \qquad \text{and} \\ \frac{s_m}{H_m} &= \frac{\frac{2\pi^2 g_*}{45}m_\chi^3}{\frac{\pi}{M_{Pl}^{red.}}\sqrt{\frac{g_*}{90}}m_\chi^2} = \frac{2^{3/2}\pi\sqrt{g_*}M_{Pl}^{red.}m_\chi}{\sqrt{45}} \end{aligned} \tag{3.9}$$

where g_* is the number of degrees of freedom for that temperature, g is the number of degrees of freedom associated with the field (4 for a Dirac's fermion), $M_{Pl}^{red.} = {}^{M_{Pl}}/_{\sqrt{8\pi}}$ is the reduced Planck mass and δ is a constant choose to obtain a closer solution to the full solution, usually in the range $1-2$ (Gondolo and Gelmini 1991) the results should be close to $x_F \approx 25$ (see 3.2b on page 45). Finally, the relic density can be approximated by:

$$\Omega_{DM}h^2 \approx \frac{1.07\times10^9/\,\text{GeV}}{M_{Pl}\sqrt{g_*}}\,\frac{x_F}{a+{}^{3b}/_{x_F}} \tag{3.10}$$

where Ω_{DM} is the normalized DM density and h is the Hubble parameter. In principle this is a prediction of the model but it is possible to invert the roles and try to deduce the value of the parameters given that Equation (3.10) is correct and the value on the left hand-side is the observed one, i.e., fixing the value of the coupling constant finding the values of the masses such as the calculated relic density is equal to the observed relic density.

Although very popular, this approach has some known problems. First the non-relativistic approximation induces an error of a few percent ($\sim 5\%$) for the slightly relativistic DM particles and the actual measurement is more precise than that. The effect of coannihilations has been completely neglect which usually is not that bad but it is known that as soon as new channel come into effect in the cross section the approximation in a series power becomes useless due to the divergence of the derivative at that point. This second point is particularly problematic when the masses are almost degenerate and other processes can affect the calculation more. Some examples of coannihilation processes include $\phi + \phi^\dagger \to g + g$, $\chi + \phi^\dagger \to t + g$, $\phi + \phi^\dagger \to \gamma g$ and $\chi + \phi^\dagger \to b + W^+$ (see the second and third Feynman diagrams of Figure 3.2).

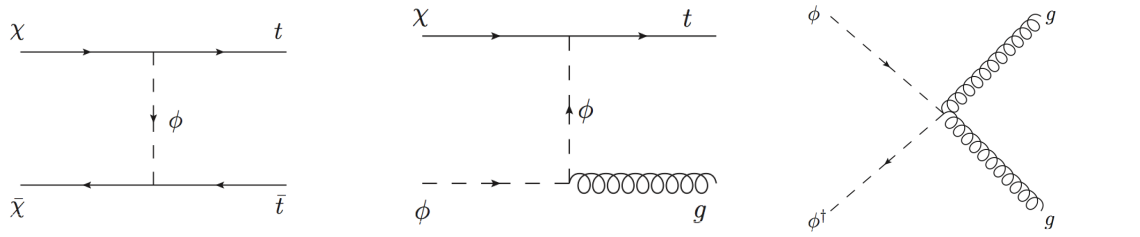

(c) DM annihilation $\chi + \bar{\chi} \to t + \bar{t}$.

(d) Coannihilation channel with DM $\chi + \phi \to t + g$.

(e) Coannihilation channel without DM $\phi + \phi \to g + g$.

Figure 3.2: Feynman diagrams which contribute to dark matter freeze-out.

To avoid the complications mentioned in the last paragraph some solutions have been created by the community and we choose to work with micrOMEGAs (Belanger et al. 2014b) which includes all these effects. As noted before, the results do not differ significantly below the threshold for the coannihilation processes but once they enter the picture the result varies considerably. The results for the fit to the measured value of the relic density from WMAP (Bennett et al. 2013) and Planck (Ade et al. 2013) are shown in Figure 3.3 on the following page. In the plot, we show contours in the $m_\phi - m_\chi$ plane for various couplings g_{DM} which satisfy the relic density constraint. The importance of co-annihilation effects is evident in the long tails of the contours as the masses approach the degenerate limit.

This concludes our "cosmological" tour with TPDM. In the following sections the analysis for collider searches (LHC) and indirect detection will be covered but including only values of the parameters (g_{DM}, m_χ and m_ϕ) that give the correct relic density.

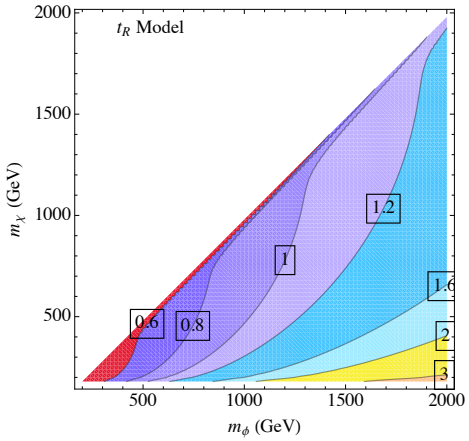

Figure 3.3: The WIMP and scalar partner masses (for various couplings) which result in the correct relic density of DM as measured by WMAP (Bennett et al. 2013) and Planck (Ade et al. 2013).

3.3 Collider Searches: LHC Prospects

The production of TPDM at LHC occurs through the production of the colored scalar mediators (ϕ) as shown in Figure 3.4. The behavior of these particles is completely analogous to scalar quarks in SUSY models. Note that our simplified model does not include a chargino component and that makes a difference compared to SUSY analysis and no mapping is possible. Model independent analysis are available, but with restricted m_χ and limited luminosity (Aad et al. 2012a).

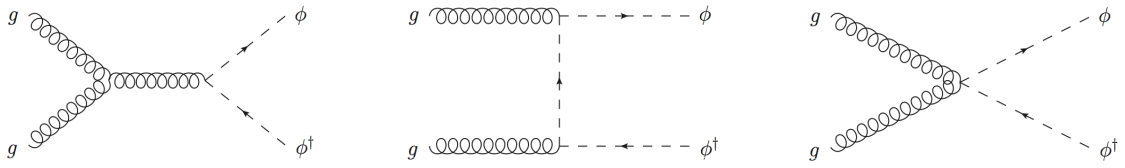

Figure 3.4: Feynman diagrams that contribute to the production of TPDM at the LHC.

The analysis for signals at LHC is based on the simulation of the process:

$$p + p \to \phi + \phi^\dagger \to (t + \bar{\chi}) + (\bar{t} + \chi) \to b + \bar{b} + \ell^\pm + j + j + \not{E}_T \tag{3.11}$$

using Madgraph5[2] (Alwall et al. 2011). The only tree-level decay is to a DM particle and a top quark[3] ($\phi \rightarrow \bar{\chi} + t$), using the narrow width approximation the cross section for the final state $t + \bar{\chi} + \bar{t} + \chi$ depends on the production of the colored scalar particle. Therefore, the cross section is determined by m_ϕ and g_{DM} and corresponds to the first case on the list on page 42.

While the background processes that affect the signal are:

$$\begin{aligned} p + p &\rightarrow \bar{t} + t, \\ p + p &\rightarrow W^{\pm} + j \end{aligned} \tag{3.12}$$

where the first process is the dominant one.

We assume efficiencies of b jet tagging of 70% for $p_T > 30\,\mathrm{GeV}$ and $\eta_b < 2.4$ consistent with the multivariate tagging suggested for the LHC luminosity upgrade (Collaboration 2014). The mistagging rate for the charm quarks is given by:

$$\epsilon_{c\rightarrow b} = 10\% \qquad \text{for} \quad p_T(c) > 50\mathrm{GeV} \tag{3.13}$$

while the mistagging rate for a light quark is:

$$\epsilon_{u,d,s,g\rightarrow b} = 2\% \qquad \text{for} \quad p_T(j) > 250\mathrm{GeV} \tag{3.14}$$

$$\epsilon_{u,d,s,g\rightarrow b} = 0.67\% \qquad \text{for} \quad p_T(j) < 100\mathrm{GeV}. \tag{3.15}$$

Over the missing range a linear interpolation of fake rates is done (Baer et al. 2007). Including pileup can worsen the result up to 20% (Collaboration 2014). Finally the detector resolution smearing is modeled by:

$$\frac{\delta E}{E} = \frac{a}{\sqrt{E}} \oplus b \tag{3.16}$$

with $a = 50\%$ and $b = 3\%$ for jets and $a = 10\%$ and $b = 0.7\%$ for photons.

A cut-based analysis and a multi-variate analysis (MVA) which relies on relevant kinematic variables are studied. For either case, we require the following tags:

$$n_b^{\mathrm{tag}} = 2, \qquad n_j^{\mathrm{tag}} = 2, \qquad n_\ell^{\mathrm{tag}} = 1. \tag{3.17}$$

[2]The missing energy is due to two DM particles and one neutrino.

[3]Only three vertices are possible for the colored scalar particle: a decay, an annihilation and scattering by a gluon.

For the cut-based analysis, we apply cuts on $\Delta R_{ab} = \sqrt{(\varphi_a - \varphi_b)^2 + (\eta_a - \eta_b)^2}$, the separation of two objects in the $\eta - \varphi$ plane. The cuts we apply are:

$$\begin{aligned} \Delta R_{jj,b\bar{b},bj} &> 0.4, & \Delta R_{j\ell,b\ell} > 0.2, \\ p_T(j) &> 25 \text{ GeV}, & |\eta_j| < 2.4, \\ p_T(e,\mu) &> 25, 20 \text{ GeV}, & |\eta_{e,\mu}| < 2.5. \end{aligned}$$

As pointed out in Footnote 2 on page 48 the missing energy should be considerable and a cut of $\not{E}_T > 100\,\text{GeV}$ removes most of the background altering the signal very little. We then require that one tagged b-jet and two additional jets reconstruct the hadronically decaying top:

$$|M_{bjj} - m_t| < 20 \text{ GeV} \tag{3.18}$$

and note the other b-tag and charged lepton originate from the other, leptonically decaying top quark. The transverse cluster mass $M_T\left(b\ell, \not{E}_T\right)$ is a suitable variable for this side of the decay (Barger et al. 1988):

$$M_T(a,b) = \left(|p_T(a)| + |p_T(b)|\right)^2 - \left(p_T(a) + p_T(b)\right)^2 \tag{3.19}$$

where the observable cluster is $a = b\ell$. This variable generically has an upper bound which is related to the mass of the parent particle, $M_T(a,b) \leq M_{ab}$. Since the typical $\not{E}_T$ distribution from a SM t-quark decay is bounded by m_t, we find the signal can be isolated if it has an appreciable cross section above $M_T(b\ell, \not{E}_T) > 200\,\text{GeV}$.

Another strong discriminator is the azimuthal angle between ℓ and $\not{E}_T$. In the $t\bar{t}$ SM background, the leptonically decaying W-boson does not often decay near rest as it is boosted from the top quark decay. Therefore, the ℓ and ν_ℓ directions are correlated and close together. This is contrasted with the signal topology in which the ℓ is paired with the ν_ℓ from the W-decay as in the $t\bar{t}$ background, but the additional $\chi\bar{\chi}$ system disrupts this correlation. Therefore, we expect to see a separation among the signal and background in this $\Delta\varphi_{\ell,\not{E}_T}$ observable.

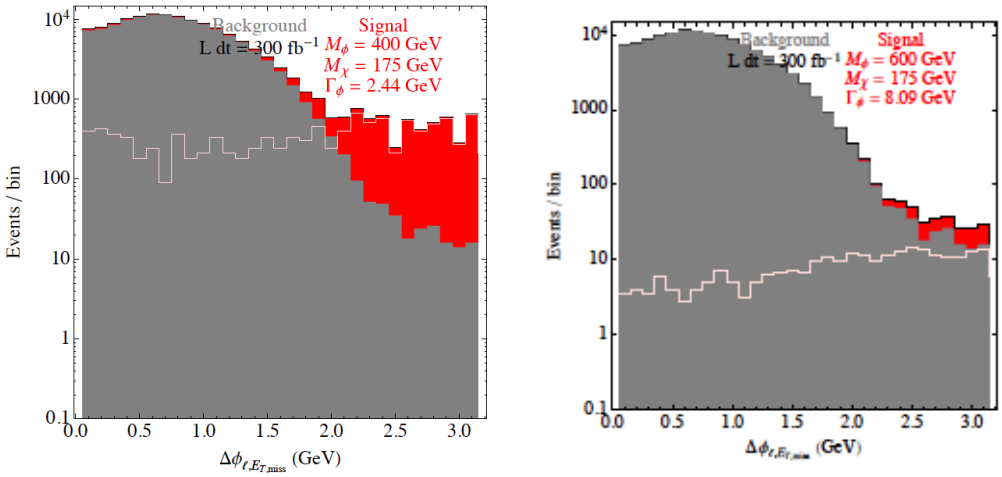

Figure 3.5: Signal and background for typical values of the variables after cuts were applied.

Furthermore, in addition to the $\not{E}_T$, M_T and $\Delta\varphi_{\ell,\not{E}_T}$ cuts, we observe that each ϕ is produced back-to-back. Therefore, the total transverse momentum carried off in either side of the ϕ decay should be balanced[4]

$$p_T(\phi_h) = -p_T(\phi_\ell), \tag{3.20}$$

where we denote ϕ_h and ϕ_ℓ as the ϕ which decays through a hadronically and leptonically decaying top quark, respectively. Therefore, one can relate the $\not{E}_T$ from both sides of the decay

$$\begin{aligned} \not{E}_T^\ell &= \frac{1}{2}(\not{E}_T^{\mathrm{obs}} + p_T(t_h) - p_T(b\ell)), \\ \not{E}_T^h &= \frac{1}{2}(\not{E}_T^{\mathrm{obs}} - p_T(t_h) + p_T(b\ell)), \end{aligned}$$

where $\not{E}_T^\ell$ and $\not{E}_T^h$ denote the missing energy from the leptonic and hadronic sides of the ϕ decays, and $\not{E}_T^{\mathrm{obs}}$ is the observed missing energy. The M_T variable applied to both sides of the event offers additional discrimination power. Specifically, the difference between the leptonic and hadronically decaying side, $M_T(\phi_h) - M_T(\phi_\ell)$, shows a modest separation in the signal and background, enough to provide an additional check of the signal.

[4]Assuming the transverse CM frame is in the lab frame. A boost to the CM frame can be made if ISR kicks the CM frame in the transverse direction.

In practice, for the cut-based analysis, an optimization of the statistical significance over the observables $M_T(b\ell, \not{E}_T)$ and $\Delta\varphi_{\ell,\not{E}_T}$, is done. Define the level of statistical significance, $\mathcal{S}$, according to (Bartsch and Quast 2005):

$$\mathcal{S} = 2\left(\sqrt{S+B} - \sqrt{B}\right), \tag{3.21}$$

where S and B are the number of signal in background events surviving cuts.

An extension the analysis to include multiple variables simultaneously is possible.This allows blend cuts together rather than perform a hard cut on a kinematic distribution sequentially. A discriminant based on a set of observables, which include: $\mathcal{O} = \left\{\not{E}_T, M_T(b\ell, \not{E}_T), \Delta\varphi_{\ell\not{E}_T}, M_T(\phi_h), M_T(\phi_\ell)\right\}$, is done.

$$\mathcal{D} = \frac{S(\mathcal{O})}{S(\mathcal{O}) + A\,B(\mathcal{O})} \tag{3.22}$$

with $S(\mathcal{O})$ and $B(\mathcal{O})$ are the normalized differential cross sections in the observable space $\mathcal{O}$. These differential cross sections are estimated via event generation. The discriminator is evaluated for an event sample, yielding a value close to 1 for signal-like events and close to 0 for background-like events. For the particular choice of $A = N_B/N_S$, the discriminant gives the probability of an event being signal (Barlow 1987). A cut may be placed on the value of $\mathcal{D}$, thereby selecting a relatively high signal event sample. Such a multivariate discriminator can offer similar sensitivity that the matrix-element, or neural network methods allow (Abazov et al. 2008).

In practice, a simplified version of the discriminant, in which correlations are ignored, is easier to conduct. This allows a more efficient estimation of the discriminator, defined as

$$\mathcal{D} = \frac{S\left\{\mathcal{O}_i\right\}}{S\left\{\mathcal{O}_i\right\} + B\left\{\mathcal{O}_i\right\}} \tag{3.23}$$

where $\{\mathcal{O}_i\}$ is the combinatorial subset of observables, $\mathcal{O}$ that go into the multivariate discriminant. In the MVA results that follow, further optimization may be done by including the correlations between observables, but we adopt this uncorrelated approach for simplicity. To maximize the significance, $\mathcal{S}$, the cut on the discriminator is varied, $\mathcal{D}_{\text{cut}}$, and this minimizes the choice of A in Equation (3.22).

3.4 Indirect Detection from Annihilation into Gamma Rays

The last possibility is to detect TPDM indirectly through the detection of high-energy radiation from outer space. In this case there are several annihilation processes that have photons in the final state, any electrically charged particle can radiate photons and rapidly moving particles tend to radiate some of their energy away (when the radiating particles are in the final state the process is call *f*inal *s*tate *r*adiation - FSR for short). Additionally sometimes the intermediate products will hadronize into neutral pions that will decay later (mostly) into two photons. These two processes produce a "boring", featureless continuum. But there are other possibilities in which the annihilation produces a photon and an additional particle ($\chi + \bar{\chi} \to \gamma + X$) through a loop (the possibilities being another photon, a neutral vector boson or a Higgs boson). The non-relativist nature of the DM particles allows to have a very narrow peak, a line on top of the continuum spectrum. At first sight it seems that these processes should be highly suppressed but if the coupling is relatively large and the masses of the particles in the loop are almost degenerate with the DM mass some enhancements happen and the line can be dominant. As usual this kind of signal is assumed to be unlikely from known astrophysical processes, i.e., it is a "smoking gun" for DM.

3.4.1 Gamma-ray Continuum from DM Annihilation

We use micrOMEGAs (Belanger et al. 2014b) to compute the continuum for DM pair annihilation. When the two new particles' masses are non-degenerate the only possibility is to create a pair of top quarks (most likely off-mass shell). It turns out that the spectrum can be split according to the source of the photons. For small energy of the photon ($E_\gamma/m_\chi \ll 1$) the main contribution comes from the decay of a neutral pion, for larger values of the energy then main source is FSR and it can be approximated by (Bringmann et al. 2008):

$$\frac{dN}{dx} \approx \frac{\alpha_{EM} Q_t^2}{\pi} \left[\frac{1 + (1-x)^2}{x} \right] \log\left(\frac{s\,(1-x)}{m_t^2} \right) \tag{3.24}$$

where $x = E_\gamma/m_\chi$ and $s \approx 4m_\chi^2$. The results are shown in Figure 3.6 on the next page for almost degenerate masses between the top and DM particle ($\Delta m = E_{\gamma max} \approx 17\,\mathrm{GeV}$). The two regimes are clearly distinguishable and the transition occurs around $x_{trans.} = 0.4$. The contribution from π^0 decay gives a "soft" spectrum due to the small phase space available (small mass difference). The second contribution coming from FSR is in general highly suppressed due to the small ratio of the masses and it has a sharp cutoff at the mass of the DM particle.

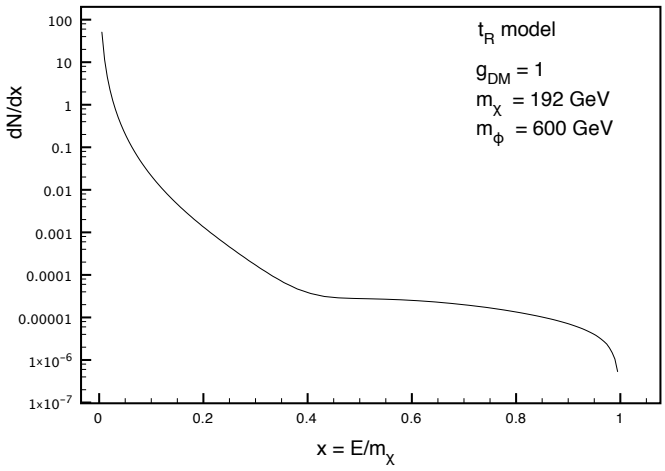

Figure 3.6: Continuum photon spectrum for a particular point in the allowed parameter space.

3.4.2 Gamma-ray Lines from DM annihilation

Each diagram in Figure 3.7 has its own peculiarities but a general form for the thermally averaged cross section flux is given by:

$$\langle \sigma_{X\gamma}\beta \rangle_{therm.} = \frac{1}{a}\,\frac{1}{32\pi m_{\chi}^{2}}\left[1-\left(\frac{m_X}{2m_\chi}\right)^2\right]\left\langle \sum_{spin}\left|\mathcal{M}^{X\gamma}\right|^2\right\rangle \tag{3.25}$$

where $X \in \{\gamma, Z, h\}$, m_X is the rest mass of the associated particle and a is the statistical factor due to final state degeneracy ($a = 1$ different final states and $a = 2$ for same final sates).

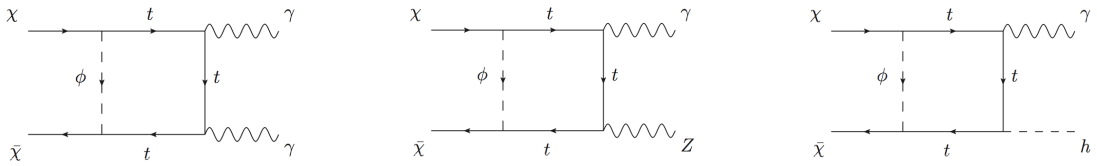

(a) Pair annihilation into two photons through a loop.

(b) A photon and a neutral vector boson in final state.

(c) A photon and a Higgs boson in final state.

Figure 3.7: Representative Feynman diagrams which contribute to the processes $\chi + \bar{\chi} \to \gamma + \gamma$, $\chi + \bar{\chi} \to \gamma + Z$ and $\chi + \bar{\chi} \to \gamma + h$ respectively.

In what follows a procedure to find the matrix element is explained for each diagram (as matter of fact it is the same procedure in all cases but the factorization and kinematical constraints vary from one to another).

3.4.2.1 Annihilation into Di-photon Final State

The annihilation of TPDM into a pair of gamma rays proceeds through loops of top quarks and ϕ particles as depicted in Figure 3.7a on the previous page. The amplitude for the process $\chi(p_1) + \bar{\chi}(p_2) \rightarrow \gamma(p_A) + \gamma(p_B)$ with A attached to vertex μ and B attached to vertex ν can be written as:

$$\mathcal{M}^{\gamma\gamma} = \epsilon^{\mu *}(p_A)\epsilon^{\nu *}(p_B)\mathcal{M}^{\gamma\gamma}_{\mu\nu} \tag{3.26}$$

where the epsilons are the polarization four-vectors for the two final-state photons. The sub-amplitude $\mathcal{M}_{\mu\nu}$ can be expanded as a linear combination of tensor structures made up of the metric tensor as well as the external momenta. In the center of momentum (CoM) the linear momentum vectors add up to zero and since the DM particles are assumed to be non-relativistic, it is possible to assign the null vector to the spatial part of the four-momenta ($p_1 \simeq p_2 \equiv p = (m_\chi, \vec{0})^T$) which reduces the number of possible tensor structures to take into account. Additionally, the four-momentum and polarization four-vector are orthogonal for photons (i.e., $\epsilon(q) \cdot q = 0$) reducing more the number of terms to include in the amplitude:

$$\begin{gathered} \mathcal{M}^{\gamma\gamma}_{\mu\nu} = \alpha_{DM}\alpha_{EM}Q_t^2 N_c\, \bar{v}(p)\, A^{\gamma\gamma}_{\mu\nu}\, u(p) \qquad \text{with} \\ A^{\gamma\gamma}_{\mu\nu} = \left(C_1 + C_2\gamma_5 + C_3 \not{p}_A + C_4 \not{p}_A \gamma_5\right) g_{\mu\nu} + \gamma_\mu\gamma_\nu \left(C_5 + C_6\gamma_5 + C_7 \not{p}_A + C_8 \not{p}_A \gamma_5\right). \end{gathered} \tag{3.27}$$

Using the Passarino-Veltman algorithm the coefficients are functions of scalar integrals only (Passarino and Veltman 1979). However, for the case of equal momentum the approach breaks down and a tweak is in order. There are some alternatives available but, for familiarity and practicality, the algebraic reduction scheme used in (Bertone et al. 2009) was chosen as working approach.

3.4.2.2 Annihilation into a Photon and Z Final State

In the case of $\chi(p_1) + \bar{\chi}(p_2) \rightarrow \gamma(p_A) + Z(p_Z)$ which is depicted in Figure 3.7b on the preceding page, again the amplitude can be written as:

$$\mathcal{M}^{\gamma Z} = \epsilon^{\mu *}(p_A)\epsilon^{\nu *}(p_Z)\mathcal{M}^{\gamma Z}_{\mu\nu} \tag{3.28}$$

where

$$\mathcal{M}_{\mu\nu}^{\gamma Z} = \frac{\alpha_{DM}\alpha_{EM}Q_t}{4s_w c_w} N_c\, \bar{v}(p)\, A_{\mu\nu}^{\gamma Z}\, u(p) \tag{3.29}$$

with the usual assignments for the trigonometric functions of the weak angle ($s_W = \sin\theta_W$, etc). In this case the tensorial sub-amplitude is more complex due to the longitudinal degrees of freedom for the neutral vector boson. The full expression is:

$$\begin{aligned} A_{\mu\nu}^{\gamma Z} &= C_1^{\gamma Z} g_{\mu\nu} + C_2^{\gamma Z}\gamma_5 g_{\mu\nu} + C_3^{\gamma Z}\, \not{p}_A g_{\mu\nu} + C_4^{\gamma Z}\, \not{p}_A\gamma_5 g_{\mu\nu} + C_5^{\gamma Z}\gamma_\mu\gamma_\nu + C_6^{\gamma Z}\gamma_\mu\gamma_\nu\gamma_5 \\ &+ C_7^{\gamma Z}\gamma_\mu\gamma_\nu\, \not{p}_A + C_8^{\gamma Z}\gamma_\mu\gamma_\nu\, \not{p}_A\gamma_5 + C_9^{\gamma Z}\gamma_\mu p_\nu + C_{10}^{\gamma Z}\gamma_\mu\gamma_5 p_\nu + C_{11}^{\gamma Z}\gamma_\mu p_{A,\nu} + C_{12}^{\gamma Z}\gamma_\mu\gamma_5 p_{A,\nu} \\ &+ C_{13}^{\gamma Z}\gamma_\mu\, \not{p}_A p_\nu + C_{14}^{\gamma Z}\gamma_\mu\, \not{p}_A\gamma_5 p_\nu + C_{15}^{\gamma Z}\gamma_\mu\, \not{p}_A p_{A,\nu} + C_{16}^{\gamma Z}\gamma_\mu\, \not{p}_A\gamma_5 p_{A,\nu}. \end{aligned} \tag{3.30}$$

3.4.2.3 Annihilation into a Photon and h Final State

The last possibility is a photon with a SM Higgs in the final state. As was explored before in Higgs in space there is a chance of enhancement, thus excluding the featureless continuum, due to the Higgs being radiated from a top quark line.

The amplitude for the process in Figure 3.7c on page 53 is given by:

$$\mathcal{M}^{h\gamma} = \epsilon^{\mu *}(p_A)\, \mathcal{M}_\mu^{h\gamma} \tag{3.31}$$

with the sub-amplitude $\mathcal{M}_\mu^{h\gamma}$ give by:

$$\mathcal{M}_\mu^{h\gamma} = \alpha_{DM}\sqrt{4\pi\alpha_{EM}}Q_t \left(\frac{m_t}{v.e.v.}\right) N_c \bar{v}(p)\, \gamma_\mu A^{h\gamma} u(p)\,. \tag{3.32}$$

The quantity $A^{h\gamma}$ can be expanded in terms of external momenta. Making the same assumptions as before (non-relativistic WIMPs, orthogonality between four-momentum and polarization four-vector for a photon) this quantity simplifies to:

$$A^{h\gamma} = C_1^{h\gamma} + C_2^{h\gamma}\gamma_5 + C_3^{h\gamma}\not{p}_A + C_4^{h\gamma}\not{p}_A\gamma_5. \tag{3.33}$$

3.4.3 The Gamma-ray Spectrum from WIMP Annihilation

Finally, putting all together and computing the total gamma-ray flux originating from the center of the Milky Way; the differential flux of gamma rays arising from DM annihilation observed in a direction making an angle ψ with the direction of the GC is given by:

$$\frac{d^2\Phi_\gamma}{d\Omega dE_\gamma}(\psi, E_\gamma) = \frac{r_\odot \rho_\odot^2}{4\pi m_\chi^2}\frac{dN_\gamma}{dE_\gamma}\int_{\text{l.o.s.}}\left(\frac{\rho(r(s,\psi))}{\rho_\odot}\right)^2\frac{ds}{r_\odot} \tag{3.34}$$

with the same definitions in Equation (2.19) on page 31 for the photon flux. Note that, in the case of $\gamma + Z$ and $\gamma + h$, the photon spectrum will deviate from a monochromatic emission due to the decay widths Γ_X from Equation (2.22) on page 35. To model the finite resolution of the detector a gaussian kernel is used as in Equation (2.23) on page 35:

$$G(E, E_0) = \frac{1}{\sqrt{2\pi}\,\sigma_{exp}} e^{-(E-E_0)^2/2\sigma_{exp}^2} \tag{3.35}$$

with the experimental uncertainty defined by $\sigma_{exp} = {}^{E_0\xi}/_{2.3}$ where ξ is the relative energy resolution of the detector.

In Figure 3.8a on the next page, a typical gamma-ray spectra for the TPDM model assuming an energy resolution of 10% and using several different DM density profiles (Navarro et al. 1996; Graham et al. 2006; Edsjo et al. 2004; Prada et al. 2004; Gnedin et al. 2004; Bertone and Merritt 2005) is shown. Note that due to detector's resolution effects, the three lines get smeared into one large bump. However, the prominence of the bump over the background is quite impressive and not typical of any other model. The main effect responsible for this is the suppression of the continuum as discussed before. A better resolution is required to be able to see two different lines (see Figure 3.8b on the following page).

Finally, a comparison between the predictions from the TPDM and the limits on the DM $\gamma\gamma$ annihilation cross section extracted from the Fermi LAT data (Ackermann et al. 2013) was made. First, sum the cross sections for $\gamma\gamma$, γZ and γh, for several different couplings, and then use the results from the relic abundance fit to determine the χ and ϕ masses (see Figure 3.9 on the next page). Since the gamma rays are assumed to be originating from a $\chi + \chi$ annihilation, the photon's energy is approximately equal to the DM particle mass. It is clear that the Fermi LAT is beginning to probe the large coupling, small mass region of the TPDM model. Over the next several years,

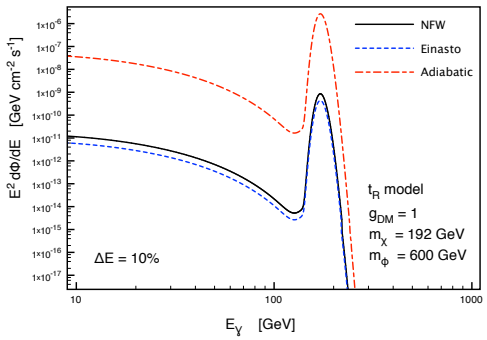

(a) A typical gamma-ray spectrum for various choices of the DM density profile and the typical energy resolution. The resolution is not good enough to allow to see the different lines present but just a single bump.

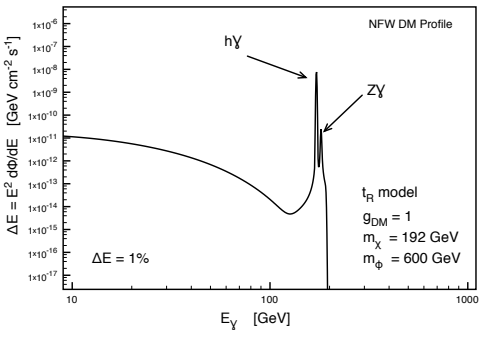

(b) Measured gamma-ray spectrum for a detector. In this case, the $h + \gamma$ and $Z + \gamma$ lines are clearly discernible, while the $\gamma + \gamma$ line remains obscured. An improvement by a factor of 10 in resolution is required!

Figure 3.8: Gamma-ray line flux from GC for typical and improved resolution.

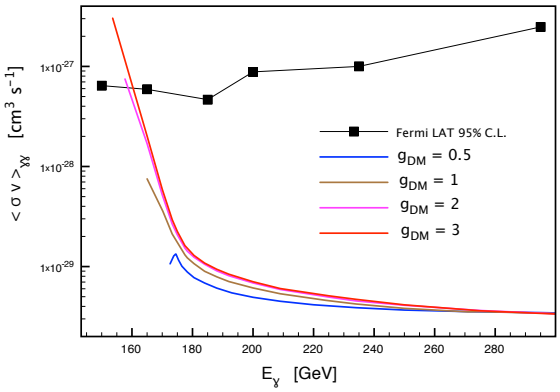

Figure 3.9: The total cross section ($\gamma + \gamma$ plus $\gamma + Z$ plus $\gamma + h$) as a function of the energy of the photon and for several values of the coupling g_{DM}. The black squares are the Fermi LAT data points (Ackermann et al. 2013).

the limits should increase by an order of magnitude or so and allow for further examination of the TPDM model parameter space.

Chapter 4

Concluding Remarks

It has been known for a long time that some kind of matter that does not interact electromagnetically exists and it is very abundant in the Universe. This new kind of matter was dubbed "dark matter" (DM) for obvious reasons but initially not many people followed this direction and decided to ignore it. However, after some other experimentalists with better instruments and methods, and almost forty years of difference, showed that the initial lead was correct, other people started to pay attention to it.

At first the explanations were given in terms of known particles (some of them undetected at the time). In the standard model there was a particularly attractive particle to associate with DM, the neutrino. It was known the neutrino was neutral, that it interacted weakly and gravitationally only and it was thought to be massless. For some time it was the leading candidate but after some advancements in the theoretical calculations (convenience model or ΛCDM) and the cosmological observational methods (standard Hot Big-Bang and structure formation) it started to look less promising. The main problem is that a particle that is massless or that carries little mass has to be a "hot" particle (moves fast), and the formation of the structures, according to simulations, required the new particle to be "cold" (that moves very slowly or its kinetic energy is small compared to its mass).

After the disenchantment with the neutrino other options started to look promising, in particular two related with more general theories developed to cure some of the "shortcomings" of the Standard Model (SM). The first option was associated to the solution of the CP-problem in the strong interaction sector. The new field was thought to be some sort of scalar that was <u>not</u> a thermal relic and therefore could be very light or very heavy, i.e., there were no real restrictions on the mass coming from thermodynamics at the early stages of the Universe. The second alternative to extend the SM is called supersymmetry (SUSY) and associates to each SM particle a superpartner with $spin_{SUSY} = spin_{SM} - 1/2$. The new particles have the same set of interactions as the SM particles, therefore there are plenty of options to choose a particle that is neutral and it interacts weakly (note that due to SUSY not being an exact symmetry all the particles are assumed to be massive).

The SUSY approach is a specific case where a model of new physics predicts a WIMP (weakly-interacting massive particle). WIMPs are new particles that are very massive. In this case the idea is that the new particle is very massive (more massive than anything in the second generation of the SM) and interacts weakly (SM weak interaction) or through a weak-like interaction but without the restrictions imposed by the SM and SUSY.

After decades of effort none of these alternatives have been confirmed experimentally. Remember that there are three ways to detect DM: directly, DM material scatters off SM particles in a detector (usually some inert element in liquid form at low temperatures and then detecting the radiation produced by the SM particle recoiling); indirectly, looking at the sky for signals (mainly from annihilation of DM particles) that are not easily attributable to known processes in astrophysics (larger than expected flux of anti-particles, very high-energy photons with sharp drops and/or spectral lines at values that point to interactions with new particles, neutrinos scattered off or produced by DM with very high-energy - excess over the expected value from astrophysics calculations); and finally there are collider searches in which DM is created when SM particles collide and annihilate producing detectable signals but with large missing energy/transverse momentum (one problem here is that without knowing the mass of the new particle and the strength of the interaction it is difficult to decide in which particular region should the research be centered and full scans of the parameter space are required).

Although some experimental collaborations have claimed a new signal and provided the explanation in terms of DM (e.g., direct detection: DAMA, COGENT; indirect detection: AMS-2, Fermi Telescope), the most recent and accurate experiments show no evidence of these signals or signals consistent with the properties of DM derived from those other experiments (XENON, LUX). On the collider front, the most celebrated observation has been the detection of a Higgs boson at the LHC but the searches had been going on for very wide range of models and the parameter space reduction for SUSY and extra-dimensions is starting to make people to move to more exotic models (due to the lack of a DM signal)).

In this work some alternatives were studied, following the trend to look for the location of new astronomical sources of signals from DM or to move to more exotic models. In this approach, once the model has been chosen and an interaction was determined to be a good candidate for generating a promising signal, the initial state particles are determined. Afterwards the possible places where these particles co-exist are determined from theoretical/observational studies. But one

way to improve the chances of detection is to augment the number of particles available, i.e., looking for places where the density of DM and SM particles is higher than average. Additionally if the particles involved in the interaction are very energetic the probability of confusing this signal with regular signals diminishes. One such place in the Universe is the core (nucleus) of a galaxy (AGN) in which the activity is larger than expected. In this work, the signal from this type of interaction was computed and compared to experimental data. The predictions exhibit a sharp cutoff in the flux of gamma-rays, the position of which depends on the difference in mass between the two new particles. While comparing with the data a reasonable fit was obtained.

Additionally this model has a DM candidate that is a thermal relic therefore the calculation of the density as of today for the given model is required. This imposes a restriction to the model and there are some tensions between the best fit variables and the "preferred" value of the variables. In particular the difference in masses points to a case in which DM has more than one component and the candidate from the model is not the main component (more than 70%) but close to slightly less than half of the total DM. Finally, in the near future some of the direct detection experiments can constrain or discard the model given that the cross-section is about one order of magnitude smaller than the last published limit for the cross section by an experimental collaboration.

The second model studied was more exotic and included two new particles. A fermionic DM candidate and a new heavier scalar colored (but weak singlet)"mediator" both couple to the right-handed top quark (the singlet part of the top quark) in a (postulated) new interaction (If this sound familiar is because it is very similar to SUSY searches but unlike SUSY there are no more particles in the model and there is a new coupling constant). This choice is not capricious but based on the possibility of an enhancement of the signal due to near degeneracy between DM candidate and the top quark additionally the small difference among the masses points to some relation to the EW symmetry breaking. But a price has to be paid, in this case the direct detection signal is suppressed due to the null top parton distribution function inside a nucleon, i.e., if an interaction occurs it must be higher order (suppressed) interaction.

This leaves two alternatives: indirect detection and collider searches, both of them were studied in this work. The first step was to apply the relic density restriction, this reduces the number of degrees of freedom from three to two. Then for reasonable choices of the parameters a simulation of the production process in a proton collider was ran and some cuts were found for optimizing the signal above the background (unfortunately there are no general formulas for all possible values of

the parameters). Clearly the most important characteristic is the missing energy/momentum and the first cut $\not{E}_T > 100\,\text{GeV}$ eliminates a good portion of the background signal. Because it is possible to b-tag the events, variables related to the hadronic and leptonic decay are useful to improve the signal. For the hadronic side $|M_{bjj} - m_t| < 20\,\text{GeV}$ a b-tag part and two additional jets are required while for the leptonic side $M_T\left(b\ell, \not{E}_T\right) > 200\,\text{GeV}$. Finally the azimuthal separation ($\Delta\varphi$) can be useful if the right conditions hold, i.e., if the width decay is small enough $\Gamma_\phi \sim 3\,\text{GeV}$.

Another alternative was implemented too, a multi-variate analysis based on the kinematical variables for the process. A discriminant $\mathcal{D}$, which is function of the set of observables $\mathcal{O} = \big\{\not{E}_T, M_T(b\ell, \not{E}_T),$
$\Delta\varphi_{\not{E}_T}, M_T(\phi_h), M_T(\phi_\ell)\big\}$ is optimized and there is no need to impose hard cuts in the variables sequentially. However, for simplicity the analysis was done based on subsets of $\mathcal{O}$ and ignoring the correlation among the variables. The final contour plot in the plane $m_\phi - m_\chi$ was constructed (the contour are not smooth due to the vast amount of points needed).

For the indirect detection part the flux of high-energy gamma-rays and lines from DM annihilation was computed. It was shown that the signal could be detected with current equipment but that if an increase of about one of order of magnitude is achieved the signal becomes clearer and two out of three lines can be resolved. This kind of signal is very difficult to explain with astrophysical processes only giving a good signal of the nature of DM.

A final comment about the "new searches" is in order. Although it is possible to choose any model in this work the decision was made based in the likelihood of the model being correct and the possibility to detect a signal over a relatively short period of time in the future (~ 5 years). This two points are of incredible relevance to phenomenological studies due to the fact that they go hand-in-hand with experiments. If both conditions are violated, the studies may be interesting but not too relevant for the detection of DM.

Appendix A

Quantum Field Theory

In this appendix, an outline of quantum field theory or QFT is given. QFTs are the basic framework with which high-energy theorists construct their theories. Usually two principles are introduced as the basis of QFT but in general additional ideas are required to constrain the theory to an acceptable level of applicability. Following Duncan (Duncan 2012) three principles are sufficient for the purpose:

- Quantum Mechanics (QM): of special importance is the superposition principle (linearity of amplitudes) and unitarity.
- Special Relativity: invariance under homogeneous Lorentz transformations.
- Clustering: the results of local events are independent of events far away.

Note that the last requirement is related to causality and unitarity but is not the same.

A.1 Quantum Mechanics

The distinctive characteristic of QM is its randomness contained in the uncertainty principle. Any theory that does not contain the uncertainty principle is considered a classical theory. There are two main approaches to QM: one based on operators and the Heisenberg's equation (canonical formalism) and another one based on a variational principle (path integral formalism). The former is the oldest and most studied out of the two (initially it was thought that all physical systems might be solved perturbatively) and the later one is more "modern" and allows to study non-perturbative situations (Zee 2010).

A.1.1 Canonical Formalism

Depending how the time evolution is assigned to the states, the operators or both, there are different ways to express quantities in QM (called pictures). The approach used in advanced QM is called interaction picture in which the dynamics (as given by the hamiltonian) is split in a analytically solvable part and a "small" perturbation. The time dependence due to the solvable part is assigned to the operators and the time evolution of the states is contained in the perturbation. Define $H_S = H_{0,S} + H_{1,S}$[1] where the S means Schoedinger's picture, the relationship between Schroedinger's picture and the interaction picture is given by (Duncan 2012):

$$\begin{aligned} |\psi_I(t)\rangle &= e^{iH_{0,S}t}|\psi_S(t)\rangle \\ A_I(t) &= e^{iH_{0,S}t} A_S(t)\, e^{-iH_{0,S}t}. \end{aligned} \tag{A.1}$$

[1] Note that this splitting is not unique but can be done in a way that facilitates the calculations.

Applying the operator equation to the hamiltonian gives:

$$\begin{aligned} H_{0,I}(t) &= e^{iH_{0,S}t} H_{0,S} e^{-iH_{0,S}t} = H_{0,S} \\ H_{1,I}(t) &= e^{iH_{0,S}t} H_{1,S}(t)\, e^{-iH_{0,S}t} \end{aligned} \tag{A.2}$$

where it was assumed that the solvable part of the hamiltonian is time independent and the perturbation has become time dependent in the interaction picture. The solution of the Heisenberg's equation for the time evolution operator is

$$U(t,t_0) = e^{iH_0 t} e^{-iH(t-t_0)} e^{-iH_0 t_0} \tag{A.3}$$

and the evolution of the state is given by:

$$|\alpha;t\rangle_I = U(t,t_0)\,|\alpha;t_0\rangle_I. \tag{A.4}$$

Evidently the operator U depends on both parts of the hamiltonian, but remember that only the solution to H_0 is known therefore to find the full operator an implicit solution or iterative approximation is required:

$$\begin{aligned} U(t,t_0) &= \sum_{n=0}^{\infty} (-i)^n \int_{t_0}^{t} dt_1 \int_{t_0}^{t_1} dt_2 \int_{t_0}^{t_2} dt_3 \cdots \int_{t_0}^{t_{n-1}} dt_n \prod_{j=1}^{n} H_I(t_j) \\ U(t,t_0) &= \sum_{n=0}^{\infty} \frac{(-i)^n}{n!} \int_{t_0}^{t} \cdots \int_{t_0}^{t} dt_1 \cdots dt_n T\left[\prod_{j=1}^{n} H_I(t_j)\right] \end{aligned} \tag{A.5}$$

where T is the time ordering operator which arranges the operators in order of occurrence. Finally a symmetry would preserve the inner product of two states (in any picture):

$$|\langle\Psi|\Phi\rangle|^2 = |\langle\Psi|U^\dagger U|\Phi\rangle|^2 = |\langle\Psi'|\Phi'\rangle|^2. \tag{A.6}$$

Inner products lead to probabilities and expectation values to observables.

A.1.2 Path Integral Formalism

In the second approach a "sum over all possibilities" is used to make the calculations[2]. Defining the kernel for a single particle:

$$K_E\left(q_f, t_f; q_i, t_i\right) = \langle q_f | e^{-H(t_f - t_i)} | q_i \rangle \tag{A.7}$$

subdividing the interval $T = t_f - t_i$ into N subintervals $t_n = t_i + n\tau$ with $\tau = T/N$ the kernel becomes:

$$K_E\left(q_f, t_f; q_i, t_i\right) = \int \prod_{n=1}^{N-1} dq_n \langle q_f | e^{-H\tau} | q_{N-1} \rangle \langle q_{N-1} | e^{-H\tau} | q_{N-2} \rangle \cdots \langle q_2 | e^{-H\tau} | q_1 \rangle \langle q_1 | e^{-H\tau} | q_i \rangle. \tag{A.8}$$

The calculation for the free particle or the simple harmonic oscillator SHO points to the functional integral of the exponential of the action (in euclidean space) $exp\left(S_E\right)$ which generalizes to:

$$K\left(q_f, t_f; q_i, t_i\right) = \int \mathcal{D}p\mathcal{D}q e^{i\int_{t_i}^{t_f} L dt} = \int \mathcal{D}p\mathcal{D}q e^{i\int_{t_i}^{t_f} \left(p(t)\dot{q}(t) - H(p(t), q(t))\right) dt} \tag{A.9}$$

which is the amplitude for a transition from state q_i at time t_i to state q_f at time t_f (Zee 2010). Note that in general it is not possible to find a closed form for the integral.

A.1.3 Special Relativity

The equivalence principle (the laws of physics are invariant -same form- for all inertial observers) and the constancy of the speed of light are enough to find the transformation between reference frames moving at constant speed with respect to each other. These transformations are called Lorentz transformations and are linear homogeneous change of coordinates that preserve the interval $(\Delta s)^2 = (\Delta s')^2$:

$$x^{\mu\prime} = \Lambda^{\mu}_{\nu} x^{\nu} \iff x^{\mu} = \left(\Lambda^{\mu}_{\nu}\right)^{-1} x^{\nu\prime} \tag{A.10}$$

[2]The path integral formal is was developed by Richard Feynman and initially was received with suspicion by other physicists and made mathematicians to grind their teeth.

where the elements of the matrix Λ and its inverse are related by reversing the sign of the speed (Srednicki 2007). For instance assuming that the motion is in the $z-$axis:

$$\Lambda = \begin{pmatrix} \gamma & 0 & 0 & -\gamma\beta \\ 0 & 1 & 0 & 0 \\ 0 & 0 & 1 & 0 \\ -\gamma\beta & 0 & 0 & \gamma \end{pmatrix} \rightarrow \Lambda^{-1} = \begin{pmatrix} \gamma & 0 & 0 & \gamma\beta \\ 0 & 1 & 0 & 0 \\ 0 & 0 & 1 & 0 \\ \gamma\beta & 0 & 0 & \gamma \end{pmatrix}. \tag{A.11}$$

Equation A.10 defines a contravariant vector in spacetime and similar, but not exactly the same, transformations for other objects (covariant vectors, second rank tensors...). This transformation rule applies to four-momentum (momentum for short from now on) too with the temporal component being the energy (Thompson 2013):

$$p^{\mu} = \begin{pmatrix} E \\ \vec{p} \end{pmatrix} \tag{A.12}$$

‘ and satisfies the on-mass shell relation:

$$E^2 = |\vec{p}|^2 + m^2 \tag{A.13}$$

that finally gives the invariant interval for momentum $p^{\mu}p_{\mu} = m^2$.

Note that the results of the previous subsection are not Lorentz invariant and therefore different observers will postulate different laws of nature, the next subsection will address this problem.

A.2 Relativistic Quantum Mechanics

Going back to wave functions the first try to generalize Schroedinger's equation is the Klein-Gordon equation:

$$\left(\partial^2 + m^2\right)\varphi = 0 \tag{A.14}$$

which looks very promising until the energy is calculated and two options appear, one positive and one negative (first problem); the second problem is that the possibility of negative probabilities. For this two reasons and the fact that it does not include spin effects it was discarded (Srednicki 2007; Griffiths 1987; Thompson 2013).

The next attempt was a fully relativistic electron equation the Dirac equation:

$$\left(i\gamma^{\mu}\partial_{\mu} - m\right)\psi = \left(i\partial\!\!\!/ - m\right)\psi = 0 \tag{A.15}$$

where ψ is a four dimensional object called spinor that allows for spin-1/2 particles, but the negative energy appears again. After a while Dirac interpreted the unwanted solutions as an antiparticle (a new particle with the same mass but opposite additive quantum number, e.g., electric charge) and almost everything fitted again, the number of components was exactly as needed, the probability interpretation was more or less restore. However some problems remained, the number of particles was not conserved and the zero point energy kept diverging. The no conservation of number of particles points clearly to a field interpretation of the theory and not longer for a single particle one (Duncan 2012; Zee 2010).

A.2.1 QFT (finally)

Putting all together and starting with, in analogy with classical field theory, the lagrangian for a free spin-0 field is:

$$\mathcal{L}_0 = \frac{1}{2}\left(\partial_{\mu}\varphi\partial^{\mu}\varphi - m^2\varphi^2\right) \tag{A.16}$$

which gives the path integral with a source J:

$$Z_0\left[J\right] = \langle 0|0\rangle_J = \int \mathcal{D}\varphi\, e^{i\int d^4x\left[\frac{1}{2}\left(\partial_{\mu}\varphi\partial^{\mu}\varphi - m^2\varphi^2\right)+J\varphi\right]} = \int \mathcal{D}\varphi\, e^{i\int d^4x} e^{\left[-\frac{1}{2}\varphi\left(\partial^2+m^2\right)\varphi+J\varphi\right]}. \tag{A.17}$$

The inverse of a differential operator and its Green's function are related by $\left(\partial^2 + m^2\right)\Delta\left(x-y\right) = -\delta^4\left(x-y\right)$ which allows to evaluate the gaussian integral:

$$Z_0\left[J\right] = Z\left[0\right] e^{-(i/2)\int d^4x\, d^4y\, J(x)\Delta(x-y)J(y)} = Z\left[0\right] e^{iW[J]}. \tag{A.18}$$

The Green's function for the Klein-Gordon equation is (including the $i\epsilon$ prescription to avoid the pole) is:

$$\Delta\left(x-y\right) = \int \frac{d^4k}{\left(2\pi\right)^4}\frac{e^{ik(x-y)}}{k^2 - m^2 + i\epsilon} \tag{A.19}$$

and is going to be of great importance afterwards because it represents the propagation of a particle from x to y (or vice-versa depending on the sign of the time component of the four-vectors). Including

an interaction term in the lagrangian $\mathcal{L} = \mathcal{L}_0 + \mathcal{L}_1 + J\varphi$ the path integral is (and working in analogy with basic gaussian integrals):

$$Z_1[J] = \int \mathcal{D}\varphi\, e^{i\int d^4x(\mathcal{L}_0+\mathcal{L}_1+J\varphi)} = e^{i\int d^4x\mathcal{L}_1\left(\frac{1}{i}\frac{\delta}{\delta J(x)}\right)} \int \mathcal{D}\varphi\, e^{i\int d^4x(\mathcal{L}_0+J\varphi)} \propto e^{i\int d^4x\mathcal{L}_1\left(\frac{1}{i}\frac{\delta}{\delta J(x)}\right)} Z_0[J]. \tag{A.20}$$

The missing constant of proportionality is used to enforced $Z_1[0] = 1$. Expanding the exponentials:

$$Z_1[J] \propto \sum_{V=0}^{\infty} \frac{1}{V!}\left(i\int d^4x\mathcal{L}_1\left(\frac{1}{i}\frac{\delta}{\delta J(x)}\right)\right)^V \sum_{P=0}^{\infty}\frac{1}{P!}\left(-\frac{i}{2}\int d^4x\, d^4y\, J(x)\,\Delta(x-y)\,J(y)\right)^P \rightarrow$$
$$Z_1[J] \propto \sum_{V=0}^{\infty} \frac{1}{V!}\left(i\int d^4x\mathcal{L}_1\left(\frac{1}{i}\frac{\delta}{\delta J(x)}\right)\right)^V \sum_{P=0}^{\infty}\frac{1}{P!}\left(i\,W[J]\right)^P \tag{A.21}$$

here lies the foundation for Feynman diagrams (after applying the functional derivatives) the numbers V and P stand for number of vertices and number of propagators in the diagram (additionally there exist a relationship between these numbers and the number of external legs but this depends on the interaction lagrangian $\mathcal{L}_1$) (Zee 2010; Srednicki 2007).

Working on the full propagator (denoted by bold font):

$$\frac{1}{i}\mathbf{\Delta}(x_1 - x_2) = \langle 0|T\varphi(x_1)\,\varphi(x_2)|0\rangle \tag{A.22}$$

to get the two φ's factors two functional derivatives are necessary, denoting the functional derivatives by $i\delta_j = \delta/\delta(x_j)$:

$$\langle 0|T\varphi(x_1)\,\varphi(x_2)|0\rangle = \delta_1\delta_2 Z_0[J]\big|_{J=0} = \delta_1\delta_2\left(i\,W[J]\right)\big|_{J=0} - \delta_1\left(i\,W[J]\right)\big|_{J=0}\delta_2\left(i\,W[J]\right)\big|_{J=0} \rightarrow$$
$$\langle 0|T\varphi(x_1)\,\varphi(x_2)|0\rangle = \delta_1\delta_2\left(i\,W[J]\right)\big|_{J=0} \tag{A.23}$$

the second term in the second equality can be drop because only connected diagrams contribute to the sum:

$$\langle 0|T\varphi(x_1)\,\varphi(x_2)|0\rangle \rightarrow \langle 0|T\varphi(x_1)\,\varphi(x_2)|0\rangle_C. \tag{A.24}$$

Without interactions particles cannot do anything but move freely, the next step is to introduce an interaction term one of the simplest is φ^4. With this interaction the lowest order term is:

$$\begin{aligned} 1,2 \to 3,4 \propto \left(-\frac{i\lambda}{4!}\right) \int d^4w \int \mathcal{D}\varphi\, e^{(i/2)\int d^4\left[(\partial\varphi)^2 - m^2\varphi^2\right]} \varphi(x_1)\,\varphi(x_2)\,\varphi(x_3)\,\varphi(x_4)\,\varphi(w)^4 = \\ -i\lambda \int d^4w\, \Delta(x_1 - w)\,\Delta(x_2 - w)\,\Delta(x_3 - w)\,\Delta(x_4 - w) \end{aligned} \tag{A.25}$$

two particles start at x_1 and x_2 converge to w scatter with strength $-i\lambda$ and then propagate to x_3 and x_4. Going to momentum space which is easier to associated with observations:

$$1,2 \to 3,4 \propto -i\lambda\,(2\pi)^4\,\delta^{(4)}\,(k_1 + k_2 - k_3 - k_4) \prod_{j=1}^{4} \frac{1}{k_j^2 - m^2 + i\epsilon} \tag{A.26}$$

where the product of propagators indicate the external particles and will be dropped because it is common to all processes with of the type $2 \to 2$ particles (amputate the legs) and the Dirac's delta function assures the conservation of momentum and can be dropped too (with the corresponding $(2\pi)^4$). What is left is known as scattering amplitude (to leading order) (Zee 2010):

$$i\mathcal{M} = -i\lambda \to \mathcal{M} = -\lambda. \tag{A.27}$$

Because almost we know about the subatomic world comes from scattering experiments and it is tedious to repeat with procedure every time it is useful to define a shortcut, called Feynman rules, for the calculation of the scattering amplitude[3].

A.2.2 Feynman Rules

The Feynman rules for scalar φ^4 field theory in momentum space are:

1. Label each external line with a momentum p and each internal line with a momentum q.
2. For each vertex include a factor of $-i\lambda$ and $(2\pi)^4\,\delta^4\,(p_{in} - p_{out})$ where *in* and *out* make reference to the specific vertex.
3. For each internal line include a propagator $i/\left(q^2 - m^2 + i\epsilon\right)$ and for each external line a factor of 1.

[3]Note that some changes will be required for different kind of particles in more general theories but the principles applied are the same.

4. Integrate each internal momentum with measure $d^4q/(2\pi)^4$. This is equivalent to summation over intermediate states in basic perturbation theory.
5. Include a symmetry factor associated with the diagram.
6. Drop the last factor of conservation of momentum $(2\pi)^4 \delta^4 (\sum p_{in} - \sum p_{out})$ where *in* and *out* make reference to initial and final particles.

A.3 Gauge Theories

When the lagrangian has a symmetry (a transformation is applied and the new lagrangian is the "same" as the initial one) a family of parameters can be associated with the transformation. When the parametrization is independent of space-time variables the symmetry is global, and when the parametrization is a function of the space-time variables the symmetry is local. The latter case is the interesting one because it is possible to show that the interactions in QFT are related to this type of symmetries (Duncan 2012; Zee 2010; Guidry 1991; Thompson 2013). The prototypical interaction is quantum electrodynamics (QED), which was discovered first and studied extensively, and it serves as an example of the procedure known as "gauging the symmetry" in the following subsection.

A.3.1 Quantum Electrodynamics

The lagrangian for a free electron is given by:

$$\mathcal{L}_0 = \bar{\psi} \left(i\partial\!\!\!/ - m \right) \psi \tag{A.28}$$

and is invariant under the (global) transformation $\psi \to e^{i\theta}\psi$ as can be checked by substitution. When the phase depends on the coordinates $\theta = \theta(x)$ a new term appears, due to the derivative, and the only way to make the lagrangian invariant again is to substitute the derivative by the "covariant" derivative:

$$\partial^\mu \to \partial^\mu + iqA^\mu = D^\mu \tag{A.29}$$

generating the new lagrangian:

$$\mathcal{L} = \bar{\psi} \left(i\partial\!\!\!/ - qA\!\!\!/ - m \right) \psi \tag{A.30}$$

note the interaction term in the new lagrangian $\mathcal{L} = \mathcal{L}_0 + \mathcal{L}_{int}$. This new lagrangian is invariant under the simultaneous transformations:

$$\psi \to e^{i\theta(x)}\psi \qquad \text{and} \qquad A_\mu \to A_\mu - \frac{1}{q}\partial_\mu\theta(x). \tag{A.31}$$

The procedure can be summarized in two considerations:

1. Imposing a local phase invariance on the fermion field demands the introduction of a new massless vector field A^μ.
2. The local phase invariance has dynamical content, i.e., it specifies the nature of the interaction between the fermion field and the vector field.

The same procedure followed in the last section can be used to derive the Feynman rules for QED. However, it is possible to read the rules from the interaction term in the lagrangian (Griffiths 1987; Thompson 2013):

1. Label each external line with a momentum p and each internal line with a momentum q.
2. For each vertex include a factor of $-ig_e\gamma^\mu$ with $g_e = \sqrt{4\pi\alpha}$, and a factor of $(2\pi)^4 \delta^4 (p_{in} - p_{out})$ where *in* and *out* make reference to the specific vertex.[4]
3. For each internal fermionic line include a propagator $i(\not{q}+m)/(q^2-m^2)$ and for each internal massless vector line include the propagator $-ig_{\mu\nu}/q^2$. For an incoming (outgoing) external fermionic particle associate the spinor u ($\bar{u}$), for an incoming (outgoing) external fermionic antiparticle associate the spinor $\bar{v}$ (v) and for an incoming (outgoing) external vector boson associate the polarization four-vector ϵ^μ ($\epsilon^{\mu *}$).
4. Integrate each internal momentum with measure $d^4q/(2\pi)^4$. This is equivalent to summation over intermediate states in basic perturbation theory.
5. Include a symmetry factor associated with the diagram.
6. Drop the last factor of conservation of momentum $(2\pi)^4 \delta^4 (\sum p_{in} - \sum p_{out})$ where *in* and *out* make reference to initial and final particles.

A.4 The Standard Model

The SM includes one simple group $SU(3)_c$ and one semi-simple group $SU(2)_L \times U(1)_Y$, each part represents a different interaction (Guidry 1991; Burgess and Moore 2006). The former is for quantum chromodynamics and the latter is for electroweak theory. After some struggle with the

[4]Note that α in here represents the fine structure constant.

renormalization of QED, gauge theories started to look more promising and they were applied to the other known phenomena: weak and strong nuclear forces. Both of them were very different from QED and their properties required more general groups and concepts. In the following subsections an overview of those properties and concepts is done.

A.4.1 Quantum Chromodynamics

By the mid-fifties a plethora of hadrons were known and in 1961 Gell-Man and Ne'eman developed the eightfold way to accommodate them in groups of similar properties and masses. Then in 1963 Gell-Mann and Zweig proposed the existence of quarks, a new type of particle of which hadrons are composed. From experimental data it was known that quarks should have an additional quantum number to avoid the violation of the exclusion principle.

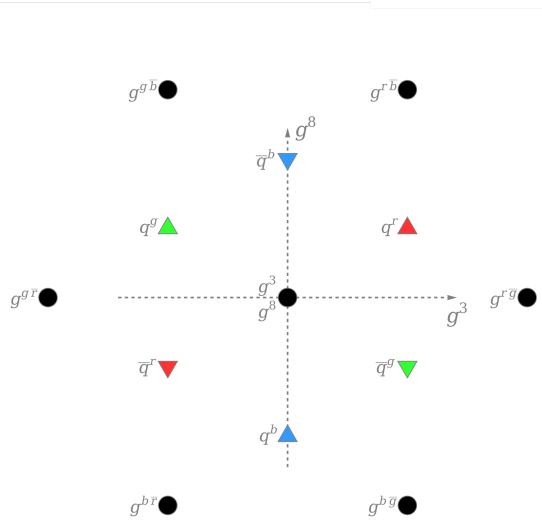

Figure A.1: QCD particle content. The triangular arrangement comes from color (optics)theory.[5]

Some differences between QED and QCD exist. First QCD is non-abelian, while QED is abelian. This means that gluons (the mediator of the interaction) can couple to other gluons in cubic and quartic vertices. Second the strength of the interaction decreases with energy in QCD and increases for QED. To accommodate these observations and other empirically known facts the require group is $SU(3)_c$ and the content needed is shown in Figure A.1.

The corresponding lagrangian is:

$$\mathcal{L}_{QCD} = \bar{\psi}\gamma^{\mu}\left(i\partial_{\mu} - \frac{g_s}{2}\lambda^a G^a_{\mu}\right)\psi - \frac{1}{4}G^a_{\mu\nu}G^{a\mu\nu} \quad \text{with}$$
$$G^a_{\mu\nu} = \partial_{\mu}G^a_{\nu} - \partial_{\nu}G^a_{\mu} - g_s f_{abc}G^b_{\mu}G^c_{\nu} \tag{A.32}$$

where the masses of the quarks are not included because they belong to the Higgs part of the lagrangian. The terms proportional to derivatives of the field $\partial_{\mu}G^a_{\nu}$ generate terms proportional to the four-momentum.

Only the second Feynman rule should be modified to include the new vertices:

- quark-quark-gluon. The factor is $\left(^{-ig_s}/_2\right)\lambda^a\gamma^{\mu}$.
- gluon-cubic. The factor is $-g_s f^{abc}\Big[g_{\mu\nu}\left(q_1-q_2\right)_{\lambda} + g_{\nu\lambda}\left(q_2-q_3\right)_{\mu} + g_{\mu\lambda}\left(q_3-q_1\right)_{\nu}\Big]$.
- gluon-quartic. The factor is:

$$-ig_s\left[f^{abe}f^{cde}\left(g_{\mu\lambda}g_{\nu\rho} - g_{\mu\rho}g_{\lambda\nu}\right) + f^{ade}f^{cbe}\left(g_{\mu\nu}g_{\lambda\rho} - g_{\mu\lambda}g_{\nu\rho}\right) + f^{ace}f^{dbe}\left(g_{\mu\rho}g_{\lambda\nu} - g_{\mu\nu}g_{\lambda\rho}\right)\right].$$

Note that for low energy the perturbative approach is invalid and another one is required. The new approach is lattice gauge theory in which a lattice in space-time is created to include the hadron in question and calculations are made with a technique called Wilson loops which are plaquettes on the lattice (Zee 2010; Duncan 2012; Guidry 1991).

A.4.2 Electroweak Theory

The EW theory is the unification of electromagnetic and weak interactions. First two groups are assumed to exist $SU(2)_L$ (three bosons W^{μ}_i) and $U(1)_Y$ (one boson B^{μ}). The lagrangian is given by:

$$\mathcal{L}_{EW} = \sum_{j\in\{L,\,R\}}\bar{\psi}_j\gamma^{\mu}\left(i\partial_{\mu} - \frac{g}{2}I_{\psi_j}\vec{\tau}\cdot\vec{W}_{\mu} - \frac{g'}{2}Y_{\psi_j}B_{\mu}\right)\psi_j - \frac{1}{4}W^a_{\mu\nu}W^{a\mu\nu} - \frac{1}{4}B_{\mu\nu}B^{\mu\nu} + \mathcal{L}_{higgs} + \mathcal{L}_{Yukawa} \tag{A.33}$$

where the Higgs part gives masses to the vector bosons and the Yukawa part includes the masses of the fermions. And the definition of the tensors in terms of the fields are (Guidry 1991):

$$W^a_{\mu\nu} = \partial_{\mu}W^a_{\nu} - \partial_{\nu}W^a_{\mu} - g\,\epsilon_{abc}W^b_{\mu}W^c_{\nu}$$
$$B_{\mu\nu} = \partial_{\mu}B_{\nu} - \partial_{\nu}B_{\mu}. \tag{A.34}$$

[5]Figure by Cjean42/CC BY 3 (URL: `http://en.wikipedia.org/wiki/File:QCD.svg`)

To obtain massive vectors instead of massless bosons like with the simple gauging of the theory a new mechanism was needed and one of the first persons to publish about it was Peter Higgs, hence the Higgs mechanism.

A.4.2.1 The Higgs Mechanism

The introduction of the Higgs mechanism allows three vector bosons to become massive while the fourth remains massless (the photon, of course). The Higgs lagrangian including the simplest potential that can give mass to the vector bosons is:

$$\mathcal{L}_{higgs} = \left| \left(\partial_\mu - \frac{i\,g}{2} \vec{\tau} \cdot \vec{W}_\mu + \frac{i\,g'}{2} B_\mu \right) \phi \right|^2 - \frac{\lambda}{4} \left(\phi^\dagger \phi - v^2 \right)^2 . \tag{A.35}$$

When the electrically neutral component of the doublet acquires a non-zero vacuum expectation value (making the second term on the left hand-side to vanish) the symmetry breaks and a mass term appears. Diagonalization of the states produces the observed spectrum (Thompson 2013):

$$\begin{pmatrix} W_\mu^+ \\ W_\mu^- \\ Z_\mu \\ A_\mu \end{pmatrix} = \begin{pmatrix} 1 & 0 & 0 & 0 \\ 0 & 1 & 0 & 0 \\ 0 & 0 & \cos\theta_W & -\sin\theta_W \\ 0 & 0 & \sin\theta_W & \cos\theta_W \end{pmatrix} \begin{pmatrix} W_\mu^1 \\ W_\mu^2 \\ W_\mu^3 \\ B_\mu \end{pmatrix} \tag{A.36}$$

which shows that the photon and the neutral vector boson Z are linear combinations of the hypercharge and the weak neutral vector boson W^3. The masses are $m_W = {}^{gv}/_2$, $m_A = 0$ and $m_Z = ({}^{v}/_2)\sqrt{g^2 + g'^2}$.

The Yukawa term gives masses to the fermions through the couplings to the Higgs:

$$\mathcal{L}_{Yukawa} = -\sum_{m,n=0}^{3} \left(\Gamma^u_{m\,n} \bar{q}^0_{m\,L} \tilde{\phi}\, u^0_{n\,R} + \Gamma^d_{m\,n} \bar{q}^0_{m\,L} \phi\, d^0_{n\,R} + \Gamma^e_{m\,n} \bar{\ell}^0_{m\,n} \phi\, e^0_{n\,R} \right) + h.c.. \tag{A.37}$$

these numbers are not known a priori and are determined experimentally.

Appendix B

Gamma-ray Signals from AGN, Calculations

B.1 Scattering between DM and SM Particles with Radiation in Final State

As is evident from Figure 2.3 on page 30 and Figure B.1, the dominant contributions to the cross section and, thus, the gamma-ray flux come from the s-channel Feynman diagrams due to resonances when the intermediate E goes on-shell. Thus, it appears a safe assumption would be to neglect the u-channel diagrams shown in Figure 2.2 on page 27 since there is no chance for the intermediate E in these diagrams to go on-shell.

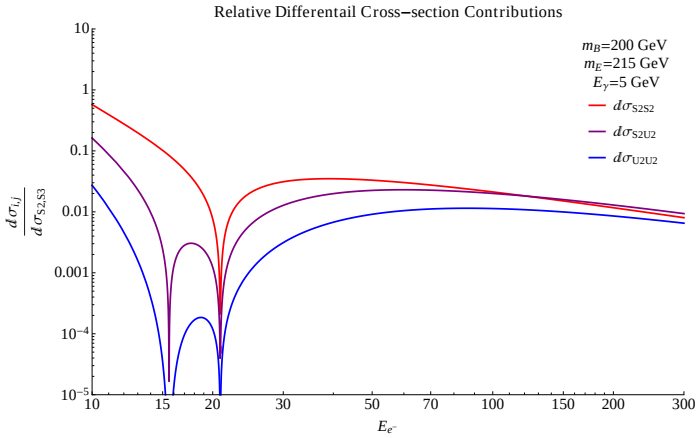

Figure B.1: Relative contribution to the differential cross-section from a representative sample of the combination of Feynman diagrams. Even when mixed with one of the resonant channels the u-channel contribution is negligible.

Besides the resonant-enhancement from the E going on-shell, there is another source of enhancement in the process considered here: a logarithmic enhancement when the photon is collinear with the final-state electron (note that, since the angle of observation does not line up with the jet axis, there is no possibility of the photon being collinear with the *initial-state* electron). Below, we outline the calculation assuming that the resonant and collinear regime makes up the most important contribution to the cross section. This calculation and this appendix follow closely Appendix B of (Gorchtein et al. 2010) (by design) and provides an important check on our calculation using the full set of Feynman diagrams and the exact kinematics of the process.

The pieces of the amplitude-squared that have the collinear log enhancement are:

$$\frac{1}{2}\sum_{\lambda,spins}|\mathcal{M}_2|^2=\frac{1}{2}e^2g_1^4(Y_L^2+Y_R^2)^2\frac{E_2E_5}{t_{45}\left|D_1\right|^2}\left[1+\frac{(Y_L^2-Y_R^2)^2}{(Y_L^2+Y_R^2)^2}\cos\theta\right],$$

$$\frac{1}{2}\sum_{\lambda,spins}2\left|\mathcal{M}_{S_2}\mathcal{M}_{S_3}^*\right|=-e^2g_1^4(Y_L^2+Y_R^2)^2\frac{\Re\left(D_2\right)E_2E_4(E_4+E_5)}{t_{45}\left|D_1\right|^2\left|D_2\right|^2}\times\left[1+\frac{(Y_L^2-Y_R^2)^2}{(Y_L^2+Y_R^2)^2}\cos\theta\right],$$

$$\frac{1}{2}\sum_{\lambda,spins}2\left|\mathcal{M}_{S_1}\mathcal{M}_{S_2}^*\right|=-2e^2g_1^4(Y_L^2+Y_R^2)^2\frac{\Re\left(D_1\right)\Re\left(D_2\right)E_2^2E_4(E_4+E_5)}{t_{25}t_{45}\left|D_1\right|^2\left|D_2\right|^2}$$

$$\times\left[1-\frac{4(Y_L^2-Y_R^2)^2}{(Y_L^2+Y_R^2)^2}\cos\theta-\frac{(Y_L^2-Y_R^2)^2}{(Y_L^2+Y_R^2)^2}\cos^2\theta\right], \tag{B.1}$$

where $D_1=E_2-\delta+i\,\Gamma/2$ and $D_2=E_2-E_5-\delta+i\,\Gamma/2$ while the pieces of the amplitude-squared that do not have collinear log enhancements are:

$$\frac{1}{2}\sum_{\lambda,spins}|\mathcal{M}_1|^2=-e^2g_1^4(Y_L^4+Y_R^4)\frac{E_4E_5}{t_{25}\left|D_2\right|^2}$$

$$\frac{1}{2}\sum_{\lambda,spins}|\mathcal{M}_3|^2=-\frac{1}{4}e^2g_1^4(Y_L^2+Y_R^2)^2\frac{E_2E_4}{\left|D_1\right|^2\left|D_2\right|^2} \tag{B.2}$$

$$\frac{1}{2}\sum_{\lambda,spins}2\left|\mathcal{M}_{S_1}\mathcal{M}_{S_3}^*\right|=e^2g_1^4(Y_L^2+Y_R^2)^2\frac{E_2E_4\Re\left(D_1\right)\left(E_5-E_2\right)}{t_{25}t_{45}\left|D_1\right|^2\left|D_2\right|^2}\left[1+\frac{(Y_L^2-Y_R^2)^2}{(Y_L^2+Y_R^2)^2}\cos\theta\right].$$

We group the pieces of the amplitude-squared that contain the collinear logarithm ($|\langle\mathcal{M}\rangle|^2_{log}$) and those that do not ($|\mathcal{M}|^2_{no\,log}$) as:

$$|\mathcal{M}|^2_{log} = \frac{1}{2}\left[\left|\mathcal{M}_{S_2}\right|^2+2Re|\mathcal{M}_{S_2}\mathcal{M}_{S_3}^*|+2Re|\mathcal{M}_{S_1}\mathcal{M}_{S_2}^*|\right], \tag{B.3}$$

$$|\mathcal{M}|^2_{no\,log} = \frac{1}{2}\left[\left|\mathcal{M}_{S_1}\right|^2+\left|\mathcal{M}_{S_3}\right|^2+2Re|\mathcal{M}_{S_1}\mathcal{M}_{S_3}^*|\right], \tag{B.4}$$

and compute the cross section as:

$$\frac{d^2\sigma}{dE_5d\Omega_5}=\frac{1}{(2\pi)^5}\frac{1}{32M_B^2E_2}\left[|\mathcal{M}|^2_{log}t_{45}\int d\Omega_4\frac{E_5E_4}{t_{45}}+4\pi|\mathcal{M}|^2_{no\,log}\right]$$
$$=\frac{\pi}{(2\pi)^5}\frac{1}{32M_B^2E_2}\left[|\mathcal{M}|^2_{log}t_{45}\ln\left(\frac{4E_4^2}{m_e^2}\right)+4|\mathcal{M}|^2_{no\,log}\right].$$

B.2 Gamma-ray Lines from DM Annihilation

In the calculation of the loop amplitudes, the following algorithm was used. First, we reduce all dot products of the form $k \cdot p$ (where k is the loop momentum and p is a generic external momentum) against the corresponding factors from propagators in the denominator. The resulting three-point functions can be safely computed using the standard Passarino-Veltman (PV) technique (Passarino and Veltman 1979). The remaining terms in the amplitudes take the form of four-point scalar (D_0) and rank-two tensor ($D_{\mu\nu}$) functions:

$$D_{0;\mu\nu}(p_1, p_2, p_3; m_1, m_2, m_3, m_4) = \int \frac{d^n k}{i\pi^2} \frac{\{1; k_\mu k_\nu\}}{[k^2 - m_1^2][(k+p_1)^2 - m_2^2][(k+p_1+p_2)^2 - m_3^2][(k+p_1+p_2+p_3)^2 - m_4^2]}, \quad \text{(B.5)}$$

where p_i are external momenta and m_i are the masses of the particles circling the loops. Note that we have neglected rank-one tensor integrals (D_μ) since we are only interested in extracting the $g_{\mu\nu}$ pieces of the amplitude.

Following the PV scheme, the rank-two tensor integral can be rewritten as a linear expansion in tensor structures which are built from the external momenta and the metric tensor:

$$D_{\mu\nu} = D_{21} p_{1,\mu} p_{2,\nu} + D_{22} p_{2,\mu} p_{2,\nu} + \cdots + D_{27} g_{\mu\nu}, . \quad \text{(B.6)}$$

The coefficients of this expansion (D_{ij}) can then be reduced to scalar integrals (Passarino and Veltman 1979). However, in cases where two of the external momenta become identical, as for the case of WIMP annihilation, this approach breaks down. In these cases, the expressions for the D_{ij} coefficients in terms of scalar integrals depend inversely on the Gram Determinant (GD) built from the external momenta (i.e., GD = $det(p_i \cdot p_j)$). In certain kinematical regions (e.g., where two of the momenta become degenerate and GD $\simeq 0$), the PV scheme gives rise to spurious divergences. In calculations for collider processes (where the momenta are integrated over an entire phase space), this situation arises only at *special* points near the boundaries of phase space. Special techniques involving interpolating from these *unsafe* regions of phase space to *safe* regions have been developed to deal with these spurious divergences in calculations for collider processes.

These techniques do not apply to our situation (where the two incoming momenta are fixed *and* identical) and we are forced to approach this problem using the following method. For our

calculation, we have chosen to implement the technique developed in Ref. (Stuart 1988). In this algebraic reduction scheme, the original PV scheme is extended to deal with situations where the GD *exactly* vanishes. Higher-point tensor (and scalar) integrals are expressed in terms of lower-point quantities which can be safely evaluated utilizing the usual numerical techniques. For example, the expressions for the four-point scalar integral (D_0) and the tensor coefficient (D_{27}) can be expressed as:

$$\begin{aligned} D_0 &= \alpha_{123} C_0(123) + \alpha_{124} C_0(124) \\ &+ \alpha_{134} C_0(134) + \alpha_{234} C_0(234)\,, \end{aligned} \tag{B.7}$$

and:

$$\begin{aligned} D_{27} &= \alpha_{123} C_{24}(123) + \alpha_{124} C_{24}(124) \\ &+ \alpha_{134} C_{24}(134) + \alpha_{234} C_{24}(234)\,, \end{aligned} \tag{B.8}$$

where $C_0(ijk)$ and $C_{24}(ijk)$ are the three-point scalar integral and PV tensor coefficient, respectively (the (ijk) denotes various propagator factors in the original four-point denominator). The α_{ijk} coefficients can be obtained by solving the matrix equation:

$$\begin{pmatrix} 1 & 1 & 1 & 1 \\ 0 & p_1^2 & (p_1^2 - p_2^2 + p_5^2)/2 & (p_1^2 + p_4^2 - p_6^2)/2 \\ 0 & (-p_1^2 - p_2^2 + p_5^2)/2 & (-p_1^2 + p_2^2 + p_5^2)/2 & (-p_1^2 - p_3^2 + p_5^2 + p_6^2)/2 \\ -m_1^2 & p_1^2 - m_2^2 & p_5^2 - m_3^2 & p_4^2 - m_4^2 \end{pmatrix} \begin{pmatrix} \alpha_{234} \\ \alpha_{134} \\ \alpha_{124} \\ \alpha_{123} \end{pmatrix} = \begin{pmatrix} 0 \\ 0 \\ 0 \\ 1 \end{pmatrix} \tag{B.9}$$

where $p_1, \ldots, p_4$ are the external momenta, $p_5 = p_1 + p_2$, $p_6 = p_2 + p_3$ and the m_i are loop particle masses.

This approach allows us to construct quite compact expressions for the one-loop amplitudes for the processes of interest in terms of kinematical factors and scalar integrals of the form $B_0(p^2; m_1^2, m_2^2)$ and $C_0(p_1^2, p_2^2, p_5^2; m_1^2, m_2^2, m_3^2)$.

Appendix C

Bayesian fit using Markov Chain Monte Carlo

In this work a Markov Chain Monte Carlo (MCMC) was used to fit the available data. The MCMC approach is based on Bayesian methods to scan over specified input parameters given constraints on an output set. Using Bayes' theorem, the posterior probability density function (PDF) of the model parameters, θ, given the data, d, and model, M, is given by:

$$p(\theta|d, M) = \frac{\pi(\theta|M)p(d|\theta, M)}{p(d|M)}, \tag{C.1}$$

where $\pi(\theta|M)$ is the prior on the model parameters, the $p(d|\theta, M)$ term is the likelihood and the term $p(d|M)$ term is called the evidence, but is often ignored as the PDFs are properly normalized to unity.

The advantage of a MCMC approach is that in the limit of large chain length the distribution of points (under appropriate circumstances), θ_i, approaches the posterior distribution of the modeling parameters given the constraining data. In addition, the set formed by a function of the points in the chain, $f(\theta_i)$, corresponds to the posterior distribution of that function of the parameters given the data.

The Goodman-Weare (GW) algorithm (Goodman and Weare 2010) was used, which has been shown to be very efficient and fast. A collection of initially random points referred to as "walkers" at time t, $\{\theta_i(t)\}$, are placed in parameter space. A given walker's next trial position, $\theta_i(t)'$, is based chosen along a line connecting it to another randomly chosen walker, θ_j, with the trial:

$$\theta_i(t) \rightarrow \theta_i' = \theta_j + Z\left(\theta_i(t) - \theta_j\right), \tag{C.2}$$

where Z is a random variable with the distribution

$$g(z) \propto \frac{1}{\sqrt{z}} \tag{C.3}$$

in the interval $[1/a, a]$ and vanishes elsewhere. The trial point is accepted if

$$q \equiv z^{N-1}\frac{\mathcal{L}_{t+1}}{\mathcal{L}_t} > r, \tag{C.4}$$

where r is a uniform random variate and $\mathcal{L}_i = e^{-\sum_j \chi^2_{i,j}/2} = e^{-\sum_j (y_{i,j}-d_i)^2/2\sigma_j}$ is the likelihood function. This selection ensures detailed balance within the algorithm, which is necessary for the algorithm

to be statistically relevant. The parameter a sets the scale of jumps. The value $a = 2$ is often used as it yields a very efficient exploration of the parameter space.

A "burn-in" period is allowed to prevent correlation of the walker's initial random state to the set of walkers used for the posterior distribution. The autocorrelation time is given by:

$$C_i(T) = \frac{1}{n-T} \sum_{t=1}^{n-T} (\theta_i(t) - \bar{\theta}_i)(\theta_i(t+T) - \bar{\theta}_i) \tag{C.5}$$

for each input parameter and it is verify that the burn-in length is at least 5 times the auto-correlation scale.

Appendix D

Relic Density

One of the most important constraints on DM (assuming it is a thermal relic) is the relic density. As shown in Chapter 3 on page 40 this restriction allows to decrease the number of degrees of freedom by one for all models. But what constitutes a thermal relic? Basically, a species that was in thermal equilibrium before freezing out and leaving a relic density. And the temperature at which freeze-out occurs usually is low making the particles non-relativistic. However, the experimental error is so small ($< 1\%$) that even for mildly relativistic particles ($\beta \sim 0.3$) the traditional approach introduces "large" errors ($\sim 5\%$). In this appendix the algorithm for the calculation of the relic density is explained (Gondolo and Gelmini 1991).

D.1 The Boltzmann Equation

Define $f = f(\vec{x}, \vec{p}, t)$, then the Boltzmann Equation is given by:

$$\hat{L}[f] = \hat{C}[f] \tag{D.1}$$

with the Liouville operator given by (Gondolo and Gelmini 1991; Profumo 2013):

$$\begin{aligned} \hat{L}_{NR} &= \frac{d}{dt} + \frac{d\vec{x}}{dt}\nabla_x + \frac{d\vec{v}}{dt}\nabla_v \qquad \text{or} \\ \hat{L}_{cov} &= p^\mu \frac{\partial}{\partial x^\mu} - \Gamma^\mu_{\alpha\beta} p^\alpha p^\beta \frac{\partial}{\partial p^\mu}, \end{aligned} \tag{D.2}$$

but for a homogeneous and isotropic cosmology (Robertson-Walker metric) f cannot depend on $\vec{x}$ or $\hat{p}$, i.e., f depends on $|\vec{p}|$ or E and t. With these simplifications the Liouville operator simplifies to:

$$\hat{L}[f] = E\frac{\partial f}{\partial t} - H\frac{|\vec{p}|^2}{E}\frac{\partial f}{\partial E} \tag{D.3}$$

with $H = \dot{a}/a$ the Hubble parameter.

The particle number density is the integral over all momenta and summed over all spins:

$$n = \int f(E,t)\frac{g\, d^3\vec{p}}{(2\pi)^3} \tag{D.4}$$

applying this procedure to the Boltzmann equation for the process $1+2 \rightarrow 3+4$, and particle 1 only, gives:

$$\begin{aligned} \frac{dn_1}{dt} + 3Hn_1 &= -\left\langle \sigma\beta_{M\not{o}l} \right\rangle_{therm.} \left(n_1 n_2 - n_1^{eq.} n_2^{eq.}\right) \qquad \text{where} \\ \left\langle \sigma\beta_{M\not{o}l} \right\rangle_{therm.} &= \frac{\int \sigma\beta_{M\not{o}l} dn_1^{eq.} dn_2^{eq.}}{\int dn_1^{eq.} dn_2^{eq.}} \end{aligned} \tag{D.5}$$

from now on the subscript *therm.* indicating that it is a thermal average will be dropped. A completely analogous equation exist for particle 2 switching n_1 and n_2. When the initial particles are a particle-antiparticle pair the relevant quantity is $n = n_1 + n_2$ but when the chemical potential is negligible $n = 2n_1$ and the resulting Boltzmann equation is:

$$\frac{dn}{dt} + 3Hn = -\left\langle \sigma\beta_{M\not{o}l} \right\rangle \left(n^2 - n_{eq.}^2\right) \tag{D.6}$$

and additional factor of one half is included for non-identical particles (Gondolo and Gelmini 1991).

Remembering that the total entropy per co-moving volume is a constant ($sa^3 = const.$) the replacement $Y = {}^{n}/_{s}$ simplifies the equation to (Gondolo and Gelmini 1991; Profumo 2013; Kolb and M. 1994):

$$\frac{dY}{dt} = -s\left\langle \sigma\beta_{M\not{o}l} \right\rangle \left(Y^2 - Y_{eq.}^2\right) \tag{D.7}$$

which can be transform to a function of the photon temperature $x = {}^{m_\chi}/_{T}$:

$$\frac{dY}{dx} = \frac{1}{3H}\frac{ds}{dx}\left\langle \sigma\beta_{M\not{o}l} \right\rangle \left(Y^2 - Y_{eq.}^2\right). \tag{D.8}$$

Replacing the temperature dependence of the Hubble parameter and the entropy in the equation gives:

$$\frac{dY}{dx} = -\sqrt{\frac{\pi g_*}{45G}}\frac{m_\chi}{x^2}\left\langle \sigma\beta_{M\not{o}l} \right\rangle \left(Y^2 - Y_{eq.}^2\right). \tag{D.9}$$

Once the thermal average is found the differential equation can be solved.

D.1.1 Thermal Average

Assuming that the equilibrium distribution as function of the temperature T is Maxwell-Boltzmann in the co-moving frame:

$$\left\langle \sigma\beta_{M\not{o}l} \right\rangle = \frac{\int \sigma\beta_{M\not{o}l} e^{-E_1/T} e^{-E_2/T} d^3\vec{p}_1 d^3\vec{p}_2}{\int e^{-E_1/T} e^{-E_1/T} d^3\vec{p}_1 d^3\vec{p}_2} \tag{D.10}$$

changing integration variables to $E_+ = E_1 + E_2$, $E_- = E_1 - E_2$ and $s = 2m_\chi + 2E_1E_2 - 2\,|\vec{p}_1|\,|\vec{p}_2|\cos\theta$ gives (Gondolo and Gelmini 1991; Profumo 2013; Drees et al. 2009):

$$\langle \sigma\beta_{M\phi l}\rangle = \frac{1}{8m_\chi^4 T\left(K_2\left({}^{m_\chi}/_T\right)\right)^2}\int_{4m_\chi^2}^{\infty}\sigma(s-4m_\chi^2)\sqrt{s}\,K_1\left({}^{\sqrt{s}}/_T\right)ds \tag{D.11}$$

where K_i are modified Bessel functions of order i. Clearly the thermal average is a function of the temperature T and it is necessary to compute this integral for each value of T that is used in the numerical solution of D.9 (a very time consuming procedure). For this reason the non-relativistic approximation is very popular and then a program like micrOMEGAs (Belanger et al. 2014a) is used to compute the fully relativistic solution.

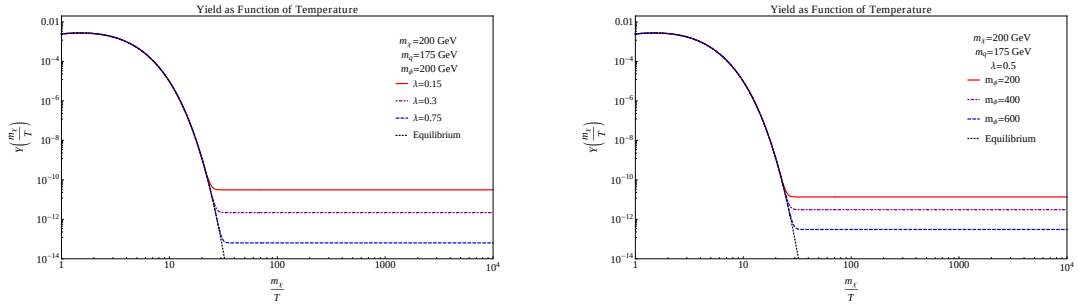

(a) Yield as function of temperature for degenerate masses and different coupling constants.

(b) Yield as function of temperature for $\lambda = 0.5$ and different values of m_ϕ.

Figure D.1: Yield as function of temperature $x = {}^{m_\chi}/_T$.

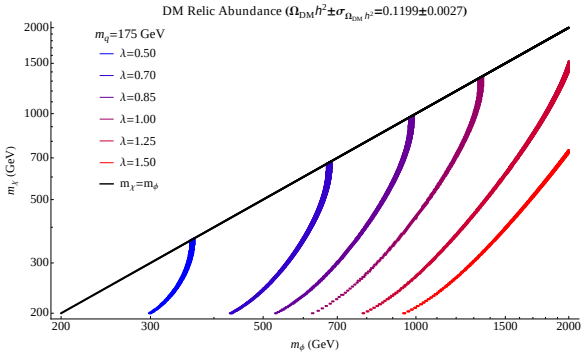

Figure D.2: Bands of phase space that are consistent wit the observed relic abundance for several values of the coupling $\lambda = g_{DM}$.

In the non-relativistic approximation the quantity $\sigma\beta_{M\o l}$ is expanded in a series of the speed. And given that the definition of the Møller factor is $\beta_{M\o l} = \sqrt{|\vec{v}_1 - \vec{v}_2|^2 - |\vec{v}_1 \times \vec{v}_2|^2}$ which has its simplest form in the "lab" reference frame (one of the particles is at rest) and the average is equal for the co-moving reference frame and the "lab" reference frame, the approximation is made in the "lab" frame. Due to this equality the approximation $\sigma\beta_{lab} \approx a + b\beta_{lab}^2$ is used for calculating the thermal average (Drees et al. 2009; Gondolo and Gelmini 1991; Profumo 2013):

$$\langle \sigma\beta_{lab} \rangle \approx a + \frac{6bT}{m_\chi} = a + \frac{6b}{x} \tag{D.12}$$

and then this function of temperature is plugged into Boltzmann differential equation[1].

The only problem is that the equation is stiff and requires some care to solve. First the freeze-out temperature is found by assuming that the solution behaves like in equilibrium before the critical temperature $x < x_F$ and then the equilibrium function can be neglected completely and finally both solutions are connected together. The solution for fixed value of the masses and different couplings constants is shown in Figure D.1a on the previous page while the solution for fixed coupling different masses of the mediator is shown in Figure D.1b on the preceding page. To finally get the relic abundance using Equation (3.10) on page 45 as shown in Figure D.2 on the preceding page. Note that the main difference between this plot and the one generate from micrOMEGAs (Belanger et al. 2014a) is in the long tails close to degenerate masses due to coannihilation processes that come into play when the temperature is close to the mass of the mediator particle $^{m_\phi}/_T \approx 1$ which is important only when $m_\phi \approx m_\chi$.

[1]There are three exceptions in which the approximation fails: coannihilation, annihilation into heavier but almost degenerate (in mass) particles and near a pole of the cross-section (Griest and Seckel 1991).

Appendix E

DM Chiral Top Portal: Loop Corrections

In this appendix the calculation of the correction to the top quark mass (Yukawa coupling) at one loop for the TPDM is shown. The lagrangian for the model is

$$\mathcal{L} = \mathcal{L}_{SM} + i\bar{\chi}\partial\!\!\!/\chi - m_\chi\bar{\chi}\chi + (D_\mu\varphi)^\dagger (D^\mu\varphi) - m_\varphi^2\varphi^*\varphi + g_{DM}\varphi^*\bar{\chi}P_R t + g_{DM}\varphi\bar{t}P_L\chi \tag{E.1}$$

where the covariant derivative is $D_\mu = \partial_\mu - ig_s G_\mu^a T^a - iQ_t eA_\mu$ with $Q_t = 2/3$ is the electric charge of the top quark in units of e.

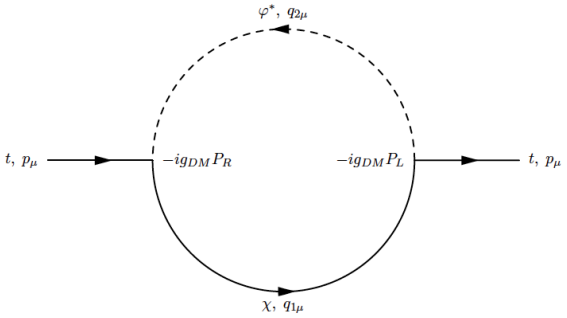

Figure E.1: $t \to \varphi^*\chi \to t$.

The matrix element for the subprocess shown in Figure E.1 (the modification to the top quark propagator due to the new particles and interactions) is

$$i\mathcal{M} = \frac{g_{DM}^2}{(2\pi)^4}\int \frac{\bar{u}_2 P_L\left(q\!\!\!/_1 + m_\chi\right)P_R u_1 d^4q_1}{\left(q_1^2 - m_\chi^2\right)\left[(q_1-p)^2 - m_\varphi^2\right]} = \frac{g_{DM}^2}{(2\pi)^4}\bar{u}_2\int \frac{q\!\!\!/_1 d^4q_1}{\left(q_1^2 - m_\chi^2\right)\left[(q_1-p)^2 - m_\varphi^2\right]}P_R u_1 \to$$

$$i\mathcal{M} = \bar{u}_2 I\left(p\!\!\!/\right)P_R u_1 \tag{E.2}$$

where the integral I can be re-expressed as a double integral

$$I\left(p\!\!\!/\right) = g_{DM}^2\int_0^1\int \frac{N\left(q\!\!\!/, x, p\!\!\!/\right)}{\left(q^2+D\right)^2}\frac{d^4q}{(2\pi)^4}dx \tag{E.3}$$

where $q = q_1 - (1-x)\,p$, $N\left(\not{q}, x, \not{p}\right) = \not{q} + (1-x)\,\not{p}$ and $D = x\,(1-x)\,p^2 - x m_\chi^2 - (1-x)\,m_\varphi^2$. Transforming to a full euclidean space and doing a analytical continuation for the number of dimensions $d = 4 - \epsilon$

$$I\left(\not{p}\right) = -g_{DM}^2 \int_0^1 \frac{\Gamma\left(\epsilon/2\right)}{\left(4\pi\right)^{2-\epsilon/2}} \frac{(1-x)\,\not{p}}{D^{\epsilon/2}} dx \tag{E.4}$$

in the limit of small ϵ

$$\begin{aligned} I\left(\not{p}\right) &\approx -\frac{g_{DM}^2}{16\pi^2} \int_0^1 \left(\frac{2}{\epsilon} - \gamma_E\right) \left(1 + \frac{\epsilon}{2} \ln\left(\frac{4\pi\tilde{\mu}}{D}\right)\right) (1-x)\,\not{p} dx \rightarrow \\ I\left(\not{p}\right) &\approx -\frac{g_{DM}^2 \not{p}}{16\pi^2} \left[\frac{1}{\epsilon} - \int_0^1 (1-x) \ln\left(\frac{D}{\mu}\right) dx\right] \\ &= A\left(p^2\right) \not{p} + B\left(p^2\right) m_t^2 \end{aligned} \tag{E.5}$$

which means that there is no correction to the mass but there is a correction to the wave function. It is reassuring that the model does not disturb the mass of the top quark given that the measurement of the width is very precise.

Appendix F

Light DM

By the end of the first decade of the 21st century some efforts were made to understand the nature of DM dropping one of the assumptions made in most DM models, the collisionless DM assumption. Some calculations point to some tension between the existing models and their consequences for structure formation against the (statistical) analysis of observed structure formation. The general idea was to include more general interactions into the simulations that come from interacting DM (Tulin et al. 2013c,b; McDermott et al. 2012; Tulin et al. 2013a). Data from cosmic relic were in tension with some announced hints of DM detection and the proposal of a new force acting in the dark sector only (Arkani-Hamed et al. 2009). The model included a heavy DM candidate that is a thermal relic and a new intermediary particle very light (in the sub- GeV range). This last property, a "long" range interaction, allows the existence of the phenomenon known as Sommerfeld enhancement. The effect can be detected through astronomical observations (indirect detection) given an additional reason to study this type of interaction.

The structure of the study was to identify potential interactions more singular than Coulomb/Yukawa's potential near the origin and that had a non-trivial angular dependence but semi-analytically tractable such as the inclusion in the simulations was not a killer. Because the potential is highly singular near the origin a cutoff was introduced in the model and then a study of the "renormalizability" was made. By summer of 2012 this approach was not longer attractive and the study was stopped. In the following sections the steps made are shown up to the stopping point.

F.1 Singular Potentials

The fully relativistic interaction is taken into account, i.e., the matrix element is calculated, then the non-relativistic limit is taken and it is identify as the Fourier transform of the potential (Beane et al. 2001). The conventions and approximations for the calculations are stated in the first subsection of this section.

F.1.1 Preliminaries

For definiteness a basis for the gamma matrices is chosen and the limits at low speed are made.

F.1.1.1 Gamma matrices

The gamma matrices can be represented in different basis (each useful for a specific calculation). However the most important thing is to be consistent and use always the same representation, in this case the Dirac representation:

$$\gamma^0 = \begin{pmatrix} 0 & I \\ I & 0 \end{pmatrix}, \qquad \gamma^j = \begin{pmatrix} 0 & \sigma_j \\ -\sigma_j & 0 \end{pmatrix} \qquad \text{and} \qquad \gamma^5 = \begin{pmatrix} -I & 0 \\ 0 & I \end{pmatrix}. \tag{F.1}$$

F.1.2 Spinors

In the non-relativistic limit the spinors simplified to:

$$u(p,s) = \begin{pmatrix} \sqrt{p^\mu \sigma_\mu}\xi^s \\ \sqrt{p^\mu \overline{\sigma}_\mu}\xi^s \end{pmatrix} \approx \sqrt{m_\chi} \begin{pmatrix} \xi^s \\ \xi^s \end{pmatrix} \tag{F.2}$$

where ξ^s is a two dimensional array depending on the spin of the particle and orthogonal among each other for different values of spin ${\xi^{s_1}}^\dagger \xi^{s_2} = \delta^{s2}_{s1}$.

F.1.2.1 Gamma matrices and spinors

The following combinations of gamma matrices and spinors will appear more than once in the next section, therefore making the calculations here will save some time afterwards.

1. Two spinors and a gamma matrix.

$$\bar{u}_l \gamma^\mu u_n = u_l^\dagger \gamma^0 \gamma^\mu u_n = \begin{cases} u_l^\dagger u_n = 2m_\chi \xi_l^\dagger \xi_n = 2m_\chi \delta^{s_l}_{s_n} & \text{if } \mu = 0, \\ m_\chi \begin{pmatrix} \xi_l^\dagger & \xi_l^\dagger \end{pmatrix} \begin{pmatrix} -\sigma_j & 0 \\ 0 & \sigma_j \end{pmatrix} \begin{pmatrix} \xi_n \\ \xi_n \end{pmatrix} = 0 & \text{if } \mu \in \{1,2,3\}. \end{cases} \tag{F.3}$$

2. Two spinors and a contracted gamma matrix with the transferred momentum.

$$\bar{u}_l \not{q} u_n \approx -m_\chi \begin{pmatrix} \xi_l^\dagger & \xi_l^\dagger \end{pmatrix} \gamma^0 \begin{pmatrix} 0 & -\vec{\sigma}\cdot\vec{q} \\ \vec{\sigma}\cdot\vec{q} & 0 \end{pmatrix} \begin{pmatrix} \xi_n \\ \xi_n \end{pmatrix} = 0. \tag{F.4}$$

Note that this is the same as the former case with the energy component set to 0.

3. Two spinors, one gamma matrix and one gamma-five matrix.

$$\bar{u}_l \gamma^\mu \gamma_5 u_n \approx m_\chi \begin{pmatrix} \xi_l^\dagger & \xi_l^\dagger \end{pmatrix} \gamma^\mu \begin{pmatrix} -\xi_n \\ \xi_n \end{pmatrix} = \begin{cases} 0 & \text{if } \mu = 0, \\ 2\, m_\chi \xi_l^\dagger \xi_n \sigma_j = 2\, m_\chi \delta_{s_n}^{s_l} \sigma_j & \text{if } \mu \in \{1,2,3\}. \end{cases} \tag{F.5}$$

4. Two spinors, one contracted gamma matrix with the transferred momentum and a gamma-five matrix.

$$\begin{aligned} \bar{u}_l \not{q} \gamma_5 u_n &\approx m_\chi \begin{pmatrix} \xi_l^\dagger & \xi_l^\dagger \end{pmatrix} \begin{pmatrix} 0 & I \\ I & 0 \end{pmatrix} \begin{pmatrix} 0 & -\vec{\sigma}\cdot\vec{q} \\ \vec{\sigma}\cdot\vec{q} & 0 \end{pmatrix} \begin{pmatrix} -I & 0 \\ 0 & I \end{pmatrix} \begin{pmatrix} \xi_n \\ \xi_n \end{pmatrix} \\ &= -m_\chi \begin{pmatrix} \xi_l^\dagger & \xi_l^\dagger \end{pmatrix} \begin{pmatrix} \vec{\sigma}\cdot\vec{q} & 0 \\ 0 & \vec{\sigma}\cdot\vec{q} \end{pmatrix} \begin{pmatrix} \xi_n \\ \xi_n \end{pmatrix} \rightarrow \end{aligned} \tag{F.6}$$

$$\bar{u}_l \not{q} \gamma_5 u_n \approx -2 m_\chi \delta_{s_n}^{s_l} \vec{\sigma}\cdot\vec{q} \rightarrow \bar{u}_l \not{q} \gamma_5 u_n \approx -2 m_\chi \delta_{s_n}^{s_l} \vec{s}_n \cdot \vec{q}.$$

F.1.3 Potentials

In which follows the non-relativistic limit potential for different interactions is found. The master equation for this section is (Beane et al. 2001):

$$V(\vec{r}) = \frac{1}{(2\pi)^3} \int V(\vec{q})\, e^{i\,\vec{q}\cdot\vec{r}} d^3\vec{q} \quad \text{and} \quad \langle p_{final} | i\,T | p_{initial} \rangle = -i\,V(\vec{q})\,(2\pi)\,\delta\left(E_{\vec{p}_{final}} - E_{\vec{p}_{initial}}\right). \tag{F.7}$$

F.1.3.1 Scalar DM and Massive Vector Mediator

The interaction lagrangian is $\mathcal{L}_{int} \propto \phi\, B^\mu \partial_\mu \phi$. The model $t-$channel interaction is shown in Figure F.1 and because in the non-relativistic case the particles can always be identified making this diagram the relevant one.

Conservation of four-momenta and momentum transfer are given by:

$$p_1^\mu + p_2^\mu = p_3^\mu + p_4^\mu \rightarrow q^\mu = p_3^\mu - p_1^\mu = p_2^\mu - p_4^\mu \tag{F.8}$$

with these definitions the matrix element for the process is:

$$i\,\mathcal{M} = i\,g^2 q^\mu \frac{g_{\mu\nu} - \frac{q_\mu q_\nu}{m_V^2}}{q^2 - m_V^2} (-q^\nu) = -i\,g^2 \frac{q^2 - \frac{q^4}{m_V^2}}{q^2 - m_V^2} = i\frac{g^2 q^2}{m_V^2} \approx -i\frac{g^2\,|\vec{q}|^2}{m_V^2} \tag{F.9}$$

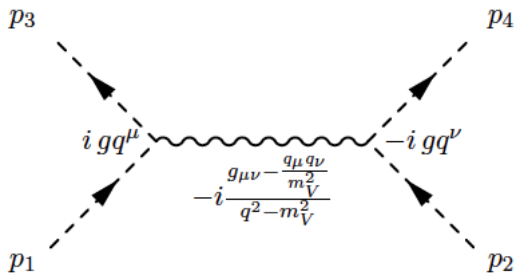

Figure F.1: $\phi\phi \to V \to \phi\phi$.

The potential in momentum space is:

$$V(\vec{q}) = \frac{g^2\,|\vec{q}|^2}{m_V^2}. \tag{F.10}$$

Evidently the potential is highly divergent at the origin (second derivative of a delta function), i.e. it is a contact interaction, but no angular dependence.

F.1.3.2 Spinor DM and Massive Vector and Axial Vector Mediator

The interaction lagrangian is $\mathcal{L}_{int} \propto \bar{\chi}\,\gamma^{\mu}\left(a + b\gamma^5\right) B_{\mu}\chi$. The model $t-$channel interaction is shown in Figure F.2 and because in the non-relativistic case the particles can always be identified and only this diagram is necessary.

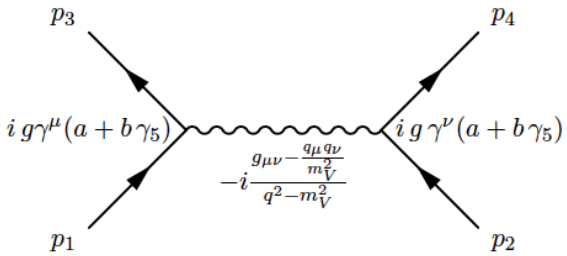

Figure F.2: $\chi\chi \to V \to \chi\chi$.

Conservation of four-momenta and momentum transfer are given by:

$$p_1^{\mu} + p_2^{\mu} = p_3^{\mu} + p_4^{\mu} \to q^{\mu} = p_3^{\mu} - p_1^{\mu} = p_2^{\mu} - p_4^{\mu} \tag{F.11}$$

and the matrix of vector and axial coefficients is:

$$A = a + b\,\gamma_5 = \begin{pmatrix} a-b & 0 \\ 0 & a+b \end{pmatrix} \tag{F.12}$$

with these definitions the matrix element for the process is:

$$\begin{aligned} i\,\mathcal{M} &= i\frac{g^2}{q^2 - m_V^2}\left(\bar{u}_4\gamma^\mu A\,u_2\,\bar{u}_3\gamma_\mu A\,u_1 - \frac{\bar{u}_4 \not{q} A\,u_2\,\bar{u}_3 \not{q} A\,u_1}{m_V^2}\right) \rightarrow \\ i\,\mathcal{M} &\approx i\frac{4m_\chi^2 g^2}{\left|\vec{q}\right|^2 + m_V^2}\left[\frac{b^2(\vec{\sigma}_1\cdot\vec{q})(\vec{\sigma}_2\cdot\vec{q})}{m_V^2} - a^2 + b^2\left(\vec{\sigma}_1\cdot\vec{\sigma}_2\right)\right]\delta_{s_1}^{s_3}\delta_{s_2}^{s_4}. \end{aligned} \tag{F.13}$$

The potential in momentum space is[1]:

$$V\left(\vec{q}\right) = -\frac{g^2}{\left|\vec{q}\right|^2 + m_V^2}\left[\frac{b^2(\vec{s}_1\cdot\vec{q})(\vec{s}_2\cdot\vec{q})}{m_V^2} - a^2 + b^2\left(\vec{s}_1\cdot\vec{s}_2\right)\right]\delta_{s_1}^{s_3}\delta_{s_2}^{s_4} \tag{F.14}$$

which implies that the potential in coordinate space is:

$$\begin{aligned} V\left(\vec{r}\right) &= -\frac{1}{(2\pi)^3}\int\frac{g^2}{\left|\vec{q}\right|^2 + m_V^2}\left[\frac{b^2(\vec{s}_1\cdot\vec{q})(\vec{s}_2\cdot\vec{q})}{m_V^2} - a^2 + b^2\left(\vec{s}_1\cdot\vec{s}_2\right)\right]e^{i\vec{q}\cdot\vec{r}}d^3\vec{q}\,\delta_{s_1}^{s_3}\delta_{s_2}^{s_4} \rightarrow \\ V\left(\vec{r}\right) &= -\left[\frac{b^2(-i\vec{s}_1\cdot\vec{\nabla})(-i\vec{s}_2\cdot\vec{\nabla})}{m_V^2} - a^2 + b^2\left(\vec{s}_1\cdot\vec{s}_2\right)\right]\frac{1}{(2\pi)^3}\int\frac{g^2}{\left|\vec{q}\right|^2 + m_V^2}e^{i\,\vec{q}\cdot\vec{r}}d^3\vec{q}\,\delta_{s_1}^{s_3}\delta_{s_2}^{s_4}. \end{aligned} \tag{F.15}$$

Remembering that Fourier transforms form pairs and that the Fourier transform of the Yukawa potential is:

$$\begin{aligned} F\left(\vec{q}\right) &= \int\frac{e^{-mr}}{4\pi r}e^{-i\,\vec{q}\cdot\vec{r}}d^3\vec{r} = \frac{1}{2}\int_0^\infty r\,e^{-mr}\int_0^\pi e^{-i\,q\,r\cos\theta}\sin\theta d\theta\,dr = \int_0^\infty r\,e^{-mr}\left[\frac{\sin\left(q\,r\right)}{q\,r}\right]dr \rightarrow \\ V\left(\vec{q}\right) &= \frac{1}{q}\left\{-\frac{e^{-mr}\left[q\cos\left(q\,r\right) + m\sin\left(q\,r\right)\right]}{q^2 + m^2}\right\}\Bigg|_0^\infty = \frac{1}{q}\frac{q}{q^2 + m^2} = \frac{1}{q^2 + m^2} \end{aligned} \tag{F.16}$$

then the potential in coordinate space is (ignoring the Kronecker's deltas for spin variables from now on):

$$\begin{aligned} V\left(\vec{r}\right) &= -\frac{g^2}{4\pi}\left[\frac{-b^2(\vec{s}_1\cdot\vec{\nabla})(\vec{s}_2\cdot\vec{\nabla})}{m_V^2} - a^2 + b^2\left(\vec{s}_1\cdot\vec{s}_2\right)\right]\frac{e^{-m_V r}}{r} \rightarrow \\ V\left(\vec{r}\right) &= -\frac{g^2}{4\pi}\left(\frac{-b^2 s_{1j}s_{2k}\partial_j\partial_k}{m_V^2} - a^2 + b^2 s_{1j}s_{2j}\right)\frac{e^{-m_V r}}{r}. \end{aligned} \tag{F.17}$$

[1]Note that the interaction conserves spin on each vertex.

The derivatives of the Yukawa function can be reduced to tensor form:

$$\partial_j\partial_k\frac{e^{-mr}}{r} = -\partial_j\left(\frac{m\,e^{-mr}x_j}{r^2}+\frac{e^{-mr}x_j}{r^3}\right) = \frac{m^2e^{-mr}x_jx_k}{r^3}+\frac{3m\,e^{-mr}x_jx_k}{r^4}+\frac{3m\,e^{-mr}x_jx_k}{r^5}$$

$$-\frac{m\,e^{-mr}\delta_j^k}{r^2}-\frac{e^{-mr}\delta_j^k}{r^3} = \left[\left(m^2+\frac{3m}{r}+\frac{3}{r^2}\right)\frac{x_jx_k}{r^2}-\left(\frac{m}{r}+\frac{1}{r^2}\right)\delta_j^k\right]\frac{e^{-mr}}{r}\rightarrow$$

$$\partial_j\partial_k\frac{e^{-mr}}{r} = \left[\left(m^2+\frac{3m}{r}+\frac{3}{r^2}\right)\frac{x_jx_k}{r^2}-\left(m^2+\frac{3m}{r}+\frac{3}{r^2}\right)\frac{\delta_j^k}{3}+\frac{m^2\delta_j^k}{3}\right]\frac{e^{-mr}}{r}\rightarrow$$

$$\partial_j\partial_k\frac{e^{-mr}}{r} = \frac{m^2}{3}\left\{\left[1+\frac{3}{mr}+\frac{3}{(mr)^2}\right]\left(\frac{3x_jx_k}{r^2}-\delta_j^k\right)+\delta_j^k\right\}\frac{e^{-mr}}{r} \tag{F.18}$$

substituting back in Equation F.17:

$$V(\vec{r}) = \left[\left[\frac{-b^2}{3}\left\{\left[1+\frac{3}{m_Vr}+\frac{3}{(m_Vr)^2}\right]\left[3\left(\vec{s}_1\cdot\hat{r}\right)\left(\vec{s}_2\cdot\hat{r}\right)-\left(\vec{s}_1\cdot\vec{s}_2\right)\right]+\left(\vec{s}_1\cdot\vec{s}_2\right)\right\}-a^2+b^2\left(\vec{s}_1\cdot\vec{s}_2\right)\right]\right]$$

$$\times\left(-\frac{g^2}{4\pi}\frac{e^{-m_Vr}}{r}\right)\rightarrow V(\vec{r}) = V_C(\vec{r})\left[a^2-\frac{2b^2\left(\vec{s}_1\cdot\vec{s}_2\right)}{3}\right]+V_T(\vec{r})\frac{b^2}{3}\left[3\left(\vec{s}_1\cdot\hat{r}\right)\left(\vec{s}_1\cdot\hat{r}\right)-\left(\vec{s}_1\cdot\vec{s}_2\right)\right] \tag{F.19}$$

where

$$V_C(\vec{r}) = V_C(r) = \alpha\frac{e^{-m_Vr}}{r}\quad\text{and}\quad V_T(\vec{r}) = V_T(r) = \alpha\left[1+\frac{3}{m_Vr}+\frac{3}{(m_Vr)^2}\right]\frac{e^{-m_Vr}}{r} \tag{F.20}$$

F.1.3.3 Spinor DM and Massive Scalar and Pseudoscalar Mediator

The interaction lagrangian is $\mathcal{L}_{int}\propto\bar{\chi}\,\gamma^\mu\left(a+b\gamma^5\right)\chi\,\partial_\mu\phi$. The model $t-$channel interaction is shown in Figure F.3 and only one diagram is necessary.

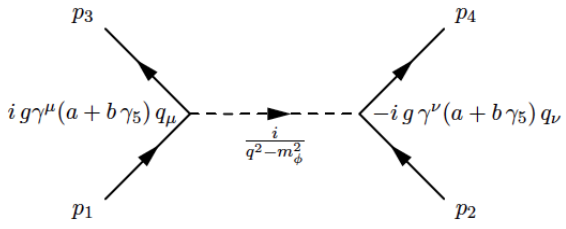

Figure F.3: $\chi\chi\rightarrow\phi\rightarrow\chi\chi$.

Conservation of four-momenta and momentum transfer are given by:

$$p_1^\mu + p_2^\mu = p_3^\mu + p_4^\mu \rightarrow q^\mu = p_3^\mu - p_1^\mu = p_2^\mu - p_4^\mu \tag{F.21}$$

and the matrix of vector and axial coefficients is:

$$A = a + b\,\gamma_5 = \begin{pmatrix} a-b & 0 \\ 0 & a+b \end{pmatrix} \tag{F.22}$$

with these definitions the matrix element for the process is:

$$i\,\mathcal{M} = i\,g^2\,\bar{u}_3 \not{q} A\,u_1 \frac{1}{q^2 - m_\phi^2}\,\bar{u}_4 \not{q} A\,u_2 = -i\frac{4b^2 m_\chi^2 g^2}{|\vec{q}|^2 + m_\phi^2}\left(\vec{\sigma}_1 \cdot \vec{r}\right)\left(\vec{\sigma}_2 \cdot \vec{r}\right)\delta_{s_1}^{s_3}\delta_{s_2}^{s_4} \tag{F.23}$$

The potential in momentum space is[2]:

$$V\left(\vec{q}\right) = \frac{b^2 g^2}{|\vec{q}|^2 + m_\phi^2}\left(\vec{\sigma}_1 \cdot \vec{r}\right)\left(\vec{\sigma}_2 \cdot \vec{r}\right)\delta_{s_1}^{s_3}\delta_{s_2}^{s_4}, \tag{F.24}$$

the potential in coordinate space is then:

$$V\left(\vec{r}\right) = -\frac{b^2 g^2 m_\phi^2}{12\pi}\left\{\left[1 + \frac{3}{m_\phi r} + \frac{3}{\left(m_\phi r\right)^2}\right]\left[3\left(\vec{s}_1 \cdot \hat{r}\right)\left(\vec{s}_2 \cdot \hat{r}\right) - \left(\vec{s}_1 \cdot \vec{s}_2\right)\right] + \left(\vec{s}_1 \cdot \vec{s}_2\right)\right\}\frac{e^{-m_\phi r}}{r} \rightarrow$$

$$V\left(\vec{r}\right) = -V_C\left(\vec{r}\right)\frac{b^2 m_\phi^2}{3}\left(\vec{s}_1 \cdot \vec{s}_2\right) - V_T\left(\vec{r}\right)\frac{b^2 m_\phi^2}{3}\left[3\left(\vec{s}_1 \cdot \hat{r}\right)\left(\vec{s}_1 \cdot \hat{r}\right) - \left(\vec{s}_1 \cdot \vec{s}_2\right)\right] \tag{F.25}$$

with the functions $V_C\left(\vec{r}\right)$ and $V_T\left(\vec{r}\right)$ given by Equation F.20 (and replacing m_V by m_ϕ). note that the scalar interaction can be dropped because in the non-relativistic limit it does not affect the potential.

F.1.3.4 Spin One Massive Boson DM and Scalar Mediator

The interaction lagrangian is $\mathcal{L}_{int} \propto g_{\mu\nu} B^\mu B^\nu \phi$. The model $t-$channel interaction is shown in Figure F.4 and only one diagram is necessary.

[2]Again the interaction conserves spin on each vertex.

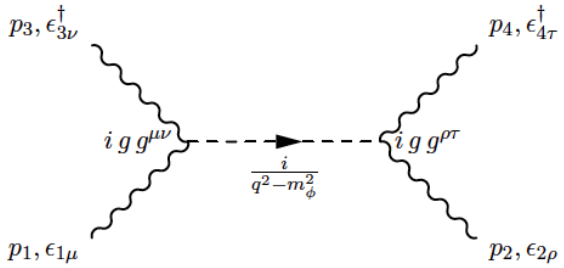

Figure F.4: $\chi\chi \to \phi \to \chi\chi$.

Conservation of four-momenta and momentum transfer are given by:

$$p_1^\mu + p_2^\mu = p_3^\mu + p_4^\mu \to q^\mu = p_3^\mu - p_1^\mu = p_2^\mu - p_4^\mu \tag{F.26}$$

with these definitions the matrix element for the process is:

$$i\,\mathcal{M} = -i\,g^2 \epsilon^{\dagger}_{3,\nu} g^{\mu\nu} \epsilon_{1,\mu} \frac{1}{q^2 - m_\phi^2} \epsilon^{\dagger}_{4,\tau} g^{\rho\tau} \epsilon_{2,\rho} \tag{F.27}$$

At this point it was decided that the best alternative should contain a chiral interaction to get a spin-dependent potential and the analysis of other options was interrupted. The key points to remember are that the matrix element should have terms proportional to linear momentum and spin in such a way that derivatives of the Yukawa potential appear and the potential depends on the spin similar to nuclear force potentials.

F.2 "Renormalization"

A cutoff of the potential is introduced but the long distance physics should be independent of this choice. The following analysis shows how this can be done for potentials with one discontinuity and how the matching conditions are imposed (Beane et al. 2001).

F.2.1 Preliminaries

The singular potentials we are interested in this work diverge worse than r^{-2} near the origin, therefore is necessary to apply some sort of modification at small distances:

$$V(r) = \frac{1}{2mr_0}\left[-\lambda_S \theta(r_c - r) - \lambda_L \frac{f(r/r_0)}{(r/r_0)^n}\theta(r - r_c)\right] \tag{F.28}$$

where $f(x)$ is a regular function near the origin, normalized to 1 at the origin and $r_c = \mathcal{R} \times r_0$.[3] An example of the renormalized potential is shown in Figure F.5. The Schroedinger equation becomes[4]:

$$\frac{d^2u(x)}{dx^2} + \eta^2 u(x) = \begin{cases} -\lambda_S u(x) & \text{if } x < \mathcal{R} \\ -\lambda_L \frac{f(x)}{x^n} u(x) & \text{if } x \geq \mathcal{R} \end{cases} \tag{F.29}$$

with $u(r) = R(r)/r$, $x = r/r_0$ and $\eta = \sqrt{2mr_0E}$. The solution near the origin is:

$$u(x) = A\cos\left(\sqrt{\eta^2 + \lambda_S}\, x + \delta_S\right) \tag{F.30}$$

but $\delta_S = -\pi/2$ then $u(x) = A\sin\left(\sqrt{\eta^2 + \lambda_S}\, x\right)$.

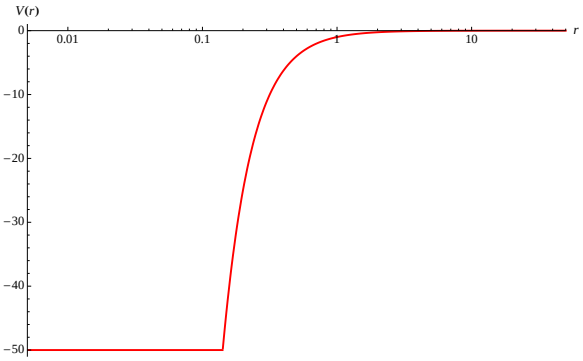

Figure F.5: Potential well for renormalization of singular potential.

Unfortunately there is no analytical solution for the general form given in Equation F.29 for $x > \mathcal{R}$.

F.2.1.1 Solution Near the Discontinuity ($\eta = 0$)

If $\eta = 0$ and $f(x) = 1$ the equation can be solved analytically. Usually there are two options to simplify a differential equation:

1. change of independent variable.
2. change of dependent variable.

[3] Note that there is no need of continuity on the potential.
[4] Notice that the angular momentum barrier is dropped in this analysis ($l = 0$ case).

In this case the first option proves more useful and the transform operators are:

$$\frac{d}{dx} = \frac{dz}{dx}\frac{d}{dz} \rightarrow \frac{d^2}{dx^2} = \frac{dz}{dx}\frac{d}{dz}\left(\frac{dz}{dx}\frac{d}{dz}\right) = \left(\frac{dz}{dx}\right)^2 \frac{d^2}{dz^2} + \frac{dz}{dx}\left[\frac{d}{dz}\left(\frac{dz}{dx}\right)\right]\frac{d}{dz} \tag{F.31}$$

the Schroedinger equation becomes then:

$$\frac{d^2u(x)}{dx^2} + \frac{\lambda_L}{x^n}u(x) = 0 \rightarrow \left(\frac{dz}{dx}\right)^2 \frac{d^2u(z)}{dz^2} + \frac{dz}{dx}\left[\frac{d}{dz}\left(\frac{dz}{dx}\right)\right]\frac{du(z)}{dz} + \frac{\lambda_L}{x^n}u(z) = 0 \tag{F.32}$$

to get rid of the x^n term multiply the equation by x^n/λ_L and making the coefficient of the second order derivative equal to one:

1. Case 1, $n > 2$:

$$\begin{gathered}\frac{x^n}{\lambda_L}\left(\frac{dz}{dx}\right)^2 = 1 \rightarrow z = \frac{\sqrt{\lambda_L}x^b}{b} \rightarrow x = \left(\frac{b\,z}{\sqrt{\lambda_L}}\right)^{1/b} \rightarrow \frac{dz}{dx} = \sqrt{\lambda_L}\left(\frac{b\,z}{\sqrt{\lambda_L}}\right)^{(b-1)/b} \rightarrow \\ \frac{d}{dz}\left(\frac{dz}{dx}\right) = \sqrt{\lambda_L}\left(\frac{b}{\sqrt{\lambda_L}}\right)^{(b-1)/b}\left(1-\frac{1}{b}\right)z^{(b-1)/b-1}\end{gathered} \tag{F.33}$$

with $b = 1 - n/2$, replacing the terms back in Equation F.32:

$$\begin{gathered}\frac{d^2u(z)}{dz^2} + \frac{1}{\lambda_L}\left(\frac{b\,z}{\sqrt{\lambda_L}}\right)^{n/b}\sqrt{\lambda_L}\left(\frac{b\,z}{\sqrt{\lambda_L}}\right)^{(b-1)/b}\sqrt{\lambda_L}\left(\frac{b}{\sqrt{\lambda_L}}\right)^{(b-1)/b} \\ \times\left(1-\frac{1}{b}\right)z^{(b-1)/b-1}\frac{du(z)}{dz} + u(z) = 0 \rightarrow \\ \frac{d^2u(z)}{dz^2} + \left(\frac{b}{\sqrt{\lambda_L}}\right)^{n/b+2(b-1)/b}\left(1-\frac{1}{b}\right)z^{n/b+2(b-1)/b-1}\frac{du(z)}{dz} + u(z) = 0 \rightarrow \\ \frac{d^2u(z)}{dz^2} + \left(1-\frac{1}{b}\right)\frac{1}{z}\frac{du(z)}{dz} + u(z) = 0\end{gathered} \tag{F.34}$$

this equation fails to be a Bessel's equation due to the coefficient of the first order derivative. At this point a transformation of the second kind will be very useful:

$$\begin{gathered}u(z) = z^a v(z) \rightarrow \frac{du(z)}{dz} = z^a\frac{dv(z)}{dz} + a\,z^{a-1}v(z) \rightarrow \\ \frac{d^2u(z)}{dz^2} = z^a\frac{d^2v(z)}{dz^2} + 2a\,z^{a-1}\frac{dv(z)}{dz} + a(a-1)z^{a-2}v(z).\end{gathered} \tag{F.35}$$

The new equation is:

$$z^2\frac{d^2v\left(z\right)}{dz^2}+\left(2a+1-\frac{1}{b}\right)z\frac{dv\left(z\right)}{dz}+\left[z^2+a\left(a-1\right)+\left(1-\frac{1}{b}\right)a\right]v\left(z\right)=0 \tag{F.36}$$

choosing $a=1/\left(2b\right)$ the coefficient of the first order derivative is fixed:

$$z^2\frac{d^2v\left(z\right)}{dz^2}+z\frac{dv\left(z\right)}{dz}+\left(z^2-\frac{1}{4b^2}\right)v\left(z\right)=0 \tag{F.37}$$

and *voilà*, the Bessel's equation. The solution is:

$$u\left(x\right)=\sqrt{x}\left[A\,J_{1/(2-n)}\left(\frac{\sqrt{\lambda_L}}{n/2-1}x^{1-n/2}\right)+B\,Y_{1/(2-n)}\left(\frac{\sqrt{\lambda_L}}{n/2-1}x^{1-n/2}\right)\right] \tag{F.38}$$

note that this solution is always valid because $J_\alpha\left(x\right)$ and $Y_\alpha\left(x\right)$ are always independent of each other (The solution shown in Bedaque's paper is not valid for $n=3$). For $x\ll 1$ and given that $n>2$ it is necessary to use asymptotic form of Bessel's functions:

$$\begin{gathered}u\left(x\right)\approx\sqrt{x}\sqrt{\frac{n-2}{\pi\sqrt{\lambda_L}}x^{n/2-1}}\left[A\cos\left(\frac{\sqrt{\lambda_L}}{n/2-1}x^{1-n/2}-\delta\right)+B\sin\left(\frac{\sqrt{\lambda_L}}{n/2-1}x^{1-n/2}-\delta\right)\right]\rightarrow\\ u\left(x\right)\approx\sqrt{\frac{n-2}{\pi\sqrt{\lambda_L}}}C'x^{n/4}\cos\left(\frac{\sqrt{\lambda_L}}{n/2-1}x^{1-n/2}-\delta+\phi'\right)\end{gathered} \tag{F.39}$$

with $\delta=\pi\left[1/4+1/\left(4-2n\right)\right]=\pi\left\{1/\left(2-n\right)-n/\left[4\left(n-2\right)\right]\right\}$, $\phi'=-\tan^{-1}\left(B/A\right)$ and $C^2=A^2+B^2$. Imposing continuity of the wave function and its derivative:

$$\begin{gathered}A\sin\left(\nu_S\mathcal{R}\right)=C\mathcal{R}^{n/4}\cos\left(\frac{\nu_L}{n/2-1}\mathcal{R}^{1-n/2}+\phi\right)\\ A\nu_S\cos\left(\nu_S\mathcal{R}\right)=C\left(\frac{n}{4}\mathcal{R}^{n/4-1}\cos\left(\frac{\nu_L}{n/2-1}\mathcal{R}^{1-n/2}+\phi\right)\right.\\ \left.+\nu_L\mathcal{R}^{n/4-n/2}\sin\left(\frac{\nu_L}{n/2-1}\mathcal{R}^{1-n/2}+\phi\right)\right)\end{gathered} \tag{F.40}$$

with obvious replacements and noting than the new phase depends on n but still constant. Dividing the first equation by the second equation:

$$\left(\nu_S\mathcal{R}\right)\cot\left(\nu_S\mathcal{R}\right)=H\cot\left(H\right)=\frac{n}{4}+\nu_L\mathcal{R}^{1-n/2}\tan\left(\frac{\nu_L}{n/2-1}\mathcal{R}^{1-n/2}+\phi\right). \tag{F.41}$$

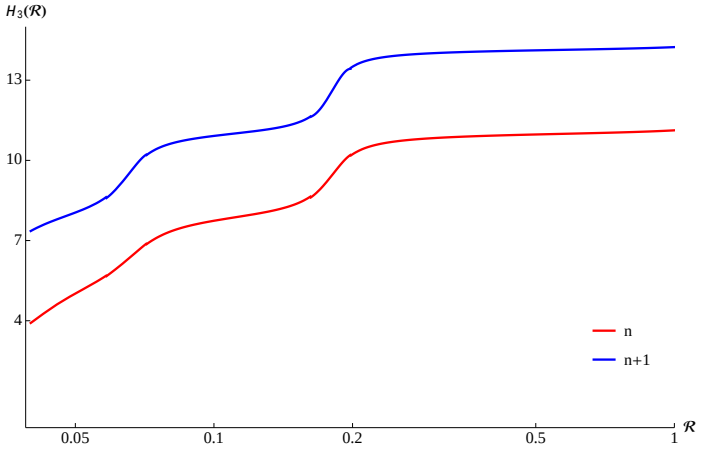

Figure F.6: Value of the coupling constant at short distances as function of the boundary point $\mathcal{R}$ for $n = 3$.

The discontinuities of the left-hand side are located where H is a multiple integer of π (with the exception of $H = 0$ where there is no discontinuity at all). Therefore a series expansion around those points allows to have an interpolating analytic function for $H(\mathcal{R})$ there:

$$\begin{gathered} m\pi + \epsilon = rhs \times \tan(\epsilon) \approx rhs \times \epsilon \rightarrow \epsilon \approx \frac{m\pi}{rhs - 1} \\ \rightarrow H(\mathcal{R}) \approx m\pi \frac{rhs}{rhs - 1} = m\pi \left(1 - \frac{1}{1 - rhs}\right) \rightarrow \\ H(\mathcal{R}) \approx m\pi \left[1 - \frac{1}{1 - n/4 - \nu_L \mathcal{R}^{1-n/2} \tan\left(\nu_L \mathcal{R}^{1-n/2} / (n/2 - 1) + \phi\right)}\right]. \end{gathered} \tag{F.42}$$

2. Case 2, $n = 2$:

$$\left(x \frac{dz}{dx}\right)^2 = 1 \rightarrow z = \ln(x) \rightarrow x = e^z \rightarrow \frac{dz}{dx} = e^{-z} \rightarrow \frac{d}{dz}\left(\frac{dz}{dx}\right) = -e^{-z} \tag{F.43}$$

replacing the terms back in Equation F.32:

$$e^{-2z}\left[\frac{d^2u(z)}{dz^2} - \frac{du(z)}{dz} + \lambda_L u(z)\right] = 0 \tag{F.44}$$

with the usual ansatz $u(z) = e^{az}$:

$$\begin{gathered} e^{az}\left(a^2 - a + \lambda_L\right) = 0 \rightarrow a = \frac{1 \pm \sqrt{1 - 4\lambda_L}}{2} \rightarrow u(x) = A_+ e^{a_+ z} + A_- e^{a_- z} \rightarrow \\ u(x) = \sqrt{x}\left[A_+ x^{\sqrt{1/4 - \lambda_L}} + A_- x^{-\sqrt{1/4 - \lambda_L}}\right] \end{gathered} \tag{F.45}$$

which is valid for any value of λ_L, however there is a more useful form when $\lambda_L > 1/4$ and with $\sqrt{\lambda_L - 1/4}$:

$$u(x) = C\sqrt{x}\cos\left(\nu_L \ln(x) + \phi\right). \tag{F.46}$$

The matching conditions are:

$$A\sin\left(\nu_S \mathcal{R}\right) = C\sqrt{\mathcal{R}}\cos\left(\nu_L \ln(\mathcal{R}) + \phi\right) \tag{F.47a}$$

$$A\nu_S \cos\left(\nu_S \mathcal{R}\right) = \frac{C}{\sqrt{\mathcal{R}}}\left(\frac{\cos\left(\nu_L \ln(\mathcal{R}) - \phi\right)}{2} + \nu_L \sin\left(\nu_L \ln(\mathcal{R}) + \phi\right)\right) \tag{F.47b}$$

and, to eliminate the multiplicative constants, dividing the second equation by the first equation:

$$\left(\nu_S \mathcal{R}\right)\cot\left(\nu_S \mathcal{R}\right) = H\cot(H) = \nu_L\left(\frac{1}{2\nu_L} - \tan\left(\nu_L \ln(\mathcal{R}) + \phi\right)\right). \tag{F.48}$$

The discontinuities of the left-hand side are located where H is a multiple integer of π (with the exception of $H = 0$ where there is no discontinuity at all). Therefore an expansion around those points allows a better comprehension of the behavior of $H(\mathcal{R})$:

$$\begin{gathered} H = m\pi + \epsilon \rightarrow (m\pi + \epsilon)\cot(\epsilon) = rhs \rightarrow (m\pi + \epsilon) \approx rhs \times \epsilon \rightarrow \\ \epsilon \approx \frac{m\pi}{rhs - 1} \rightarrow H \approx m\pi \frac{rhs}{rhs - 1} \rightarrow \\ H(\mathcal{R}) \approx m\pi\left[\frac{1/2 - \nu_L \tan\left(\nu_L \ln(\mathcal{R}) + \phi\right)}{-1/2 - \nu_L \tan\left(\nu_L \ln(\mathcal{R}) + \phi\right)}\right] \approx m\pi\left[\frac{\sin\left(\nu_L \ln(\mathcal{R}) + \phi - \delta\right)}{\sin\left(\nu_L \ln(\mathcal{R}) + \phi + \delta\right)}\right] \end{gathered} \tag{F.49}$$

with $2\nu_L \tan(\delta) = 1$.

F.2.1.2 Solution Near the Discontinuity ($\eta \neq 0$)

When $\eta \neq 0$ the second part of Equation F.29 can be solved analytically for $n = 2$, other values of n need a numerical approach.

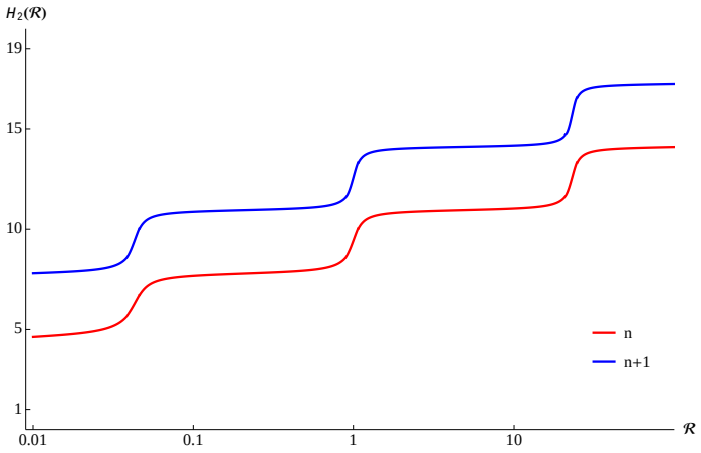

Figure F.7: Value of the coupling constant at short distances as function of the boundary point $\mathcal{R}$ for $n = 2$.

1. Case 1, the Schroedinger's equation for $n = 2$ is:

$$\frac{d^2u(x)}{dx^2} + \left(\eta^2 + \lambda_L \frac{1}{x^2}\right) u(x) = 0 \rightarrow x^2 \frac{d^2u(x)}{dx^2} + \left(\eta^2 x^2 + \lambda_L\right) u(x) = 0 \tag{F.50}$$

which is reminiscent of Bessel's equation but fails to be one due to two aspects: the coefficient η of x^2 monomial (this can be solved through a scaling transformation $y = \eta x$) and the missing first order derivative (this can be solved through an appropriate ansatz). Trying the ansatz $u(x) = x^a v(x)$:

$$x^a \left[a(a-1) v(x) + 2ax \frac{dv(x)}{dx} + x^2 \frac{d^2v(x)}{dx^2}\right] + \left(\eta^2 x^2 + \lambda_L\right) x^a v(x) = 0 \tag{F.51}$$

and choosing $a = 1/2$:

$$x^2 \frac{d^2v(x)}{dx^2} + x \frac{dv(x)}{dx} + \left(\eta^2 x^2 + \lambda_L - \frac{1}{4}\right) v(x) = 0. \tag{F.52}$$

Finally applying the scaling transformation:

$$y^2 \frac{d^2v(y)}{dy^2} + y \frac{dv(y)}{dy} + \left[y^2 - \left(\frac{1}{4} - \lambda_L\right)\right] v(y) = 0 \tag{F.53}$$

which is Bessel's equation, then the solution is:

$$u(x) = \sqrt{x}\left(A_+ J_\nu(\eta x) + A_- J_{-\nu}(\eta x)\right) \tag{F.54}$$

with $\nu = \sqrt{1/4 - \lambda_L}$. The small x behavior is given by:

$$u(x) \approx \sqrt{x}\left[A_+ \frac{1}{\Gamma(1+\nu)}\left(\frac{\eta x}{2}\right)^{\nu} + A_- \frac{1}{\Gamma(1-\nu)}\left(\frac{\eta x}{2}\right)^{-\nu}\right] \tag{F.55}$$

for ν real only the second term is relevant, but when $\lambda_L > 1/4$ both terms contribute (replacing $\nu_1 = \sqrt{\lambda_L - 1/4}$):

$$u(x) \approx \sqrt{x}\left[\frac{A_+}{\Gamma(1+i\nu_1)}\left(\frac{\eta x}{2}\right)^{i\nu_1} + \frac{A_-}{\Gamma(1-i\nu_1)}\left(\frac{\eta x}{2}\right)^{-i\nu_1}\right] \tag{F.56}$$

but $\Gamma(\bar{z}) = \overline{\Gamma(z)}$ and the linear superposition of complex conjugate complex exponentials can be replaced by a sinusoidal function with a phase, then:

$$\begin{aligned} u(x) \approx \sqrt{x}\Big[&A_+ \exp\left(\ln\left(\Gamma(1+i\nu_1)\right) + i\nu_1 \ln\left(\frac{\eta x}{2}\right)\right) \\ &+ A_- \exp\left(\ln\left(\Gamma(1-i\nu_1)\right) - i\nu_1 \ln\left(\frac{\eta x}{2}\right)\right)\Big] \rightarrow \\ u(x) \approx A\sqrt{x}\cos&\left(\nu_1 \ln\left(\frac{\eta x}{2}\right) - \Im\left(\Gamma(1+i\nu_1)\right) + \phi\right). \end{aligned} \tag{F.57}$$

2. Case 2, the Schroedinger's equation for $n > 2$ is:

$$\frac{d^2 u(x)}{dx^2} + \left(\eta^2 + \lambda_L \frac{f(x)}{x^n}\right) u(x) = 0 \tag{F.58}$$

substituting the ansatz $u(x) = a(x)\, e^{ib(x)}$ back into Equation F.58:

$$\begin{aligned} \Bigg[&\frac{d^2 a(x)}{dx^2} + 2i\frac{da(x)}{dx}\frac{db(x)}{dx} + ia(x)\frac{d^2 b(x)}{dx^2} - a(x)\left(\frac{db(x)}{dx}\right)^2 \\ &+ \left(\eta^2 + \lambda_L \frac{f(x)}{x^n}\right) a(x)\Bigg] e^{ib(x)} = 0 \end{aligned} \tag{F.59}$$

the imaginary part is:

$$2\frac{da\left(x\right)}{dx}\frac{db\left(x\right)}{dx}+a\left(x\right)\frac{d^{2}b\left(x\right)}{dx^{2}}=0\rightarrow\frac{d}{dx}\left(a^{2}\left(x\right)\frac{db\left(x\right)}{dx}\right)=0\rightarrow a^{2}\left(x\right)\frac{db\left(x\right)}{dx}=C^{2} \tag{F.60}$$

and the real part:

$$\frac{1}{a\left(x\right)}\frac{d^{2}a\left(x\right)}{dx^{2}}-\left(\frac{db\left(x\right)}{dx}\right)^{2}+\eta^{2}+\lambda_{L}\frac{f\left(x\right)}{x^{n}}=0 \tag{F.61}$$

neglecting the second order derivative term:

$$\begin{gathered}-\left(\frac{db\left(x\right)}{dx}\right)^{2}+\eta^{2}+\lambda_{L}\frac{f\left(x\right)}{x^{n}}\approx0\rightarrow b\left(x\right)\approx\pm\int^{x}\sqrt{\eta^{2}+\lambda_{L}\frac{f\left(x_{1}\right)}{x_{1}^{n}}}\,dx_{1}\rightarrow\\ a\left(x\right)\approx\frac{C}{\sqrt[4]{\eta^{2}+\lambda_{L}\frac{f(x)}{x^{n}}}}.\end{gathered} \tag{F.62}$$

The approximate solution is:

$$u\left(x\right)\approx\frac{1}{\sqrt[4]{\eta^{2}+\lambda_{L}\frac{f(x)}{x^{n}}}}\cos\left(\int_{x_{0}}^{x}\sqrt{\eta^{2}+\lambda_{L}\frac{f\left(x_{1}\right)}{x_{1}^{n}}}\,dx_{1}\right) \tag{F.63}$$

when $\eta\rightarrow0$ Equation F.39 is recovered.

Solution for the General Case. Because the solution for $\eta=0$ is known for all cases the general solution can be written as:

$$u_{\eta}\left(x\right)=A\left(x;\eta\right)u_{0}\left(x\right) \tag{F.64}$$

where all dependence on the energy η is contained in the function $A\left(x\right)$. Replacing back into the second part of Equation F.29 with $f\left(x\right)=1$:

$$\begin{gathered}A\left(x\right)\frac{d^{2}u_{0}\left(x\right)}{dx^{2}}+2\frac{dA\left(x\right)}{dx}\frac{du_{0}\left(x\right)}{dx}+\frac{d^{2}A\left(x\right)}{dx^{2}}u_{0}\left(x\right)+\left(\eta^{2}+\frac{\lambda_{L}}{x^{n}}\right)A\left(x\right)u_{0}\left(x\right)=0\rightarrow\\ 2\frac{dA\left(x\right)}{dx}\frac{du_{0}\left(x\right)}{dx}+\frac{d^{2}A\left(x\right)}{dx^{2}}u_{0}\left(x\right)+\eta^{2}A\left(x\right)u_{0}\left(x\right)=0\rightarrow\\ \frac{d^{2}A\left(x\right)}{dx^{2}}+2\frac{d\ln\left(u_{0}\left(x\right)\right)}{dx}\frac{dA\left(x\right)}{dx}+\eta^{2}A\left(x\right)=0.\end{gathered} \tag{F.65}$$

1. When the dominant term is the one containing the first order derivative then the leading term of the approximate solution is:

$$\begin{gathered}\frac{dA_0(x)}{dx}=0\rightarrow A_0(x)=constant=A_0\rightarrow\\ \frac{dA_1(x)}{dx}=-\frac{\eta^2A_0}{2}\frac{u_0(x)}{u'(x;0)}\rightarrow A_1(x)=-\frac{\eta^2A_0}{2}\int_0^x\frac{u_0(x_1)}{u_0'(x_1)}dx_1\rightarrow\\ A(x)\approx A_0\left(1-\frac{\eta^2}{2}\int_0^x\frac{u_0(x_1)}{u_0'(x_1)}dx_1\right)\end{gathered}\tag{F.66}$$

2. The general perturbative solution starts with a series expansion in the perturbative parameter η^2, $A(x)=\sum_{j=0}^{\infty}A_j(x)\eta^{2j}$. Replacing back into Equation F.65:

$$\sum_{j=0}^{\infty}\left(\frac{d^2A_j(x)}{dx^2}+2\frac{d\ln(u_0(x))}{dx}\frac{dA_j(x)}{dx}\right)\eta^{2j}+\sum_{j=0}^{\infty}A_j(x)\eta^{2j+2}=0\tag{F.67}$$

which should be true for each power of η^2:

$$\frac{d^2A_0(x)}{dx^2}+2\frac{d\ln(u_0(x))}{dx}\frac{dA_0(x)}{dx}=0\tag{F.68a}$$

$$\frac{d^2A_1(x)}{dx^2}+2\frac{d\ln(u_0(x))}{dx}\frac{dA_1(x)}{dx}+A_0(x)=0\tag{F.68b}$$

$$\frac{d^2A_{j+1}(x)}{dx^2}+2\frac{d\ln(u_0(x))}{dx}\frac{dA_{j+1}(x)}{dx}+A_j(x)=0.\tag{F.68c}$$

The solution to Equation F.68a is:

$$\frac{d\left(v(x)u_0^2(x)\right)}{dx}=0\rightarrow\frac{dA_0(x)}{dx}=\frac{c_{0,1}}{u_0^2(x)}\rightarrow A_0(x)=c_{0,1}\int^x\frac{dx_1}{u_0^2(x_1)}+c_{0,2}\tag{F.69}$$

and introducing this into Equation F.68b:

$$\begin{gathered}\frac{dv(x)}{dx}+2\frac{d\ln(u_0(x))}{dx}v(x)+c_{0,1}\int^x\frac{dx_1}{u_0^2(x_1)}+c_{0,2}=0\rightarrow\\ \frac{d\left(v(x)u_0^2(x)\right)}{dx}+\left(c_{0,1}\int^x\frac{dx_1}{u_0^2(x_1)}+c_{0,2}\right)u_0^2(x)=0\rightarrow\\ A_1(x)=-\int^x\frac{1}{u_0^2(x_1)}\left[\int^{x_1}\left(c_{0,1}\int^{x_2}\frac{dx_3}{u_0^2(x_3)}+c_{0,2}\right)u_0^2(x_2)\,dx_2+c_{1,2}\right]dx_1.\end{gathered}\tag{F.70}$$

F.2.1.3 Perturbative Solution to Schroedinger's Equation

Perturbation method applied to second part of Equation F.29:

$$u(x)=\sum_{j=0}^{\infty}u_j(x)\,\eta^{2j}\rightarrow\sum_{j=0}^{\infty}\left(\frac{d^2u_j(x)}{dx^2}+\frac{\lambda_L}{x^n}u_j(x)\right)\eta^{2j}+\sum_{j=0}^{\infty}u_j(x)\,\eta^{2j+2}=0\rightarrow \tag{F.71}$$

matching coefficients of power of η:

$$\frac{d^2u_0(x)}{dx^2}+\frac{\lambda_L}{x^n}u_0(x)=0 \tag{F.72a}$$

$$\frac{d^2u_j(x)}{dx^2}+\frac{\lambda_L}{x^n}u_j(x)+u_{j-1}(x)=0\quad j\in\{1,2,\dots\} \tag{F.72b}$$

the solution to Equation F.72a was worked out in Section F.2.1.1, the solution to Equation F.72b for $j=1$ can be written as $u_1(x)=f(x)\,u_0(x)$:

$$\begin{gathered}\left(\frac{d^2u_0(x)}{dx^2}+\frac{\lambda_L}{x^n}u_0(x)\right)f(x)+\frac{d^2f(x)}{dx^2}u_0(x)+2\frac{df(x)}{dx}\frac{du_0(x)}{dx}+u_0(x)=0\rightarrow\\ \frac{d}{dx}\left(\frac{df(x)}{dx}u_0^2(x)\right)+u_0^2(x)=0\rightarrow f(x)=c_2+\int^x\left(\frac{c_1}{u_0^2(x_1)}-\int^{x_1}\frac{u_0^2(x_2)}{u_0^2(x_1)}dx_2\right)dx_1\end{gathered} \tag{F.73}$$

which gives the approximate solution up to first order in η^2:

$$u(x)\approx\left\{1+\eta^2\left[c_2+\int^x\left(\frac{c_1}{u_0^2(x_1)}-\int^{x_1}\frac{u_0^2(x_2)}{u_0^2(x_1)}dx_2\right)dx_1\right]\right\}u_0(x) \tag{F.74}$$

F.3 Sommerfeld Enhancement

The partial wave expansion $\psi(\vec{r})=\sum_{l=0}^{\infty}(2l+1)\,P_l(\cos\theta)\,u(r)/r$ reduces Schroedinger's equation for a central potential to (Tulin et al. 2013c; Arkani-Hamed et al. 2009):

$$\frac{d^2u_l(r)}{dr^2}+\left\{2M\left[E-\left(-V_0\theta(R-r)-\frac{g}{M^2r^n}\theta(r-R)\right)\right]-\frac{l(l+1)}{r^2}\right\}u_l(r)=0 \tag{F.75}$$

with $u_l(0)=0$ and continuity of the wave function and its derivative at $r=R$.

F.3.1 Free Particle

Using the ansatz $u_l(r) = r^a v_l(r)$ the equation for the free particle becomes:

$$r^2 \frac{d^2 v_l(r)}{dr^2} + 2ar \frac{dv_l(r)}{dr} + \left[k^2 r^2 + a(a-1) - l(l+1)\right] v_l(r) = 0 \tag{F.76}$$

choosing $a = 1/2$ Equation F.76 reduces to Bessel's equation:

$$\begin{gathered} r^2 \frac{d^2 v_l(r)}{dr^2} + r \frac{dv_l(r)}{dr} + \left\{k^2 r^2 - \left[\frac{1}{4} + l(l+1)\right]\right\} v_l(r) = 0 \rightarrow \\ u_l(r) = \begin{cases} \sqrt{r}\left(A J_{\alpha_l}(kr) + B J_{-\alpha_l}(kr)\right) & l > 0 \\ A \sin(kr) + B \cos(kr) & l = 0 \end{cases} \end{gathered} \tag{F.77}$$

with $\alpha_l = \sqrt{1/4 + l(l+1)}$. The boundary condition $u_l(0) = 0$ makes $B = 0$ in both cases.

F.3.2 Non-zero Potential

The solution inside the potential well has the same form as the free particle's solution but replacing k with $\omega = \sqrt{k^2 + 2MV_0}$:

$$u_l(r) = \begin{cases} A\sqrt{r} J_{\alpha_l}(\omega r) & l > 0 \\ A \sin(\omega r) & l = 0. \end{cases} \tag{F.78}$$

For $r > R$ the equation is:

$$\frac{d^2 u_l(r)}{dr^2} + \left[k^2 + \frac{2g}{Mr^n} - \frac{l(l+1)}{r^2}\right] u_l(r) = 0. \tag{F.79}$$

unfortunately, this equation cannot be solved analytically and has to be solved numerically. For $l = 0$ (or $r \ll \{2g/[l(l+1)M]\}^{1/(n-2)}$), $n \neq 2$ and k small the solution can be approximate by:

$$u_l(r) \approx \sqrt{r}\left[A\, J_{1/(2-n)}\left(\frac{1}{n/2-1}\sqrt{\frac{2g}{M}}\, r^{1-n/2}\right) + B\, Y_{1/(2-n)}\left(\frac{1}{n/2-1}\sqrt{\frac{2g}{M}}\, r^{1-n/2}\right)\right] \tag{F.80}$$

which in the small x limit behaves like a sinusoidal wave:

$$u_l(r) \approx C r^{n/4} \sin\left(\frac{1}{n/2-1}\sqrt{\frac{2g}{M}}\, r^{1-n/2} + \phi\right). \tag{F.81}$$

F.3.2.1 Continuity and Boundary Conditions for a Three-section Potential

Imposing an asymptotic condition when solving numerically an ODE is not possible unless a definition of long distance is introduce. One way of doing this is splitting the independent variable into two regions: asymptotic and non-asymptotic regions. Therefore the solution is:

$$u_0(r) \approx \begin{cases} A\,F_1(r) + B\,F_2(r) & \text{for } r < R \\ C\,G_1(r) + D\,G_2(r) & \text{for } R < r < R_1 \\ G\sin(kr + \delta_0) & \text{for } R_1 < r \end{cases} \tag{F.82}$$

then assume that $F_1(0) = 0$ and $F_2(0) \neq 0$. When combined with $u_0(0) = 0$ implies that $B = 0$.

The derivative is:

$$\frac{du_0(r)}{dr} \approx \begin{cases} A\,f_1(r) & \text{for } r < R \\ C\,g_1(r) + D\,g_2(r) & \text{for } R < r < R_1 \\ k\,G\cos(kr + \delta_0) & \text{for } R_1 < r. \end{cases} \tag{F.83}$$

Imposing the continuity at the first interface:

$$\begin{aligned} A\,F_1(R) &= C\,G_1(R) + D\,G_2(R) \\ A\,f_1(R) &= C\,g_1(R) + D\,g_2(R) \end{aligned} \tag{F.84}$$

which reduces to:

$$D = \frac{F_1(R)\,g_1(R) - f_1(R)\,G_1(R)}{f_1(R)\,G_2(R) - F_1(R)\,g_2(R)} C = h(R)\;C. \tag{F.85}$$

Similarly, imposing the continuity at the second interface:

$$\begin{aligned} C\left(G_1(R_1) + h(R)\,G_2(R_1)\right) &= G\sin(kr + \delta_0) \\ C\left(g_1(R_1) + h(R)\,g_2(R_1)\right) &= k\,G\cos(kr + \delta_0) \end{aligned} \tag{F.86}$$

solving for C:

$$\frac{C^2}{G^2} = \frac{1}{\left(G_1(R_1) + h(R)\,G_2(R_1)\right)^2 + \left(g_1(R_1) + h(R)\,g_2(R_1)\right)^2/k^2}. \tag{F.87}$$

The problem now is to choose an adequate point (R_1) to describe the large distance behavior of the wave function (note that in this case there is no renormalization procedure as there is for the short distance behavior).

F.4 Collisionless DM

With all the machinery setup a final step was necessary to actually solve the Schroedinger's equation for the selected potential. The idea was to follow an algorithm devised by Zurek (McDermott et al. 2012; Tulin et al. 2013c,b,a) with the new potential and dropping some of the most divergent terms. Obviously a reproduction of their results were necessary and are shown in Figure F.8.

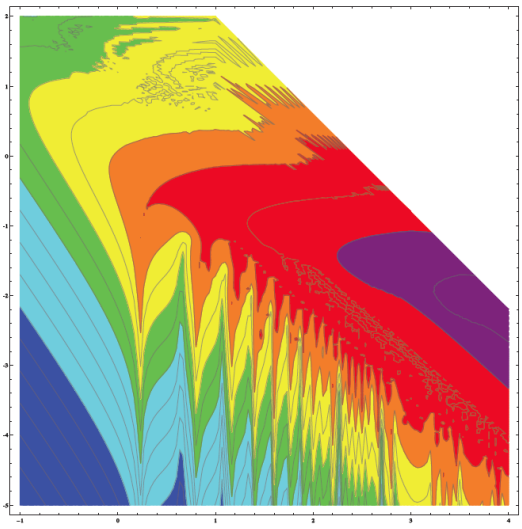

Figure F.8: Contours of (normalized) cross-section in the plane $a-b$ with $a = {}^{v}/_{2\alpha_X}$ and $b = {}^{\alpha_X m_\chi}/_{m_\phi}$.

F.4.1 The Numerical Algorithm

Define $\chi_l = r\,R_l\,(r)$, $x = \alpha_X m_X r$, $a = v/\,(2\,\alpha_X)$ and $b = \alpha_x\,m_X/m_\phi$, then:

$$\left(\frac{d^2}{dx^2} + a^2 - \frac{l\,(l+1)}{x^2} \pm \frac{1}{x}e^{-x/b}\right)\chi_l\,(x) = 0 \tag{F.88}$$

for given l, a and b:

1. Choose x_0 close to the origin and make $\chi\,(x_0) = 1$ and $\chi'\,(x_1) = (l+1)\,/x_0$.

2. Choose x_1 such as $a^2 \gg exp\left(-x_1/b\right)/x_1$ then solve numerically Eq. F.88 for $x_0 < x < x_1$.
3. At x_1 match solution to asymptotic solution:

$$\chi_l \propto x\, e^{i\delta_l} \left(\cos\left(\delta_l\right)\, j_l\left(a\, x\right) - \sin\left(\delta_l\right) n_l\left(a\, x\right)\right) \tag{F.89}$$

   solve Eq. F.89 for δ_l. Repeat procedure until variation is less than a fixed amount.
4. Compute σ_T, for this include terms in the summation until the variation is less than a fixed amount.

Note that in Figure F.8 the contours are not well defined in some regions due to numerical instabilities, i.e., a greater density in the grid and smaller tolerance are required. However the main features are shown, the large and narrow regions in which the cross-section increases are the points where Sommerfeld enhancement occur. At this point it was decided that no further work was going to be done in this project.

References

Georges Aad et al. Search for New Phenomena in $t\bar{t}$ Events With Large Missing Transverse Momentum in Proton-Proton Collisions at $\sqrt{s} = 7$ TeV with the ATLAS Detector. *Phys.Rev.Lett.*, 108:041805, 2012a. doi: 10.1103/PhysRevLett.108.041805.

Georges Aad et al. Observation of a New Particle in the Search for the Standard Model Higgs Boson with the ATLAS Detector at the LHC. *Phys.Lett.*, B716:1–29, 2012b. doi: 10.1016/j.physletb.2012.08.020.

Georges Aad et al. Search for Dark Matter Candidates and Large Extra Dimensions in Events with a Jet and Missing Transverse Momentum with the ATLAS Detector. *JHEP*, 1304:075, 2013. doi: 10.1007/JHEP04(2013)075.

Georges Aad et al. Search for Dark Matter in Events with a Hadronically Decaying W or Z Boson and Missing Transverse Momentum in pp Collisions at $\sqrt{s}$=8 TeV with the ATLAS Detector. *Phys.Rev.Lett.*, 112:041802, 2014a. doi: 10.1103/PhysRevLett.112.041802.

Georges Aad et al. Search for Direct Production of Charginos and Neutralinos in Events with Three Leptons and Missing Transverse Momentum in $\sqrt{s} = 8$ TeV pp Collisions with the ATLAS Detector. 2014b.

V.M. Abazov et al. Evidence for Production of Single Top Quarks. *Phys.Rev.*, D78:012005, 2008. doi: 10.1103/PhysRevD.78.012005.

A.A. Abdo et al. Fermi Large Area Telescope View of the Core of the Radio Galaxy Centaurus A. *Astrophys.J.*, 719:1433–1444, 2010. doi: 10.1088/0004-637X/719/2/1433.

M. Ackermann et al. Search for Gamma-ray Spectral Lines with the Fermi Large Area Telescope and Dark Matter Implications. *Phys.Rev.*, D88:082002, 2013. doi: 10.1103/PhysRevD.88.082002.

P.A.R. Ade et al. Planck 2013 results. XVI. Cosmological parameters. 2013.

Prateek Agrawal, Zackaria Chacko, Can Kilic, and Rashmish K. Mishra. A Classification of Dark Matter Candidates with Primarily Spin-Dependent Interactions with Matter. 2010.

D.S. Akerib et al. Technical Results from the Surface Run of the LUX Dark Matter Experiment. *Astropart.Phys.*, 45:34–43, 2013a. doi: 10.1016/j.astropartphys.2013.02.001.

D.S. Akerib et al. First Results from the LUX Dark Matter Experiment at the Sanford Underground Research Facility. 2013b.

A. Albert. Search for Gamma-ray Spectral Lines in the Milky Way Diffuse with the Fermi Large Area Telescope, 11 2012. The Fermi Symposium.

Johan Alwall, Michel Herquet, Fabio Maltoni, Olivier Mattelaer, and Tim Stelzer. MadGraph 5 : Going Beyond. *JHEP*, 1106:128, 2011. doi: 10.1007/JHEP06(2011)128.

E. Aprile et al. Dark Matter Results from 225 Live Days of XENON100 Data. *Phys.Rev.Lett.*, 109: 181301, 2012. doi: 10.1103/PhysRevLett.109.181301.

Elena Aprile. The XENON1T Dark Matter Search Experiment. 2012.

Nima Arkani-Hamed, Douglas P. Finkbeiner, Tracy R. Slatyer, and Neal Weiner. A Theory of Dark Matter. *Phys.Rev.*, D79:015014, 2009. doi: 10.1103/PhysRevD.79.015014.

Sebastian Arrenberg, Howard Baer, Vernon Barger, Laura Baudis, Daniel Bauer, et al. Dark Matter in the Coming Decade: Complementary Paths to Discovery and Beyond. 2013.

Max Baak and Roman Kogler. The Global Electroweak Standard Model Fit After the Higgs Discovery. pages 349–358, 2013.

Howard Baer, Vernon Barger, Gabe Shaughnessy, Heaya Summy, and Lian-tao Wang. Precision Gluino Mass at the LHC in SUSY Models with Decoupled Scalars. *Phys.Rev.*, D75:095010, 2007. doi: 10.1103/PhysRevD.75.095010.

Yang Bai and Joshua Berger. Fermion Portal Dark Matter. *JHEP*, 1311:171, 2013. doi: 10.1007/JHEP11(2013)171.

Yang Bai and Joshua Berger. Lepton Portal Dark Matter. 2014.

Yang Bai, Patrick J. Fox, and Roni Harnik. The Tevatron at the Frontier of Dark Matter Direct Detection. *JHEP*, 1012:048, 2010. doi: 10.1007/JHEP12(2010)048.

Vernon Barger, Wai-Yee Keung, and Gabe Shaughnessy. Spin Dependence of Dark Matter Scattering. *Phys.Rev.*, D78:056007, 2008a. doi: 10.1103/PhysRevD.78.056007.

Vernon Barger, Paul Langacker, Mathew McCaskey, Michael J. Ramsey-Musolf, and Gabe Shaughnessy. LHC Phenomenology of an Extended Standard Model with a Real Scalar Singlet. *Phys.Rev.*, D77:035005, 2008b. doi: 10.1103/PhysRevD.77.035005.

Vernon D. Barger, Tao Han, and J. Ohnemus. Heavy Leptons at Hadron Supercolliders. *Phys.Rev.*, D37:1174, 1988. doi: 10.1103/PhysRevD.37.1174.

Roger J. Barlow. Event Classification Using Weighting Methods. *J.Comput.Phys.*, 72:202–219, 1987. doi: 10.1016/0021-9991(87)90078-7.

Valeria Bartsch and Gunter Quast. Expected Signal Observability at Future Experiments. 2005.

S.R. Beane, Paulo F. Bedaque, L. Childress, A. Kryjevski, J. McGuire, et al. Singular Potentials and Limit Cycles. *Phys.Rev.*, A64:042103, 2001. doi: 10.1103/PhysRevA.64.042103.

Paulo F. Bedaque, Michael I. Buchoff, and Rashmish K. Mishra. Sommerfeld Enhancement from Goldstone Pseudo-scalar Exchange. *JHEP*, 0911:046, 2009. doi: 10.1088/1126-6708/2009/11/046.

G. Belanger, F. Boudjema, P. Brun, A. Pukhov, S. Rosier-Lees, et al. Indirect Search for Dark Matter with MicrOMEGAs2.4. *Comput.Phys.Commun.*, 182:842–856, 2011. doi: 10.1016/j.cpc.2010.11.033.

G. Belanger, F. Boudjema, and A. Pukhov. MicrOMEGAs : A Code for the Calculation of Dark Matter Properties in Generic Models of Particle Interaction. 2014a.

G. Belanger, F. Boudjema, A. Pukhov, and A. Semenov. MicrOMEGAs3: A Program for Calculating Dark Matter Observables. *Comput.Phys.Commun.*, 185:960–985, 2014b. doi: 10.1016/j.cpc.2013.10.016.

Maria Beltran, Dan Hooper, Edward W. Kolb, and Zosia C. Krusberg. Deducing the Nature of Dark Matter from Direct and Indirect Detection Experiments in the Absence of Collider Signatures of New Physics. *Phys.Rev.*, D80:043509, 2009. doi: 10.1103/PhysRevD.80.043509.

Maria Beltran, Dan Hooper, Edward W. Kolb, Zosia A.C. Krusberg, and Tim M.P. Tait. Maverick Dark Matter at Colliders. *JHEP*, 1009:037, 2010. doi: 10.1007/JHEP09(2010)037.

Carl M. Bender, Nick E. Mavromatos, and Sarben Sarkar. Asymptotic Analysis of the Boltzmann Equation for Dark Matter Relics in the Presence of a Running Dilaton and Space-Time Defects. *Phys.Rev.*, D87(5):055021, 2013. doi: 10.1103/PhysRevD.87.055021.

C.L. Bennett et al. Nine-Year Wilkinson Microwave Anisotropy Probe (WMAP) Observations: Final Maps and Results. *Astrophys.J.Suppl.*, 208:20, 2013. doi: 10.1088/0067-0049/208/2/20.

Lars Bergstrom. Saas-Fee Lecture Notes: Multi-messenger Astronomy and Dark Matter. 2012.

Lars Bergstrom, Gianfranco Bertone, Jan Conrad, Christian Farnier, and Christoph Weniger. Investigating Gamma-Ray Lines from Dark Matter with Future Observatories. *JCAP*, 1211:025, 2012. doi: 10.1088/1475-7516/2012/11/025.

R. Bernabei. Dark Matter Searches. pages 104–121, 2004.

R. Bernabei, Pierluigi Belli, F. Cappella, R. Cerulli, F. Montecchia, et al. Dark Matter Search. *Riv.Nuovo Cim.*, 26N1:1–73, 2003.

G. Bertone, editor. *Particle Dark Matter: Observations, Models and Searches*. Cambridge University Press, 02 2010.

G. Bertone, D.G. Cerdeno, M. Fornasa, L. Pieri, R. Ruiz de Austri, et al. Complementarity of Indirect and Accelerator Dark Matter Searches. *Phys.Rev.*, D85:055014, 2012a. doi: 10.1103/PhysRevD.85.055014.

Gianfranco Bertone and David Merritt. Time-dependent Models for Dark Matter at the Galactic Center. *Phys.Rev.*, D72:103502, 2005. doi: 10.1103/PhysRevD.72.103502.

Gianfranco Bertone, Dan Hooper, and Joseph Silk. Particle dark matter: Evidence, Candidates and Constraints. *Phys.Rept.*, 405:279–390, 2005. doi: 10.1016/j.physrep.2004.08.031.

Gianfranco Bertone, C.B. Jackson, Gabe Shaughnessy, Tim M.P. Tait, and Alberto Vallinotto. The WIMP Forest Indirect Detection of a Chiral Square. *Phys.Rev.*, D80:023512, 2009. doi: 10.1103/PhysRevD.80.023512.

Gianfranco Bertone, C.B. Jackson, Gabe Shaughnessy, Tim M.P. Tait, and Alberto Vallinotto. Gamma Ray Lines from a Universal Extra Dimension. *JCAP*, 1203:020, 2012b. doi: 10.1088/1475-7516/2012/03/020.

J. Billard, L. Strigari, and E. Figueroa-Feliciano. Implication of Neutrino Backgrounds on the Reach of Next Generation Dark Matter Direct Detection Experiments. *Phys.Rev.*, D89:023524, 2014.

Andreas Birkedal, Konstantin Matchev, and Maxim Perelstein. Dark Matter at Colliders: A Model Independent Approach. *Phys.Rev.*, D70:077701, 2004. doi: 10.1103/PhysRevD.70.077701.

Elliott D. Bloom and James D. Wells. Multi - GeV Photons from Electron - Dark Matter Scattering Near Active Galactic Nuclei. *Phys.Rev.*, D57:1299–1302, 1998. doi: 10.1103/PhysRevD.57.1299.

Torsten Bringmann, Lars Bergstrom, and Joakim Edsjo. New Gamma-Ray Contributions to Supersymmetric Dark Matter Annihilation. *JHEP*, 0801:049, 2008. doi: 10.1088/1126-6708/2008/01/049.

J. Buckley, D.F. Cowen, S. Profumo, A. Archer, M. Cahill-Rowley, et al. Cosmic Frontier Indirect Dark Matter Detection Working Group Summary. 2013.

Gustavo Burdman, Bogdan A. Dobrescu, and Eduardo Ponton. Six-dimensional Gauge Theory on the Chiral Square. *JHEP*, 0602:033, 2006a. doi: 10.1088/1126-6708/2006/02/033.

Gustavo Burdman, Bogdan A. Dobrescu, and Eduardo Ponton. Resonances from Two Universal Extra Dimensions. *Phys.Rev.*, D74:075008, 2006b. doi: 10.1103/PhysRevD.74.075008.

C. Burgess and G. Moore. *The Standard Model: A Primer*. Cambridge University Press, 12 2006.

C.P. Burgess, Maxim Pospelov, and Tonnis ter Veldhuis. The Minimal Model of Non-Baryonic Dark Matter: A Singlet Scalar. *Nucl.Phys.*, B619:709–728, 2001. doi: 10.1016/S0550-3213(01)00513-2.

Qing-Hong Cao, Chuan-Ren Chen, Chong Sheng Li, and Hao Zhang. Effective Dark Matter Model: Relic Density, CDMS II, Fermi LAT and LHC. *JHEP*, 1108:018, 2011. doi: 10.1007/JHEP08(2011)018.

Linda M. Carpenter, Andrew Nelson, Chase Shimmin, Tim M.P. Tait, and Daniel Whiteson. Collider Searches for Dark Matter in Events with a Z Boson and Missing Energy. *Phys.Rev.*, D87(7):074005, 2013. doi: 10.1103/PhysRevD.87.074005.

Spencer Chang, Yu Gao, and Michael Spannowsky. Enhanced Gamma Ray Signals in Cosmic Proton-Wimp Collisions Due to Hadronization. *JCAP*, 1211:053, 2012. doi: 10.1088/1475-7516/2012/11/053.

Spencer Chang, Ralph Edezhath, Jeffrey Hutchinson, and Markus Luty. Effective WIMPs. *Phys.Rev.*, D89:015011, 2014a. doi: 10.1103/PhysRevD.89.015011.

Spencer Chang, Ralph Edezhath, Jeffrey Hutchinson, and Markus Luty. Leptophilic Effective WIMPs. 2014b.

Serguei Chatrchyan et al. Observation of a New Boson at a Mass of 125 GeV with the CMS Experiment at the LHC. *Phys.Lett.*, B716:30–61, 2012. doi: 10.1016/j.physletb.2012.08.021.

Kingman Cheung, Po-Yan Tseng, Yue-Lin S. Tsai, and Tzu-Chiang Yuan. Global Constraints on Effective Dark Matter Interactions: Relic Density, Direct Detection, Indirect Detection, and Collider. *JCAP*, 1205:001, 2012. doi: 10.1088/1475-7516/2012/05/001.

Marco Cirelli. Indirect Searches for Dark Matter: A Status Review. *Pramana*, 79:1021–1043, 2012. doi: 10.1007/s12043-012-0419-x.

Marco Cirelli, Roberto Franceschini, and Alessandro Strumia. Minimal Dark Matter Predictions for Galactic Positrons, Anti-protons, Photons. *Nucl.Phys.*, B800:204–220, 2008. doi: 10.1016/j.nuclphysb.2008.03.013.

James M. Cline, Grace Dupuis, and Zuowei Liu. LHC Constraints on Dark Matter with (130 GeV) Gamma Ray Lines. *JHEP*, 1309:065, 2013. doi: 10.1007/JHEP09(2013)065.

The ATLAS Collaboration. Performance Assumptions for an Upgraded ATLAS Detector at a High-Luminosity LHC, 04 2014. ATLAS Note. ATLAS-PHYS-PUB-2013-004 revised.

Jonathan M. Cornell, Stefano Profumo, and William Shepherd. Kinetic Decoupling and Small-Scale Structure in Effective Theories of Dark Matter. *Phys.Rev.*, D88(1):015027, 2013. doi: 10.1103/PhysRevD.88.015027.

Claudio Corti. The Cosmic Ray Electron and Positron Spectra Measured by AMS-02. 2014.

P. Cushman, C. Galbiati, D.N. McKinsey, H. Robertson, T.M.P. Tait, et al. Snowmass CF1 Summary: WIMP Dark Matter Direct Detection. 2013.

S. Dawson. Introduction to Electroweak Symmetry Breaking. pages 1–83, 1998.

Anthony DiFranzo, Keiko I. Nagao, Arvind Rajaraman, and Tim M. P. Tait. Simplified Models for Dark Matter Interacting with Quarks. *JHEP*, 1311:014, 2013. doi: 10.1007/JHEP11(2013)014.

Bogdan A. Dobrescu and Eduardo Ponton. Chiral Compactification on a Square. *JHEP*, 0403:071, 2004. doi: 10.1088/1126-6708/2004/03/071.

Bogdan A. Dobrescu, Dan Hooper, Kyoungchul Kong, and Rakhi Mahbubani. Spinless Photon Dark Matter from two Universal Extra Dimensions. *JCAP*, 0710:012, 2007a. doi: 10.1088/1475-7516/2007/10/012.

Bogdan A. Dobrescu, Kyoungchul Kong, and Rakhi Mahbubani. Leptons and Photons at the LHC: Cascades Through Spinless Adjoints. *JHEP*, 0707:006, 2007b. doi: 10.1088/1126-6708/2007/07/006.

Manuel Drees, Mitsuru Kakizaki, and Suchita Kulkarni. The Thermal Abundance of Semi-Relativistic Relics. *Phys.Rev.*, D80:043505, 2009. doi: 10.1103/PhysRevD.80.043505.

Herbi Dreiner, Daniel Schmeier, and Jamie Tattersall. Contact Interactions Probe Effective Dark Matter Models at the LHC. *Europhys.Lett.*, 102:51001, 2013. doi: 10.1209/0295-5075/102/51001.

A. Duncan. *The Conceptual Framework of Quantum Field Theory*. Oxford University Press, USA, 10 2012.

Joakim Edsjo, Mia Schelke, and Piero Ullio. Direct versus Indirect Detection in mSUGRA with Self-Consistent Halo Models. *JCAP*, 0409:004, 2004. doi: 10.1088/1475-7516/2004/09/004.

JiJi Fan, Matthew Reece, and Lian-Tao Wang. Non-Relativistic Effective Theory of Dark Matter Direct Detection. *JCAP*, 1011:042, 2010. doi: 10.1088/1475-7516/2010/11/042.

Jonathan L. Feng. Dark Matter Candidates from Particle Physics and Methods of Detection. *Ann.Rev.Astron.Astrophys.*, 48:495–545, 2010. doi: 10.1146/annurev-astro-082708-101659.

Jonathan L. Feng, Shufang Su, and Fumihiro Takayama. Lower Limit on Dark Matter Production at the Large Hadron Collider. *Phys.Rev.Lett.*, 96:151802, 2006. doi: 10.1103/PhysRevLett.96.151802.

A. Liam Fitzpatrick, Wick Haxton, Emanuel Katz, Nicholas Lubbers, and Yiming Xu. The Effective Field Theory of Dark Matter Direct Detection. *JCAP*, 1302:004, 2013. doi: 10.1088/1475-7516/2013/02/004.

Jean-Francois Fortin and Tim M.P. Tait. Collider Constraints on Dipole-Interacting Dark Matter. *Phys.Rev.*, D85:063506, 2012. doi: 10.1103/PhysRevD.85.063506.

Andrew Fowlie, Kamila Kowalska, Leszek Roszkowski, Enrico Maria Sessolo, and Yue-Lin Sming Tsai. Dark Matter and Collider Signatures of the MSSM. *Phys.Rev.*, D88(5):055012, 2013. doi: 10.1103/PhysRevD.88.055012.

Renata Zukanovich Funchal, Benoit Schmauch, and Gaelle Giesen. The Physics of Neutrinos. 2013.

Stefan Funk. Indirect Detection of Dark Matter with Gamma Rays. 2013.

Graciela Gelmini and Paolo Gondolo. DM Production Mechanisms. 2010.

Oleg Y. Gnedin and Joel R. Primack. Dark Matter Profile in the Galactic Center. *Phys.Rev.Lett.*, 93:061302, 2004. doi: 10.1103/PhysRevLett.93.061302.

Oleg Y. Gnedin, Andrey V. Kravtsov, Anatoly A. Klypin, and Daisuke Nagai. Response of Dark Matter Halos to Condensation of Baryons: Cosmological Simulations and Improved Adiabatic Contraction Model. *Astrophys.J.*, 616:16–26, 2004. doi: 10.1086/424914.

M.A. Gómez, C.B. Jackson, and G. Shaughnessy. WIMP-Induced Gamma Ray Spectrum of Active Galactic Nuclei. *Phys.Rev.*, D88(1):015024, 2013. doi: 10.1103/PhysRevD.88.015024.

M.A. Gomez, C.B. Jackson, and G. Shaughnessy. Dark Matter on Top. 2014.

P. Gondolo, J. Edsjo, P. Ullio, L. Bergstrom, Mia Schelke, et al. DarkSUSY: Computing Supersymmetric Dark Matter Properties Numerically. *JCAP*, 0407:008, 2004. doi: 10.1088/1475-7516/2004/07/008.

Paolo Gondolo and Graciela Gelmini. Cosmic Abundances of Stable Particles: Improved Analysis. *Nucl.Phys.*, B360:145–179, 1991. doi: 10.1016/0550-3213(91)90438-4.

Paolo Gondolo and Joseph Silk. Dark Matter Annihilation at the Galactic Center. *Phys.Rev.Lett.*, 83:1719–1722, 1999. doi: 10.1103/PhysRevLett.83.1719.

Paolo Gondolo, Graciela Gelmini, and Subir Sarkar. Cosmic Neutrinos from Unstable Relic Particles. *Nucl.Phys.*, B392:111–136, 1993. doi: 10.1016/0550-3213(93)90199-Y.

J. Goodman and J. Weare. Ensemble Samplers with Affine Invariance. *Comm. App. Math. Comp. Sci.*, 5(1):65–80, 2010. doi: 10.2140/camcos.2010.5.65.

Jessica Goodman, Masahiro Ibe, Arvind Rajaraman, William Shepherd, Tim M.P. Tait, et al. Constraints on Dark Matter from Colliders. *Phys.Rev.*, D82:116010, 2010. doi: 10.1103/PhysRevD.82.116010.

Jessica Goodman, Masahiro Ibe, Arvind Rajaraman, William Shepherd, Tim M.P. Tait, et al. Constraints on Light Majorana dark Matter from Colliders. *Phys.Lett.*, B695:185–188, 2011. doi: 10.1016/j.physletb.2010.11.009.

Mikhail Gorchtein, Stefano Profumo, and Lorenzo Ubaldi. Probing Dark Matter with AGN Jets. *Phys.Rev.*, D82:083514, 2010. doi: 10.1103/PhysRevD.84.069903,10.1103/PhysRevD.82.083514.

Alister W. Graham, David Merritt, Ben Moore, Juerg Diemand, and Balsa Terzic. Empirical models for Dark Matter Halos. I. Nonparametric Construction of Density Profiles and Comparison with Parametric Models. *Astron.J.*, 132:2685–2700, 2006. doi: 10.1086/508988.

Kim Griest. The Search for Dark Matter: WIMPs and MACHOs. 1993.

Kim Griest and David Seckel. Three Exceptions in the Calculation of Relic Abundances. *Phys.Rev.*, D43:3191–3203, 1991. doi: 10.1103/PhysRevD.43.3191.

Kim Griest, Agnieszka M. Cieplak, and Matthew J. Lehner. New Limits on Primordial Black Hole Dark Matter from an Analysis of Kepler Source Microlensing Data. *Phys.Rev.Lett.*, 111:181302, 2013. doi: 10.1103/PhysRevLett.111.181302.

D. Griffiths. *Introduction to Particle Physics*. John Wiley & Sons Inc., 03 1987.

M. Guidry. *Gauge Field Theories: An Introduction with Applications*. Wiley-Interscience, 09 1991.

Shunsaku Horiuchi, Philip J. Humphrey, Jose Onorbe, Kevork N. Abazajian, Manoj Kaplinghat, et al. Sterile Neutrino Dark Matter Bounds from Galaxies of the Local Group. 2013.

Jin-Rui Huang, Arvind Rajaraman, and Tim M.P. Tait. Collisions of Jets of Particles from Active Galactic Nuclei with Neutralino Dark Matter. *JCAP*, 1205:027, 2012. doi: 10.1088/1475-7516/2012/05/027.

Hoernisa Iminniyaz, Manuel Drees, and Xuelei Chen. Relic Abundance of Asymmetric Dark Matter. *JCAP*, 1107:003, 2011. doi: 10.1088/1475-7516/2011/07/003.

C.B. Jackson, Geraldine Servant, Gabe Shaughnessy, Tim M.P. Tait, and Marco Taoso. Higgs in Space! *JCAP*, 1004:004, 2010. doi: 10.1088/1475-7516/2010/04/004.

C.B. Jackson, Geraldine Servant, Gabe Shaughnessy, Tim M.P. Tait, and Marco Taoso. Gamma-Ray Lines and One-Loop Continuum from s-Channel Dark Matter Annihilations. *JCAP*, 1307: 021, 2013a. doi: 10.1088/1475-7516/2013/07/021.

C.B. Jackson, Géraldine Servant, Gabe Shaughnessy, Tim M.P. Tait, and Marco Taoso. Gamma Rays from Top-Mediated Dark Matter Annihilations. *JCAP*, 1307:006, 2013b. doi: 10.1088/1475-7516/2013/07/006.

E. Kolb and Turner M. *The Early Universe*. Westview Press, 02 1994.

M.S. Longair. *High Energy Astrophysics*. Cambridge University Press, 03 2011.

Konstantin Matchev. TASI Lectures on Precision Electroweak Physics. pages 51–98, 2004.

Samuel D. McDermott, Hai-Bo Yu, and Kathryn M. Zurek. The Dark Matter Inverse Problem: Extracting Particle Physics from Scattering Events. *Phys.Rev.*, D85:123507, 2012. doi: 10.1103/PhysRevD.85.123507.

John McDonald. Gauge Singlet Scalars as Cold Dark Matter. *Phys.Rev.*, D50:3637–3649, 1994. doi: 10.1103/PhysRevD.50.3637.

Vasiliki A. Mitsou. Shedding Light on Dark Matter at Colliders. *Int.J.Mod.Phys.*, A28:1330052, 2013. doi: 10.1142/S0217751X13300524.

R.N. Mohapatra, S. Antusch, K.S. Babu, G. Barenboim, Mu-Chun Chen, et al. Theory of Neutrinos: A White Paper. *Rept.Prog.Phys.*, 70:1757–1867, 2007. doi: 10.1088/0034-4885/70/11/R02.

Julio F. Navarro, Carlos S. Frenk, and Simon D.M. White. The Structure of Cold Dark Matter Halos. *Astrophys.J.*, 462:563–575, 1996. doi: 10.1086/177173.

G. Passarino and M.J.G. Veltman. One Loop Corrections for e+ e- Annihilation Into mu+ mu- in the Weinberg Model. *Nucl.Phys.*, B160:151, 1979. doi: 10.1016/0550-3213(79)90234-7.

Brian Patt and Frank Wilczek. Higgs-Field Portal into Hidden Sectors. 2006.

Francisco Prada, Anatoly Klypin, Jose Flix Molina, M. Martinez, and E. Simonneau. Dark Matter Annihilation in the Milky Way Galaxy: Effects of Baryonic Compression. *Phys.Rev.Lett.*, 93: 241301, 2004. doi: 10.1103/PhysRevLett.93.241301.

Stefano Profumo. TASI 2012 Lectures on Astrophysical Probes of Dark Matter. 2013.

Stefano Profumo, Lorenzo Ubaldi, and Mikhail Gorchtein. Gamma Rays from Cosmic-Ray Proton Scattering in AGN Jets: the Intra-Cluster Gas Vastly Outshines Dark Matter. *JCAP*, 1304:012, 2013. doi: 10.1088/1475-7516/2013/04/012.

Tarek Saab. An Introduction to Dark Matter Direct Detection Searches & Techniques. 2012.

Marc Schumann. Dark Matter 2013. 2013.

Vanda Silveira and A. Zee. Scalar Phantoms. *Phys.Lett.*, B161:136, 1985. doi: 10.1016/0370-2693(85)90624-0.

M. Srednicki. *Quantum Field Theory*. Cambridge University Press, 02 2007.

Robin G. Stuart. Algebraic Reduction of One Loop Feynman Diagrams to Scalar Integrals. *Comput.Phys.Commun.*, 48:367–389, 1988. doi: 10.1016/0010-4655(88)90202-0.

Marco Taoso, Gianfranco Bertone, and Antonio Masiero. Dark Matter Candidates: A Ten-Point Test. *JCAP*, 0803:022, 2008. doi: 10.1088/1475-7516/2008/03/022.

M. Thompson. *Modern Particle Physics*. Cambridge University Press, 10 2013.

Ho-Chin Tsai and Kwei-Chou Yang. Dark Matter Mass Constrained by the Relic Abundance, Direct Detections, and Colliders. *Phys.Rev.*, D87(11):115016, 2013. doi: 10.1103/PhysRevD.87.115016.

Sean Tulin, Hai-Bo Yu, and Kathryn M. Zurek. Three Exceptions for Thermal Dark Matter with Enhanced Annihilation to $\gamma\gamma$. *Phys.Rev.*, D87:036011, 2013a. doi: 10.1103/PhysRevD.87.036011.

Sean Tulin, Hai-Bo Yu, and Kathryn M. Zurek. Resonant Dark Forces and Small Scale Structure. *Phys.Rev.Lett.*, 110(11):111301, 2013b. doi: 10.1103/PhysRevLett.110.111301.

Sean Tulin, Hai-Bo Yu, and Kathryn M. Zurek. Beyond Collisionless Dark Matter: Particle Physics Dynamics for Dark Matter Halo Structure. *Phys.Rev.*, D87(11):115007, 2013c. doi: 10.1103/PhysRevD.87.115007.

A. Zee. *Quantum Field Theory in a Nutshell*. Princeton University Press, second edition, 02 2010.

Yue Zhang. Top Quark Mediated Dark Matter. *Phys.Lett.*, B720:137–141, 2013. doi: 10.1016/j.physletb.2013.01.063.

Biographical Statement

Miguel Alejandro Gómez Ramírez was born in Bogotá, Colombia, in 1976. He received his B.Sc. in Industrial Engineering from Universidad de los Andes, Bogotá, Colombia, in 2001; his B.Sc. in Physics from Universidad de los Andes, Bogotá, Colombia, in 2006; his M.Sc. in Physics from University of Texas at Arlington, U.S. in 2011, and his Ph.D degree in Physics from the University of Texas at Arlington in 2014. He worked as a quantitative analyst at different companies in Colombia between 2001 and 2009. His current research interest include beyond the Standard Model physics, i.e., dark matter, and computational and statistical methods in finance.